

High Resolution Spectroscopy  
of  
Photospheric Bright Points

DISSERTATION

zur

Erlangung des Doktorgrades

der

FAKULTÄT FÜR MATHEMATIK UND PHYSIK

der

ALBERT-LUDWIGS-UNIVERSITÄT

FREIBURG IM BREISGAU

vorgelegt von

Katarzyna Mikurda

2005

---

Dekan: Prof. Dr. J. Honerkamp  
Betreuer: Prof. Dr. O. von der Lühe  
Referent: Prof. Dr. O. von der Lühe  
Koreferent: Prof. Dr. F. Stienkenmeier  
Datum der mündlichen Prüfung: 24.10.2005

---

*God could cause us considerable embarrassment by revealing all the secrets of nature to us: we should not know what to do for sheer apathy and boredom.*

Johann von Goethe



In the context of this thesis the following articles have been published:

### **Journal papers**

Mikurda, K., Tritschler, A., Schmidt, W., 2006,

*The influence of image reconstruction on two-dimensional spectrograms of the solar photosphere*

Astronomy & Astrophysics, accepted

Mikurda, K., von der Lühe, O., 2006,

*High Resolution Solar Speckle Imaging with the Extended Knox - Thompson algorithm*

Solar Physics, accepted

### **Other publications**

Mikurda, K., von der Lühe, O., Schmidt, W., 2003,

*Dynamics of the G-band Bright Points*

Astronomische Nachrichten, Supplementary Issue 3, Vol. 324, p.24

Mikurda, K., von der Lühe, O., Wöger, F., 2003

*Solar Imaging with an Extended Knox-Thompson Technique*

Astronomische Nachrichten, Supplementary Issue 3, Vol. 324, p.112



## Abstract

Photospheric bright points are proxies for small-scale magnetic flux concentrations. These magnetic elements are thought to be the building blocks of the solar magnetic field and are important to understand many physical processes on the Sun, e.g. the variability of the solar irradiance. Because of their small size (100-200 km in diameter) the observations of photospheric bright points put special requirements on the seeing conditions, instrumental setup and post-processing techniques.

The motivation of this work comes from theoretical predictions concerning flows associated with magnetic elements. Solar magneto-convection simulations indicate that the formation of these structures is accompanied with large downflows that can reach velocities of several km/s. In some cases, the downflowing gas may rebound in the deeper layers which can cause an upward-propagating shock.

MHD simulations have usually much better resolution than observational data, so advanced observational techniques need to be applied to compare them.

Speckle reconstruction techniques are widely used to improve the quality of ground-based solar observations. To date, there have been no comprehensive analysis of photometric errors of the speckle reconstruction process and of the influence of the speckle deconvolution on spectral line profiles. In this thesis, the results of such an analysis are presented, followed by a conclusion that speckle-reconstructed spectral line profiles can be used for quantitative spectroscopy.

The data set presented in this thesis consists of speckle-reconstructed G-band images and quasi-simultaneous two-dimensional spectra in the neutral iron line at 557.6 nm. The choice of the G-band - a molecular bandhead at around 430 nm - for observations of photospheric bright points is motivated by their increased contrast with respect to the surroundings at this wavelength range.

In this analysis, spectral profiles were used to determine line-of-sight velocities at photospheric bright points locations. I found that the majority of bright points are associated with downflow regions, which is consistent with previous findings. Velocities derived from the line core (formed in higher photospheric layers) are reduced in comparison with velocities of the line wing which is formed lower in the atmosphere, in agreement with some theoretical predictions. Individual cases of photospheric bright points were studied in order to understand their interaction with surrounding granular flow. The maximum downflow usually do not coincides with the maximum G-band intensity. No downflows with velocities of few km/s as predicted by MHD simulations have been found, but it may be due to the lack of sufficient spatial resolution. There were only very few photospheric bright points in the analyzed data which showed upflows with respect to their immediate surroundings.



## Zusammenfassung

Photosphärische Bright Points sind Proxies von kleinskaligen magnetischen Flusskonzentrationen. Man glaubt das diese magnetischen Elemente Bausteine des solaren magnetischen Feldes sind, und somit als sehr wichtig für das Verständnis von vielen physikalischen Prozessen unserer Sonnen anzusehen sind (z.B. die Variabilität der solaren Irradiation.). Wegen der geringen Größe von photosphärischen Bright Points (100-200 km im Durchmesser) gestaltet sich ihre Beobachtung schwierig und bedarf spezieller Anforderungen an das Seeing, dem instrumentellem Setup und an post verarbeitenden Techniken.

Die Motivation der vorliegenden Arbeit leitet sich von der theoretischen Vorhersage von flussassoziierten magnetischen Elementen ab. Simulationen der solare Magnetokonvektion indizieren, dass die Entstehung dieser Strukturen in Begleitung mit großen Downflows in der Größenordnung von mehreren km/s auftreten. In einigen Fällen konnte gezeigt werden, dass das Downflow-Gas in tieferen Lagen zurückprallt und somit aufwärts propagierende Schockwellen anregen kann.

Üblicherweise haben MHD Simulationen eine höhere Auflösung als Beobachtungsmaterial, so dass fortschrittliche Beobachtungstechniken zur Verifikation der Simulationsergebnisse notwendig sind.

Speckle-Rekonstruktionsverfahren werden weitestgehend zur Qualitätsverbesserung von erdgebundenen solaren Beobachtungen verwendet. Bis jetzt gab es keine umfangreichen Analysen der photometrischen Fehler von Speckle-Rekonstruktionsprozessen und deren Einflüsse auf die Speckle-Dekonvolution von spektralen Linienprofilen. In dieser Arbeit werden Ergebnisse solcher Analysen präsentiert mit der Schlussfolgerung, dass Speckle-rekonstruierte spektrale Linienprofile zur quantitativen Spektroskopie verwendet werden können.

In dieser Arbeit haben wir einen Datensatz bestehend aus speckle rekonstruierten G-Band Bildern und quasi simultanen 2-dimensionalen Spektren der neutralen Eisenlinie bei 577.6 nm verwendet. Die Wahl des G-Band, das ein Molekül-Bandhead bei ungefähr 430 nm darstellt, für die Beobachtung von photosphärischen Bright Points zu verwenden ist über den ansteigenden Umgebungskontrast in diesem Wellenlängenbereich motiviert.

In der Analyse wurden Spektralprofile verwendet um die Line-of-Sight Geschwindigkeiten an den Lokationen von Bright Points zu bestimmen. Im Zuge der Arbeit haben wir herausgefunden, dass ein Großteil der Bright Points mit Downflow Regionen assoziiert sind. Somit konnten vorherige Ergebnisse bestätigt werden. Die Geschwindigkeiten in den Linienkernen, welche in höheren photosphärischen Lagen entstehen, sind geringer im Vergleich zu den Geschwindigkeiten in den Linienflügeln, welche ihren Ursprung tiefer in der Atmosphäre haben. Diese Beobachtung steht in Einklang mit theoretischen Vorhersagen. Einzelne Fälle von photosphärischen Bright Points wurden untersucht um die Interaktion mit der umliegenden Granulation besser zu verstehen. Der maximale Downflow stimmt im Allgemeinen nicht mit der maximalen G-Band Intensität

überein. Heutige MHD Simulation sagen Downflows in der Größenordnung von einigen km/s voraus. Diese Vorhersagen konnten durch unsere Ergebnisse nicht bestätigt werden. Es besteht allerdings durchaus die Möglichkeit, dass unsere Ergebnisse auf eine eingeschränkte räumliche Auflösung zurückzuführen sind. Es gab nur wenige photosphärische Bright Points in den Beobachtungsdaten, die Upflows im Zusammenhang mit deren unmittelbaren Umgebungen zeigten.

# Contents

<b>1</b>	<b>Introduction</b>	<b>1</b>
<b>2</b>	<b>High resolution ground-based solar observations</b>	<b>5</b>
2.1	Atmospheric turbulence . . . . .	5
2.1.1	The structure of turbulence . . . . .	6
2.1.2	Kolmogorov model of turbulence . . . . .	6
2.1.3	Wave propagation through turbulence . . . . .	6
2.1.4	Properties of long- and short-exposure images . . . . .	8
2.2	Image reconstruction techniques . . . . .	9
2.2.1	Adaptive optics . . . . .	9
2.2.2	Speckle imaging . . . . .	10
2.3	Speckle reconstruction and adaptive optics . . . . .	19
2.4	The summary . . . . .	19
<b>3</b>	<b>Two-dimensional solar spectroscopy</b>	<b>23</b>
3.0.1	2-D solar spectra from TESOS . . . . .	24
3.1	Speckle deconvolution of 2-D spectra . . . . .	24
3.2	Photometric quality of speckle deconvolution . . . . .	27
3.2.1	Observations . . . . .	27
3.2.2	Data reduction and reconstruction . . . . .	28
3.3	Results . . . . .	29
3.3.1	“Grainy pattern” . . . . .	31
3.3.2	Difference between the blue and red wing of 557.6 nm Fe I line . . . . .	32
3.3.3	Influence of the speckle deconvolution on the spectral lines . . . . .	33
3.3.4	Quiet and abnormal granulation . . . . .	36
<b>4</b>	<b>Photospheric bright points</b>	<b>39</b>
4.1	From filigrees to G-band bright points . . . . .	39
4.2	Understanding photospheric bright points . . . . .	42
4.3	Why are PBPs bright in the G-band ? . . . . .	46

<b>5 Spectroscopy of photospheric bright points</b>	<b>49</b>
5.1 Observations . . . . .	49
5.1.1 Velocity maps . . . . .	49
5.2 Identification of bright points in the G-band images . . . . .	52
5.3 Line-of-sight velocity distribution . . . . .	54
5.4 Are photospheric bright points bright in the line core of Fe I at 557.6 nm ? . . . .	60
5.5 Individual cases . . . . .	60
5.5.1 Individual case 1 . . . . .	62
5.5.2 Individual case 2 . . . . .	62
5.5.3 Individual case 3 . . . . .	62
5.5.4 Individual case 4 . . . . .	64
5.6 Elongated structures . . . . .	65
5.7 Velocities and height of formation of spectral lines . . . . .	67
<b>6 Conclusions and outlook</b>	<b>71</b>
<b>A Spectroscopic observations</b>	<b>75</b>
A.1 TESOS - TElecentric SOlar Spectrometer . . . . .	75
A.2 Intensity modulation . . . . .	75
<b>B Precision of velocity measurements</b>	<b>79</b>
<b>C The optical depth</b>	<b>81</b>

# Chapter 1

## Introduction

*If it were not for its magnetic field, the Sun would be as dull a star as most astronomers think it is.*

Robert Leighton

At the beginning of the XVIIth century, soon after the telescope was invented, three independent observers: Galileo Galilei, Johann Fabricius and Christopher Scheiner used it to observe the Sun. They all saw dark patches on the solar disc: the sunspots. Galileo believed that sunspots were part of the Sun itself and speculated that they might be clouds floating in the Sun's atmosphere, blocking some of its light.

Galileo could not know that his discovery opened a new door to understanding the Sun. However, the nature of sunspots remained unclear for the next 300 years until G. Hale proved that sunspots are associated with strong magnetic fields.

The generation mechanism of solar magnetic fields still is a very controversial issue, but it is generally accepted that the magnetic field is generated in the convective envelope of the Sun (see Fig. 1.1) by a dynamo mechanism. The convection stops at the photosphere which is the visible surface and the deepest layer of the Sun accessible to direct observations. The magnetic field created in the convective zone emerges through the photosphere, revealing its presence as sunspots.

The sunspots are the largest and long-living solar magnetic structures, but not the only ones. Pores are dark magnetic patches, too, but they are smaller than sunspot and lacking penumbrae. Flux can be concentrated at even smaller scales: micropores and small scale magnetic elements have characteristic sizes below 1000 km. While micropores are darker than their surroundings, like sunspots or pores, magnetic elements are brighter than the quiet photosphere. According to Topka et al. [1997] this transition occurs at a diameter of about 300 km. While the sunspots and pores occur only in active regions within the activity belts, small magnetic elements are distributed over the whole solar surface, with larger concentrations at the borders of

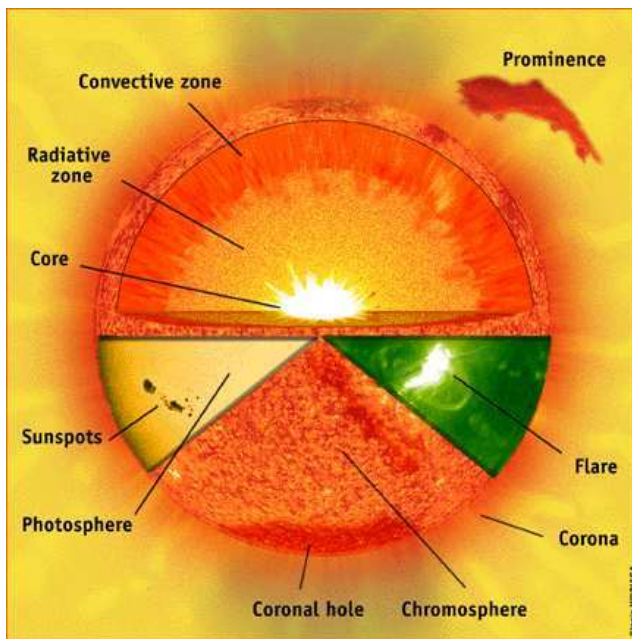


Figure 1.1: The structure of the Sun.  
Image: ESA/NASA

supergranular cells and in active regions.

The range of magnetic flux spatial scales in the solar photosphere is very large: spots have diameters up to  $10^5$  km, while magnetic elements are thousand time smaller. Even more surprising is the fact that all these structures can be, at least to a first approximation, described as *flux tubes*. This is one of the most important concepts in the solar physics and it will be addressed later.

Investigating the nature, formation and evolution of the magnetic elements is important to understand many processes in the Sun, such as variations of the solar irradiance, or formation of active regions.

*Photospheric bright points* are proxies for magnetic elements. They are very challenging to an observer because of their small sizes and require high resolution post-focus instruments and advanced observational techniques.

Results of MHD simulations indicate that there may be strong vertical flows associated with the magnetic elements, but measurements of line-of-sight velocities at bright points locations are scarce.

The aim of this thesis is to present the high resolution observational techniques that have been (co)developed by the author and their application to observations of photospheric bright points. The main scientific goal was to use spectral information in order to understand vertical flows associated with magnetic elements.

This thesis is divided into six chapters. The introduction is followed by Chapter 2 that gives an overview of high resolution observational techniques. Moreover, it discusses the basic principles and tests of the speckle reconstruction code developed at Kiepenheuer-Institut and used to improve data analyzed in this thesis. Chapter 3 introduces the reader to two-dimensional solar spectroscopy

and discusses the achievements of the author in speckle deconvolution of spectral data. Chapter 4 is introductory and deals with past observations and modeling of photospheric bright points. Chapter 5 presents results on dynamic properties of photospheric bright points, resulting from high resolution spectroscopic observations. Finally, the results are summarized and concluded in Chapter 6, which also gives some outlook on the future work.



## Chapter 2

# High resolution ground-based solar observations

The resolution of a solar telescope is limited by the diffraction at the telescope aperture and imaging errors of the optics. The diffraction limit of ground-based telescope with 1 m diameter is about 0.1 arcsec in the visible, which corresponds to approximately 75 km on the solar surface. In reality, the spatial resolution of a large telescope is limited by the influence of turbulence in the Earth's atmosphere rather than by the performance of imaging systems.

This problem requires the application of techniques that compensate effectively the degrading effects induced by the Earth's atmosphere in an either active and thus real-time way (i.e. correlation tracking, adaptive optics), or post-facto in a passive way (i.e. speckle imaging, phase-diversity and deconvolution techniques). In this chapter I give a short introduction to the image reconstruction techniques which have been applied to the data presented and analyzed in this thesis.<sup>1</sup>

### 2.1 Atmospheric turbulence

Big whorls have little whorls  
That feed on their velocity,  
And little whorls have smaller whorls  
And so on to viscosity.

L. F. Richardson

---

<sup>1</sup>Many issues addressed in this chapter are discussed in more detail by Roggemann and Welsh [1995] and Hardy [1998].

### 2.1.1 The structure of turbulence

The velocity fields in Earth's atmosphere are almost always turbulent with Reynolds numbers of order of  $10^6$  (fully developed turbulence). The kinetic energy of the turbulence is generated on larger scales  $L_0$  (*outer scale* of the turbulence) and dissipated in small eddies with characteristic size  $l_0$  (*inner scale* of the turbulence).  $l_0$  is of order of a few millimeters, while  $L_0$  can be tens to hundreds of meters and corresponds to the thickness of turbulent layers. We can therefore distinguish three ranges of the turbulence, as characterized by an eddy scale:

- Excitation range with scales  $l > L_0$ : in the lower atmosphere
- Inertial (Kolmogorov) range ( $l_0 < l < L_0$ ): the kinetic energy of large scale motions is transferred to smaller scales
- Dissipation range ( $l > l_0$ ): the kinetic energy is dissipated into heat by viscous friction.

In the inertial range the turbulence strength depends on the cell size (so the spatial frequency  $\kappa$ ). This very important fact underlies the Kolmogorov model of turbulence.

### 2.1.2 Kolmogorov model of turbulence

Kolmogorov [1941] suggested that, in a fully developed turbulence, kinetic energy cascades from larger to smaller scales, so turbulent eddies become smaller and smaller until they are subject to viscous dissipation. Assuming the stationary state, we can demand that the rate of energy dissipation  $\epsilon_0$  be equal to the rate of production of turbulent energy. If we assume that the velocity  $v$  of motions at scale  $l$  depends only on  $l$  and  $\epsilon_0$ , a dimensional analysis leads to

$$v \propto \epsilon_0^{1/3} l^{1/3}. \quad (2.1)$$

The kinetic energy is proportional to  $v^2$ . Then the energy spectrum  $E(\kappa)$ , where the  $\kappa$  is the spatial frequency (or wave number) and the  $\kappa \propto \frac{1}{l}$ , is

$$E(\kappa) \propto \kappa^{-2/3}. \quad (2.2)$$

Expression 2.2 is called the Kolmogorov law and is only valid in the inertial range and under the assumption that the turbulence is homogeneous and isotropic and the medium is incompressible. Despite these limitations (e.g. Earth's atmosphere is not homogeneous and isotropic), the range where the Kolmogorov model applies is surprisingly large.

### 2.1.3 Wave propagation through turbulence

An optical wave arriving from the Sun can be considered as plane before entering the Earth's atmosphere. But random temperature inhomogeneities causes the refraction index distribution in

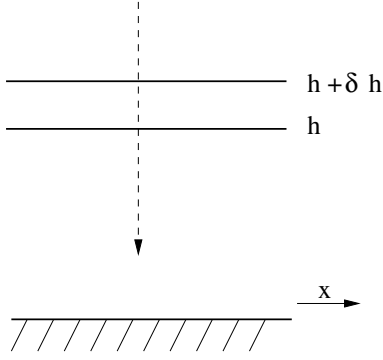


Figure 2.1: Propagation of a plane wave through the atmosphere.

the atmosphere to be random as well. They introduce random phase delays into different parts of the wave and the wavefront becomes deformed. This effect reduces the angular resolution of the ground-based telescopes and in most cases renders diffraction limited images impossible.

Consider a plane wavefront with a constant amplitude  $\Psi(x) = \exp(i\Phi(x))$  (see Fig. 2.1) that propagates through turbulent layer of thickness  $\delta h$  at height  $h$ . In the geometric approximation the phase shift introduced by refractive index fluctuation is

$$\Phi(x) = k \int_h^{h+\delta h} n(x, z) dz, \quad (2.3)$$

where  $k = 2\pi/\lambda$  and the wavefront after passing the turbulent layer is

$$\Psi(x) = e^{i\Phi(x) + k \int_h^{h+\delta h} n(x, z) dz} \quad (2.4)$$

because amplitude variations are neglected.

If the turbulence is not too strong, the phase errors from different layers add linearly.

The random processes are mostly described by correlation functions, but for the atmospheric turbulence there is sometimes a problem in defining them (because the Kolmogorov spectrum diverges for  $\kappa \rightarrow 0$ ), and a *structure function* is defined instead:

$$D_\Phi(\vec{r}) = \langle [\Phi(\vec{x} + \vec{r}) - \Phi(\vec{x})]^2 \rangle. \quad (2.5)$$

It can be shown that the temperature and the refractive index fluctuations follow the Kolmogorov law (in three dimensions), too:

$$D_T = C_T^2 r^{2/3} \quad (2.6)$$

$$D_n = C_n^2 r^{2/3}. \quad (2.7)$$

$C_T^2$  and  $C_n^2$  are called temperature structure constant and refractive index structure constant,

respectively.

The structure function  $D_\Phi$  can be derived from Eq. 2.7 by integrating along the direction of the wave propagation with the result:

$$D_\Phi(\vec{r}) = 2.914 k^2 \sec \gamma r^{5/3} \int_0^\infty C_n^2(z) dz = 6.88 \left( \frac{|\vec{r}|}{r_0} \right)^{5/3}, \quad (2.8)$$

where  $C_n^2(z)$  is a continuous distribution of the structure coefficient with height  $z$ ,  $k$  is a wave number and  $\gamma$  is the zenith distance.  $r_0$  is called *atmospheric coherence radius* or *Fried parameter* and is a measure of the turbulence strength (in astronomy mostly referred as to “seeing”). It can be understood as the diameter of a wavefront area over which the rms phase variations due to the atmospheric turbulence are within 1 rad. Secondly, the resolution of an image obtained through the atmosphere characterized by  $r_0$  is the same as the resolution of an diffraction-limited image taken with a telescope with diameter  $r_0$ . This means that when the diameter of the telescope  $D$

- $D < r_0$  - the resolving power is limited by the telescope.
- $D > r_0$  - the resolving power is limited by the atmosphere.

There are two important functional relations of the Fried parameter:

- $r_0$  is an integral over the  $C_n^2(z)$

$$r_0 = \left( 0.432 k^2 \sec \gamma \int_0^\infty C_n^2(z) dz \right)^{-3/5}. \quad (2.9)$$

- $r_0$  increases with wavelength

$$r_0 \propto (\lambda)^{6/5}. \quad (2.10)$$

From the latter dependence one can easily see that it is much easier to achieve diffraction-limited images at longer wavelengths with a telescope of given diameter.

#### 2.1.4 Properties of long- and short-exposure images

The evolution of the turbulence pattern usually takes more time than it is needed for the turbulence to pass in front of the telescope aperture. The *frozen turbulence hypothesis* [Taylor, 1938] states that as the wind transports the turbulent layer past the aperture, the fundamental properties of the turbulence remain unchanged (or *frozen*) in this layer. It becomes more complicated when the light passes through many turbulent layers, but we can still characterize the temporal changes of the turbulence by the *time constant (atmospheric coherence time)*

$$\tau_0 \equiv r_0/v, \quad (2.11)$$

where  $v$  is the mean wind speed in the (dominant) layer. For example, for the wind speed of 10 m/s and a Fried parameter of 10 cm, the  $\tau_0$  is about 10 ms.

Observations taken with exposure time  $\tau_0$  or shorter are called short-exposure images and represent a single instantaneous realization of the atmosphere. Such images are often called *speckle images* and contain information at high spatial frequencies. There is a variety of *speckle reconstruction techniques* which are able to recover those frequencies up to the diffraction limit (see Sec. 2.2.2).

With exposure times longer than  $\tau_0$ , the atmospheric aberrations are averaged and most of the high-frequency information is lost.

Light from two regions on the Sun separated by an angle  $\theta$  passes through different atmospheric conditions, so it experiences different wavefront distortions. This effect is called *angular anisoplanatism*. It is useful to introduce the *isoplanatic angle*  $\theta_0$ , for which the rms phase variation is  $1 \text{ rad}^2$ :

$$\theta_0 = 0.314 (\cos \gamma) \frac{r_0}{H}, \quad (2.12)$$

where  $H$  is the mean effective turbulence height.

Long-exposure images do not suffer from the anisoplanatism, but it has to be carefully taken into account when applying the speckle imaging techniques. More about it in Sec. 2.2.2.

## 2.2 Image reconstruction techniques

### 2.2.1 Adaptive optics

Since the data presented in this thesis were taken with the usage of an adaptive optics system, it is worthwhile to briefly describe its principles and applications.

Adaptive optics (AO) are widely used in the night-time astronomical observation since the mid-1990s [see e.g. Hardy, 1998], and is regularly used for solar observations since 2000. As already mentioned, the resolving power of large telescopes is limited not by their diameter, but by the seeing conditions. The adaptive optics enables to overcome these limitations by sensing and removing the disturbances in real time.

All AO systems comprise three main parts: the deformable mirror (correcting element), the wavefront sensor, and the actuator control loop. When the light beam enters the system, a part of it is used to measure the distortions of the incoming wavefront by the wavefront sensor. AO is a closed-loop system: the wavefront sensor follows the deformable mirror (see Fig. 2.2). The control criterion is a flat wavefront.

Solar adaptive optics systems are in some aspects more challenging than night-time AO. The seeing conditions are usually worse and more varying during the day and, due to the direct sunlight, the near-ground turbulence is stronger. This requires a larger number of correcting elements per area although the apertures of solar telescopes are usually smaller. The majority of

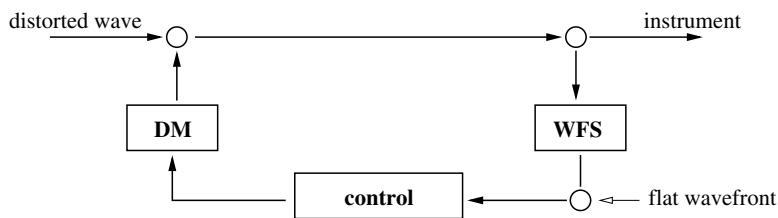


Figure 2.2: Adaptive optics: components (WS: wavefront sensor, DM: deformable mirror, control) and principle.

solar observations is made at visible wavelengths which means short atmospheric coherence times. From this reason high closed loop bandwidth are required.

While the night-time sky provides natural point sources, the low-contrast and strongly varying solar surface itself has to be used as a target.

In spite of all these challenges there are also clear advantages of the solar AO: the number of photons is much higher than this available to night-time observers and there is no sky coverage problem, because the solar AO can lock everywhere on the Sun.

In solar AO wavefront sensors which are based on correlation tracking on images formed by an array of subapertures are used. All currently operating solar AO system are based on correlating Shack-Hartmann wavefront sensors.

The Kiepenheuer-Institut Adaptive Optics System [KAOS, Soltau et al., 2002, von der Lühe et al., 2003] operates at the Vacuum Tower Telescope (VTT) on Tenerife since 2002. Its two main components are the bimorph-type deformable mirror with 35 actuators and the Shack-Hartmann wavefront sensor with 36 hexagonally arranged subapertures. The closed loop bandwidth is about 50 Hz.

The AO systems can compensate only a small area around the line of sight (“lock point”) of the wavefront sensor, because not all the refractive index fluctuations can be detected. The best performance of the adaptive optic systems (up to the diffraction limit) can therefore be expected in the immediate vicinity of the lock point and the efficiency decreases with increasing distance from the lock point. This is the reason why Multi-conjugate AO systems (multiple wavefront sensing and several deformable mirrors compensating a volume) are currently developed [Soltau et al., 2002, Rimmele, 2004, von der Lühe et al., in press].

### 2.2.2 Speckle imaging

Since the late 1980s speckle imaging has become a very important tool for ground-based solar observations. The capability of the original method introduced by Labeyrie [1970] is limited to retrieve other techniques that provide the full information (i.e. corrected Fourier amplitudes AND phases) on the observed intensity: Knox-Thompson algorithms [Knox and Thompson, 1974, von der Lühe, 1993, von der Lühe, 1994, Mikurda et al., 2003, Mikurda and von der Lühe, 2006] and the speckle masking [Weigelt, 1977, Pehlemann and von der Lühe, 1989, de Boer and Kneer, 1992]. These techniques have been originally developed for night time astronomy, but since the

mid-1980s are have been adopted and widely used in solar physics.

### KISIP: Kiepenheuer Institut Speckle Imaging Package

The Kiepenheuer-Institut Speckle Imaging Package has been developed since the early 1980s. The current set of speckle reconstruction routines was written in IDL by O. von der L u e and J. Setiawan and then modified by K. Mikurda and F. W oger. The user-friendly version will be soon available to the whole solar physics community.

In the following section I will discuss the basics of the (extended) Knox-Thompson speckle reconstruction technique, our implementation of this method, as well as some results of the test performed on the simulated datasets and data obtained at the VTT.

### Knox-Thompson technique

In speckle imaging methods a sequence of  $N$  short-exposure images is analyzed. The Fourier transform  $F_i(\mathbf{s})$  of the  $i$ -th frame in the sequence can be written as

$$F_i(\mathbf{s}) = F_0(\mathbf{s}) S_i(\mathbf{s}). \quad (2.13)$$

where  $F_0$  is the Fourier transform of true, undisturbed object intensity distribution,  $S_i(\mathbf{s})$  is the instantaneous optical transfer function (OTF), and  $\mathbf{s}$  denotes a two-dimensional angular frequency expressed in units of an inverse angle ("line pairs per radian").

The object Fourier amplitudes are estimated from the average power spectrum as proposed by Labeyrie [1970]:

$$C(\mathbf{s}, \mathbf{0}) = \sum_{i=1}^N |F_i(\mathbf{s})|^2 = |F_0(\mathbf{s})|^2 \sum_{i=1}^N |S_i(\mathbf{s})|^2, \quad (2.14)$$

and the phases are estimated using the Knox-Thompson average cross spectrum Knox and Thompson [1974]:

$$C(\mathbf{s}, \boldsymbol{\delta}) = \sum_{i=1}^N F_i(\mathbf{s}) F_i^*(\mathbf{s} - \boldsymbol{\delta}) = F_0(\mathbf{s}) F_0^*(\mathbf{s} - \boldsymbol{\delta}) \sum_{i=1}^N S_i(\mathbf{s}) S_i^*(\mathbf{s} - \boldsymbol{\delta}). \quad (2.15)$$

$\boldsymbol{\delta}$  is a shift in the frequency domain and the upper index  $*$  denotes complex conjugation. All terms remain finite up to the diffraction limit  $D/\lambda$  so long as  $N$  is large (typically 100) and the magnitude  $\delta$  of  $\boldsymbol{\delta}$  does not exceed the seeing cutoff  $r_0/\lambda$  [Knox and Thompson, 1974, von der L u e, 1993]. Knox and Thompson also showed that the average cross spectrum contains unbiased information on the object phase gradient from which the object phase can be recovered using two-dimensional quadrature algorithms. The expression  $\langle |S_i(\mathbf{s})|^2 \rangle$  in Eq. 2.14 is called "speckle transfer function" (STF).

The original Knox-Thompson technique produces two cross spectra with two orthogonal fre-

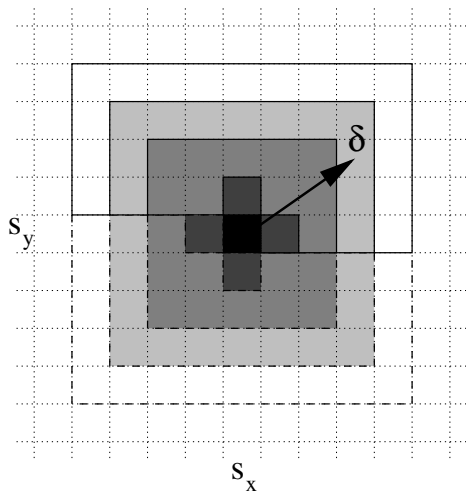


Figure 2.3: Neighborhood of pixel  $\mathbf{s} = (s_x, s_y)$  in the Fourier domain, showing the region covered by the shift vectors  $\delta_k$ . The black panel represents frequency  $\mathbf{s}$ . The gray pixels represent discrete frequencies addressed by shift vectors  $\delta_k$  for  $r_{\max}$  equal to 1 (dark gray), 2, (middle gray), 3 (light gray) and 4 (white). Only the upper half region, surrounded by solid lines, is addressed during the averaging and initial integration steps; the entire area is used for the iterative phase reconstruction steps.

frequency shifts  $\delta_x$  and  $\delta_y$ , this technique was also implemented in the earlier versions of KISIP. The difference between the standard and extended Knox-Thompson (EKT) algorithms as implemented in KISIP V is the number of frequency shifts used for object phase retrieval. KISIP V permits to use two shifts and more, up to as many as fit within the seeing limit area. The number of shifts is a function of the field size - which determines the resolution in the Fourier domain - and can be as large as a few dozen, because the algorithm is able to assemble the many phase differences into a unique object phase. The maximum limit  $r_{\max}$  of the frequency shift  $\delta_k$  can be chosen by the user. Fig. 2.3 demonstrates which discrete frequencies are used to calculate the cross spectra  $C(\mathbf{s}, \delta)$ .

An initial phase integration step is followed by iterative successive over-relaxation of the solution phase in order to minimize errors. The mean phase change between iterations is typically 0.01 radians after 10 to 20 iteration steps. An estimate of the mean phase noise based on the speckle signal-to-noise ratio and the number of phase differences is used for a stopping criterion, as well as an upper limit on the number of iterations performed.

As the last step amplitudes calculated from Eq. 2.14 are calibrated for the noise and atmospheric seeing. The first is performed with the Wiener filter, the latter by dividing the amplitudes by model STF calculated for the previously estimated Fried parameter  $r_0$  [von der Luhe, 1993, Mikurda and von der Luhe, 2006].

Speckle reconstructions can be computed only for fields of view (FOVs) not exceeding an isoplanatic path (typically a few arcsec). In order to minimize anisoplanatic effects, a large field of view is divided into several, overlapping subfields which are reconstructed individually and then recombined [von der Luhe, 1993].

Further details on our implementation of the EKT can be found in a forthcoming paper [Mikurda and von der Luhe, 2006]

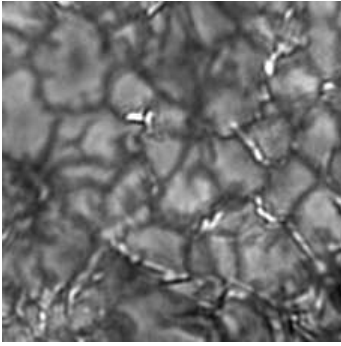


Figure 2.4: Sample input image (set 1) used for the simulation of the speckle bursts, showing solar granulation with several G band bright points. The field of view is  $13 \times 13$  arcsec.

### Tests on the simulated data

To test the performance of KISIP we simulated time series of solar granulation images. As an input we used five G-band (430.5 nm) images taken at VTT. The images show various solar scenes: from a quiet granulation to a sunspot penumbra. The field of view of every image is 13 by 13 arcsec. Using the input images we created speckle bursts representing different seeing conditions. The Kolmogorov model of an atmospheric turbulence with the phases being complex random numbers was used. The simulated exposure time was 10 ms and each burst consists of 100 single frames. The telescope diameter was set to 700 mm.

The input image for the first data set is shown in Fig. 2.4. Fig. 2.5 presents the results of the speckle reconstruction for this solar scene. The burst have been simulated for Fried parameters  $r_0 = 5, 7, 10, 15, 20$  cm (from top to bottom) and the best single image of a given burst, the average of the whole burst ("long exposure"), "raw reconstruction" (not corrected for seeing and noise effects) and final reconstruction are displayed (from left to right). The "raw reconstruction" was obtained by combining the uncalibrated Fourier amplitude  $\sqrt{C(\mathbf{s}, \mathbf{0})}$  with the reconstructed object phase  $P(\mathbf{s})$  and represents the 'average short exposure'. Note that all small scale information is already present in the 'raw reconstruction'. The calibrated reconstructions do not differ very much in contrast, despite the quality difference of the input data, which indicates that the speckle imaging process is quite robust against variations of the Fried parameter.

There are several ways to compare the reconstruction with "true" images. The most interesting question is how the quality of the reconstruction depends on the seeing conditions. In order to allow for a fair comparison the reconstructed and input images were coaligned and a 16 pixels wide strip was removed at the edges to avoid possible edge effects. The mean values of the remaining images were then normalized to 1.

A linear regression was performed in order to estimate the error minimizing parameters  $a, b$ :

$$E^2 = \frac{1}{A} \sum_{\mathbf{x}} \left( \hat{I}_0(\mathbf{x}) - a - bI_0(\mathbf{x}) \right)^2, \quad (2.16)$$

where  $\hat{I}_0(\mathbf{x})$  and  $I_0(\mathbf{x})$  are the speckle reconstruction and cropped input image, respectively, and  $A$  is the area of the images.

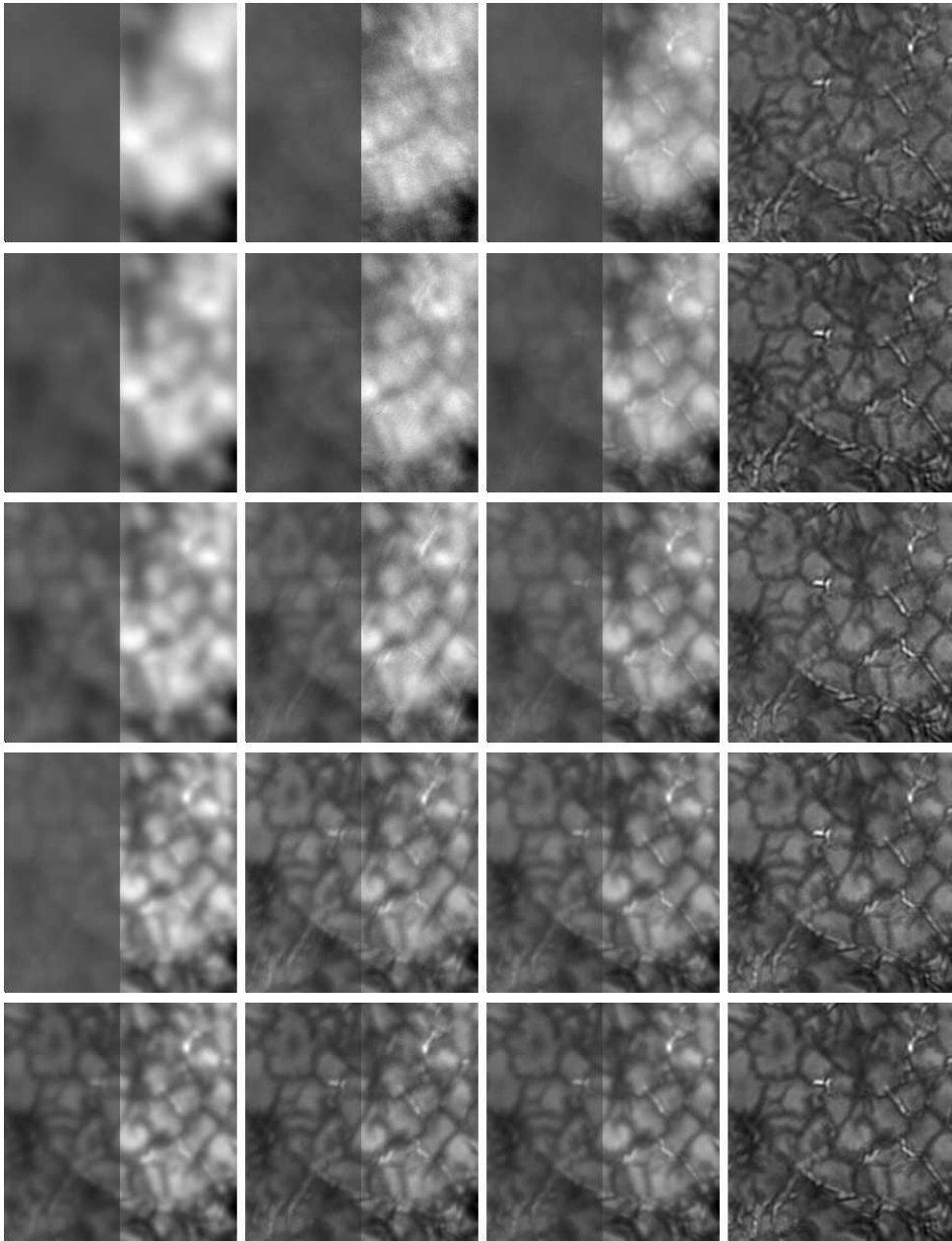


Figure 2.5: Speckle reconstructions of synthetic bursts with (from left to right column)  $r_0 = 5$  cm, 7 cm, 10 cm, 15 cm, and 20 cm. The columns show, from left to right: the best single frame of the burst, the average of all 100 frames (“long term exposure”), the reconstructed image without amplitude calibration (“raw reconstruction”), and the seeing and noise calibrated reconstructed image. The left halves of the panels are shown with a common gray scale to display the differences in contrast of the simulated data. The right halves are scaled individually to bring out the small details

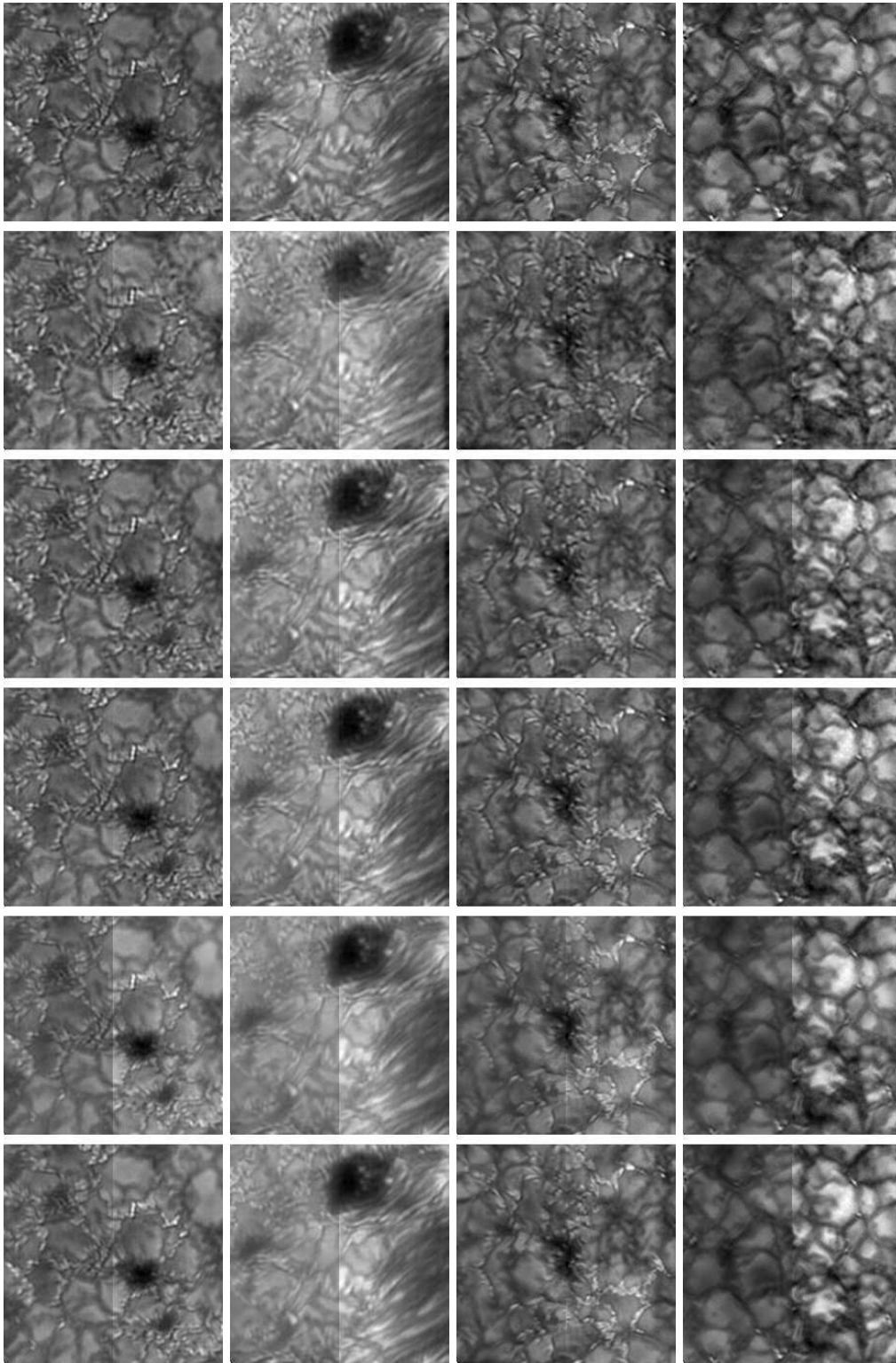


Figure 2.6: Speckle reconstructions of synthetic burst sets 2 (first column) to 5 (last column). The sets represent: 2 – pore, 3 – edge of sunspot with penumbral filaments, 4 – active region granulation, 5 – quiet region granulation. From top to bottom: input image and  $r_0 = 5$  cm, 7 cm, 10 cm, 15 cm, and 20 cm, respectively. The left halves of the panels are shown with a contrast scale which is common for each column while the right halves are scaled individually for each panel.

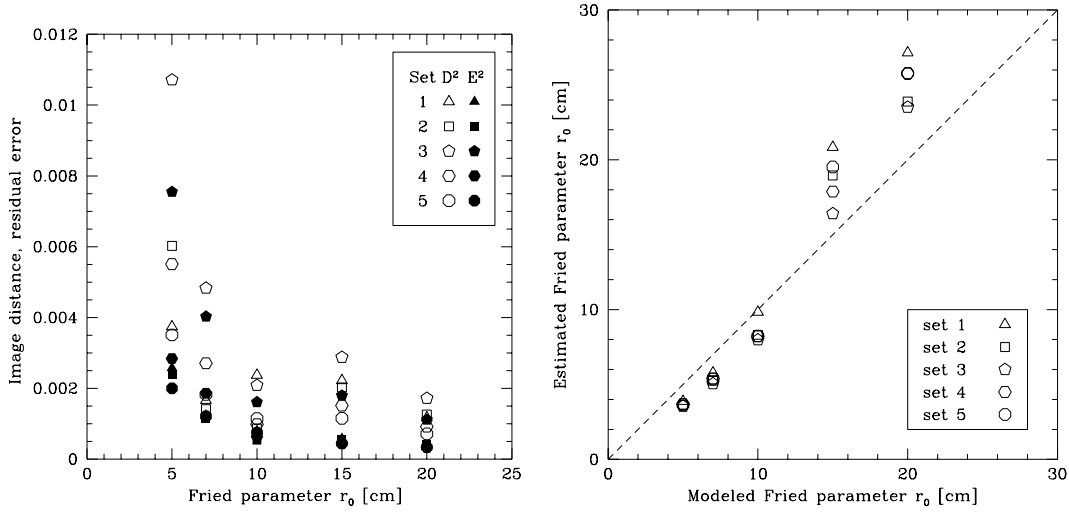


Figure 2.7: Left: image distance  $D^2$  and error  $E^2$  for all data sets and seeing qualities. Right: estimated vs. modeled Fried parameter for all data sets and seeing qualities.

As a second parameter, the Euclidean image distance of input and reconstructed images was determined,

$$D^2 = \frac{1}{A} \sum_{\mathbf{x}} \left( \hat{I}_0(\mathbf{x}) - I_0(\mathbf{x}) \right)^2. \quad (2.17)$$

The image distance is a measure of a reconstruction quality: the more similar are the input and reconstructed images, the smaller  $D^2$  becomes. Fig. 2.7 (left) shows the result of the image distance  $D^2$  and error  $E^2$  calculations for all the scenes and seeing conditions. The image distance is systematically lower for the reconstructions with larger Fried parameters. The sunspot penumbra scene is characterized with the largest  $D^2$ , probably because of the complexity of the reconstructed structure.

Fig. 2.7 (right) shows the Fried parameter estimated from simulated data using the spectral ratio technique [von der Lühe, 1984] implemented in KISIP V plotted against the input Fried parameter. The Fried parameter up to  $r_0 = 10$  seems to be very well recovered, but Fried parameters above 10 cm are overestimated. It is caused by the fact that the spectral ratio technique is based on Korff's STF theory [Korff, 1973] that is best applicable for moderate seeing conditions ( $r_0/D < 0.3$ ).

The simulated data presented here are isoplanatic. It is the reason why the influence of the subfield size on the quality of the reconstruction could not be tested. For this test the data was reconstructed using a subfield size of 7 arcsec, which corresponds to nine overlapping subfields across the field of view.

### Tests on real data

The quantitative analysis of an reconstruction of real data is more difficult, because there is no knowledge about the true object. Instead, the reconstruction can be performed on the same data with varying input parameters (i.e. subfield size, phase radius) and the results tested for an rms contrast, artefacts etc. In this way the best set of parameters for a reconstruction can be found.

The data presented here was taken on June 02, 2003 at the VTT. A DALSA CA-D7 camera with 1024 by 1024 pixels, observing at the G-band, was used. The exposure time was 10 ms and the data was taken with the maximum frame rate of  $7\text{ s}^{-1}$ . It took 100s to take and write to a hard disk a burst consisting of 100 frames. The observed sunspot was part of the active region NOAA 10373. The field of view was 58 by 58 arcsec and the image scale was 0.056 arcsec/pixel.

I used this data to demonstrate the influence of subfield size and subfield apodization width on the reconstruction. The result is shown in Fig. 2.8 (effects of the choice of the subfield size) and 2.9 (effects of the choice of the apodization window).

The anisoplanatism effects are clearly seen in the reconstruction with the subfield size of  $58 \times 58$  arcsec (full field of view). The somehow "grainy" structure has its origin in a transfer of a speckle signal to neighbor frequencies (pixels in the Fourier domain, see von der Lühe [1985]). In this case the information from neighbor pixels is not independent, so the phases reconstruction is affected.

The artefacts are also seen in the reconstruction with a subfield size of 3.5 arcsec. The reason for that is following: the size of the frequency step between pixels in the Fourier domain increases as the subfield size decreases. The consequence is a decrease of the cross-spectrum signal [von der Lühe, 1988] and when the step between pixels approaches the seeing limit  $r_0/\lambda$ , its magnitude is only about 20% of the mean power spectrum.

The right choice of the subfield size is then a trade-off between keeping it large enough for the smallest frequency difference being smaller than the seeing cutoff frequency and small enough to avoid anisoplanatic effects.

The choice of the subfield apodization window size is very important for the reconstruction of the extended sources, too, because it prevents the effects of uncorrelated structures at opposite edges of the subfield. In order to avoid discontinuities, the apodization of the field must be large enough (typically more than 10% of the field).

Fig. 2.9 demonstrates the effect of the apodization choice on the reconstruction quality. The optimum apodization is in most cases between 10 and 40%.

Fig. 2.10 shows the result of the reconstruction with the optimal set of parameters. For comparison, the best single frame of the burst, the average of the whole burst and the 'raw reconstruction' are presented.

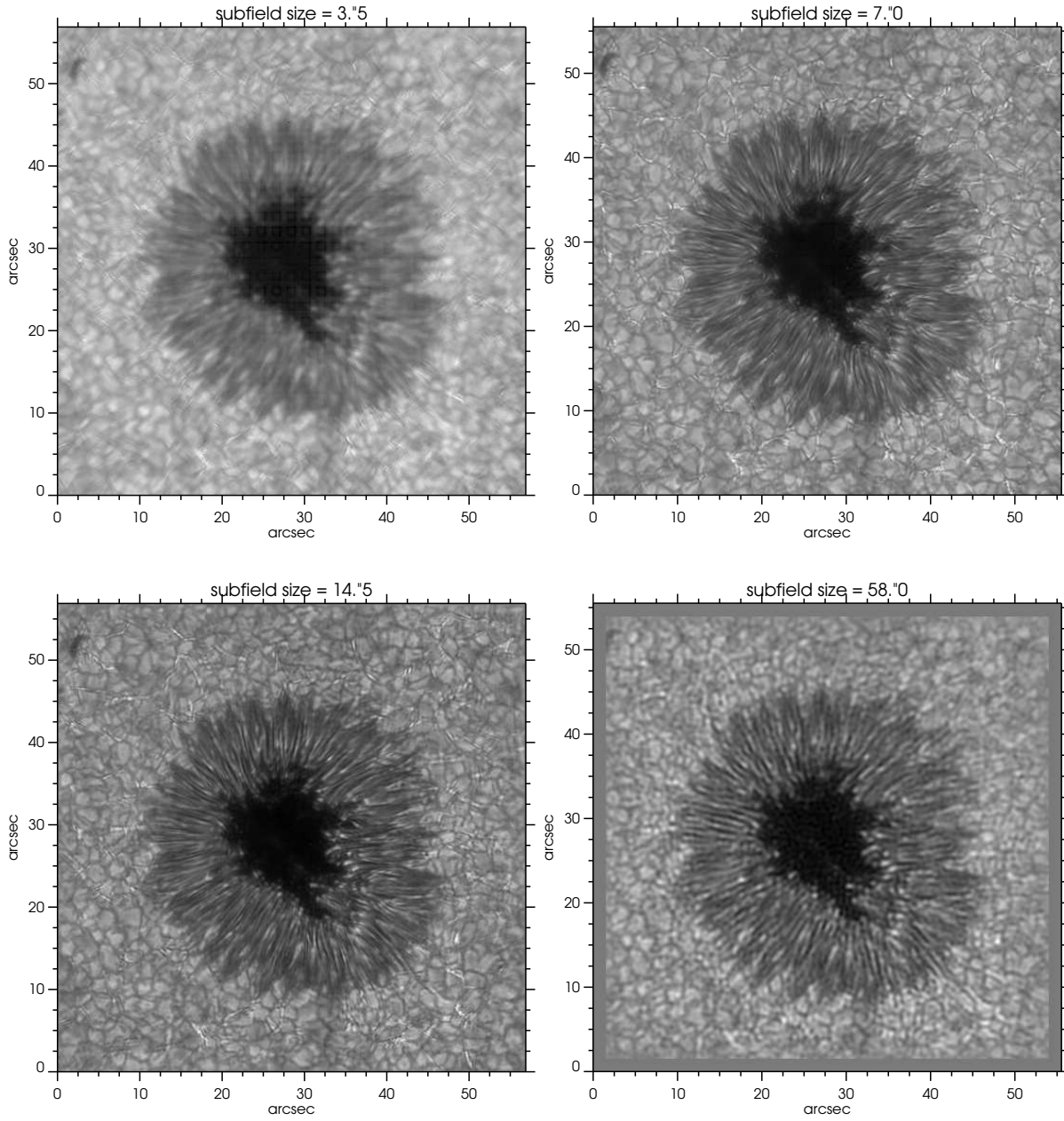


Figure 2.8: Reconstruction of the same speckle burst with various subfield sizes. 58×58 arcsec corresponds to the full field of view.

## 2.3 Speckle reconstruction and adaptive optics

In KISIP V the Fried parameter is estimated individually for each subfield in order to account for a field dependent seeing quality. This approach is useful when data are taken with partially compensating adaptive optics, such as the KAOS at the VTT. The full field of view of data presented in the previous sections is almost one arcmin, much larger than the isoplanatic area compensated by KAOS, which is of the order of 10 arcsec.

There is a field gradient of image quality with growing distance from the wavefront sensor lock point, the further from the lock point the worse the quality. To first order, this gradient can be approximated with a field-dependent, “modified” Fried parameter  $\rho_0$  [Cagigal and Canales, 2000]. KISIP V interpolates the conventional Korff STF for a seeing parameter  $\alpha = \rho_0/D$  at each field position and adjusts the amplitude calibration accordingly.

This approach gives satisfactory results according to the experience made with KISIP at the Kiepenheuer-Institut, but this issue of course requires a much more thorough analysis. Work is in progress to understand how a STF is modified by the use of adaptive optics.

## 2.4 The summary

### ...or how to get a good speckle reconstruction ?

As already mentioned, several factors can influence the quality of a speckle reconstruction. In practice, a trade off is sometimes needed , for example between a short exposure time and a sufficient signal-to-noise ratio. The list below contains the most important factors that need to be taken into account to obtain a decent speckle reconstruction:

- the exposure time should be shorter than the atmospheric coherence time  $\tau_0$ ;
- an interval between two exposures need to be larger than  $\tau_0$  in order to assure that each frame represents a statistically independent state of the turbulence;
- the number of frames in the burst should be large enough (see the commentary to Eq. 2.15), but taken in a time shorter than the characteristic time for changes on the Sun (depends on a wavelength and a telescope diameter);
- “subfielding” must be performed in case of anisoplanatic fields of view;
- the spectral bandwidth should not be too large (typically  $\Delta\lambda/\lambda < 0.1$ ) in order to keep a sufficient degree of coherence.

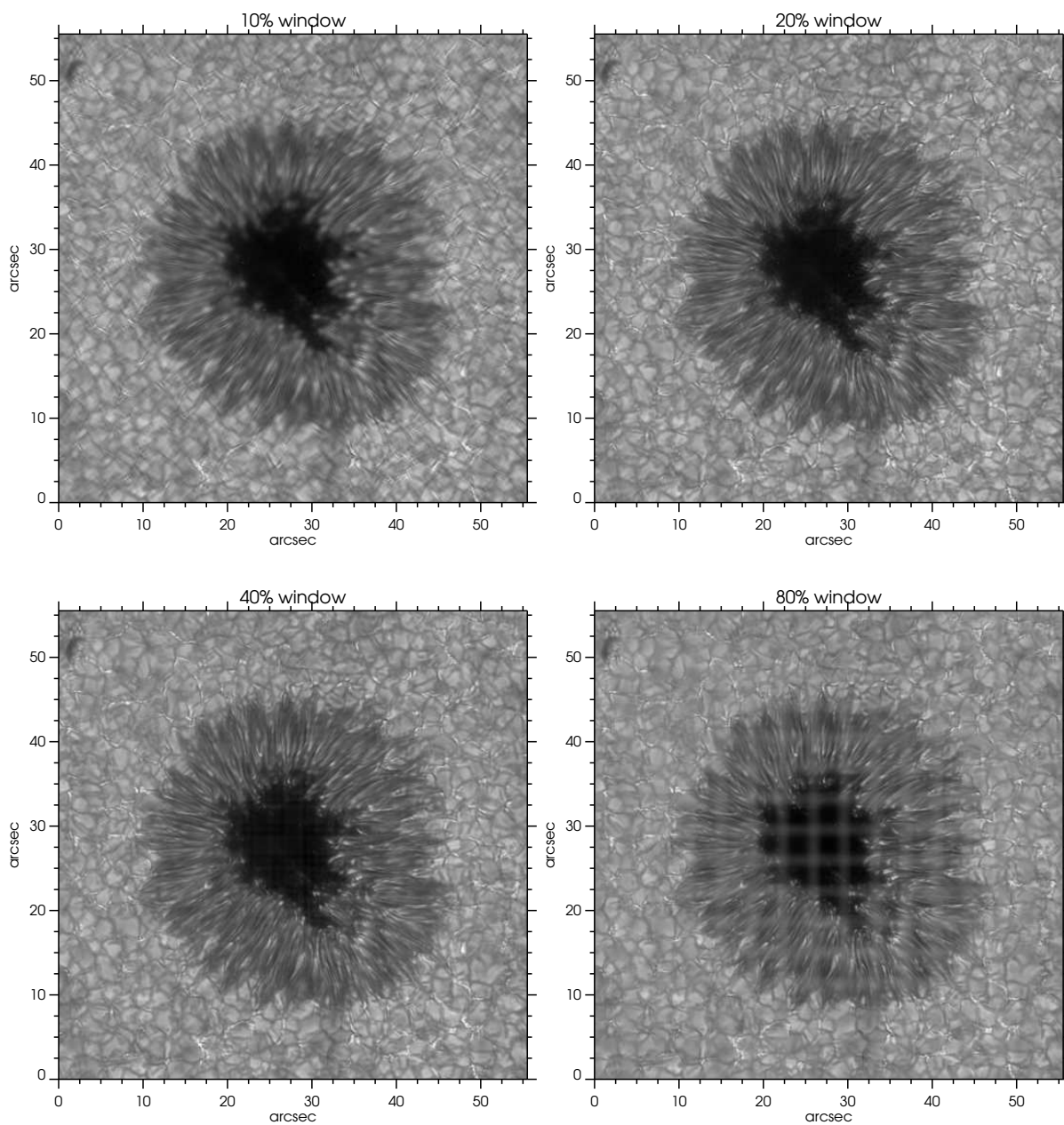


Figure 2.9: Reconstruction of the same speckle burst with various apodizing fractions.

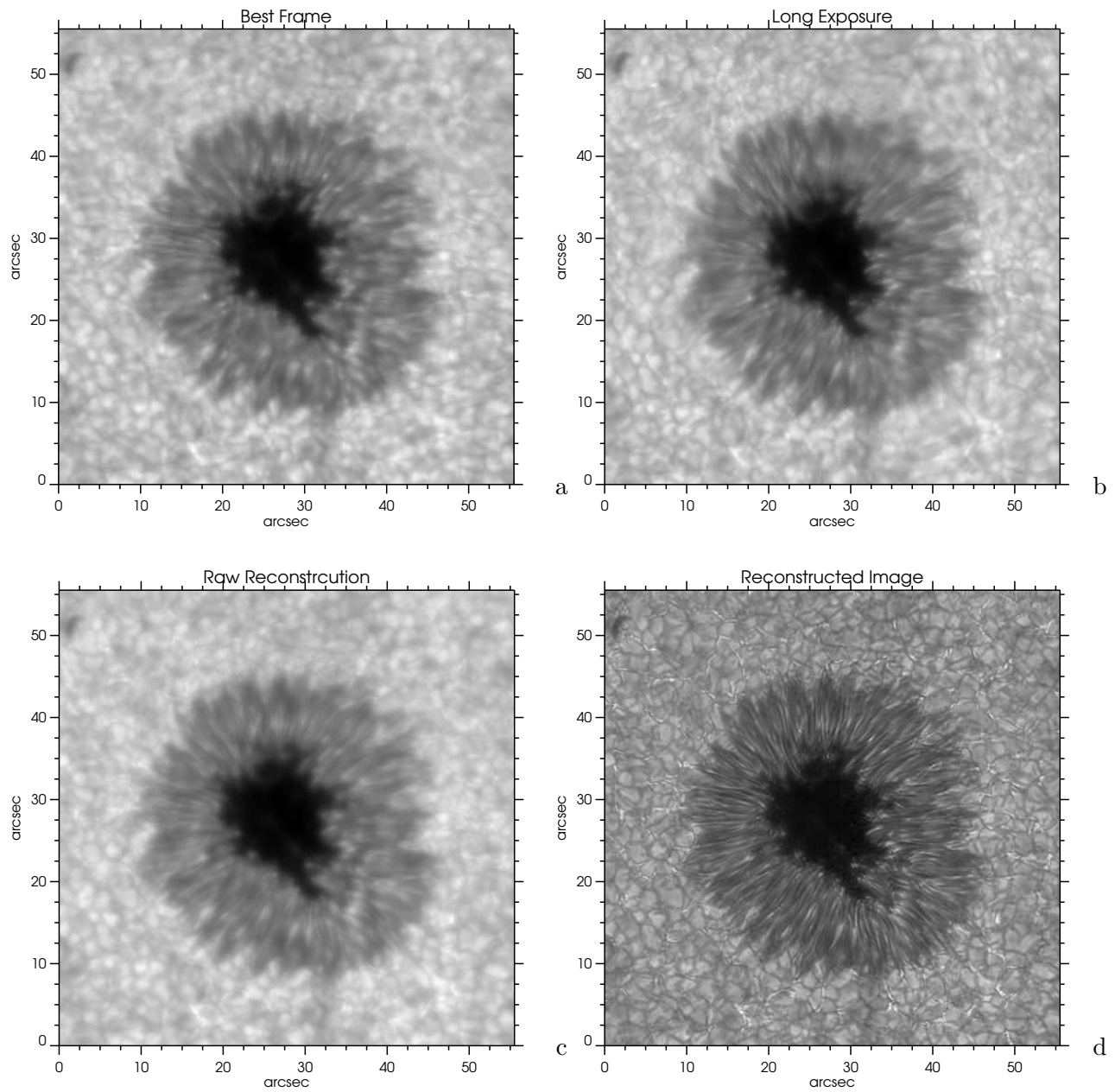


Figure 2.10: Reconstruction of the part of active region NOAA 10373 with the optimal set of parameters. a: the frame with the highest contrast of the burst, b: 100 frame average, c: "raw reconstruction", d: final reconstruction.



## Chapter 3

# Two-dimensional solar spectroscopy

Spectroscopy is one of the most important tools of observational solar physics. It provides information on several physical parameters like velocity, temperature, magnetic field strength etc. The combination of these parameters gives the solar physicist the information about the state of the solar atmosphere.

The intensity as a function of four parameters is needed: two spatial coordinates, time and wavelength. The two most established observational narrow-band techniques: photometry and longslit spectroscopy cover only three of the four parameters. While photometry with usage of a CCD camera can cover a large field of view at a very good temporal resolution, it does it at a fixed wavelength. On the other hand, slit spectrograph records wavelength-dependent intensity at a fixed spatial coordinate perpendicular to the slit. Covering larger fields of view requires scanning of the solar image across the slit. It is usually time consuming and can corrupt the data, because both the solar surface (especially on sub-arcsecond scale) and seeing evolve during the scan.

Several authors argued that it is necessary to develop two-dimensional spectroscopic techniques [see e.g. Keller et al., 1990, Johanneson et al., 1992, Collados et al., 1996] in order to investigate physical parameters (Doppler velocity, magnetic fields etc.) of sub-arcsecond structures. The answer are tunable filter instruments employing either tunable Lyot filters, Michelson interferometers (MFI), Fabry-Perot interferometers (FPI) or a combination of them. Currently operating solar tunable filter instruments are listed in Tab. 3.

The big advantage of a classical grating spectrograph is its very high spectral resolution. As already mentioned, slit spectrographs take the whole spectra at a time and scan perpendicular to the slit in order to get the information in the second spatial coordinate. In case of tunable filter instruments with a high spectral resolution, the scanning is performed across the spectral line and a two-dimensional filtergram is obtained at each step. The individual narrow-band filtergrams are then combined to a full 2-D spectrogram. The main limitation of this technique is the time needed to perform a scan, since the temporal evolution of the solar surface has to be taken into account.

Name	Location	Type	References
'Göttingen' FPI	VTT, Tenerife	FPI	Bendlin et al. [1992]
H $\alpha$ tunable filter	DOT, La Palma	Lyot	Bettonvil et al. [2003]
Interferometric BIdimensional Spectrometer, IBIS	THEMIS, Tenerife	FPI/Lyot	Cavallini and et al. [2000]
Michelson Doppler Imager, MDI	Soho	Lyot/MFI	Scherrer et al. [1995]
Solar Optical Universal Polarimeter, SOUP	SVST, La Palma	Lyot	Title and Rosenberg [1981]
TElecentric SOLar Spectrometer, TESOS	VTT, Tenerife	FPI	Tritschler et al. [2002]
Chromospheric Helium I Imaging Photometer, CHIP	MLSO, Hawaii	Lyot	
Universal Birefringent Filter	Dunn Solar Telescope, Sacramento Peak, USA	FPI/Lyot	Bonaccini et al. [1989]

Table 3.1: Currently operating solar tunable filter instruments (in alphabetic order)

### 3.0.1 2-D solar spectra from TESOS

Spectroscopic data presented in this thesis was taken with the Fabry-Perot Interferometer TESOS [Kentischer et al., 1998, Tritschler et al., 2002, TElecentric SOLar Spectrometer, ] located at the VTT, Tenerife.

Fig. 3.1 shows the profile of the neutral iron line at 557.6 nm obtained with TESOS. A two-dimensional filtergram is recorded at each wavelength step and this information is then used to create a line profile (similar to the one in Fig. 3.1) at each pixel of the field of view. More details about TESOS can be found in Appendix A.1.

## 3.1 Speckle deconvolution of 2-D spectra

Speckle reconstruction techniques are widely used to improve the quality of filtergrams. However, in order to obtain good results with those techniques a high signal-to-noise ratio (SNR) is needed. This is usually obtained by using filters with broad (1 nm or more) transmission band which provide enough photons even if observing with short exposure times required by the speckle imaging (about 10 ms).

The situation becomes different when observing with bandwidths below 0.1 nm. When, in addition, pixel sizes are small (in order to achieve the desired spatial resolution), the number of photons would not be sufficient to apply one of those techniques.

Keller and von der Lühe [1992] proposed the following solution of this problem: simultaneous broad-band and narrow-band images close-by in wavelength should be taken and speckle imaging performed for the broad-band channel data only. Combining the reconstruction and the single broad-band images gives information on the instantaneous state of the Earth's atmosphere. This

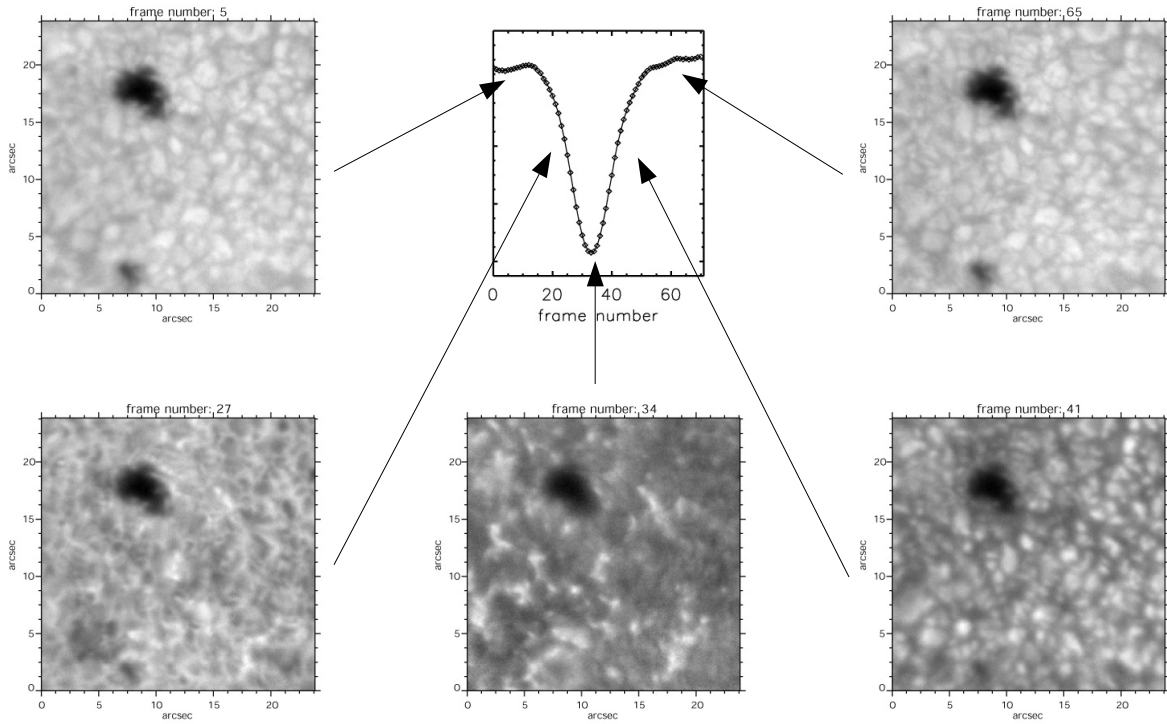


Figure 3.1: The profile of the Fe I spectral line at 557.6 nm obtained with TESOS and filtergrams taken at selected wavelength positions.

information is then used to correct the single narrow-band images.

In the following sections I will discuss this method in more detail and show its consequences for the photometric quality of the spectra.

### The method

The deconvolution method applied by me is similar to those of Keller and von der Lühe [1992] and Krieg et al. [1999].

Under isoplanatic conditions and for exposure times short enough to “freeze” the atmosphere, the observed intensity in the broad-band channel,  $i^b$ , and in the narrow-band channel,  $i^n$ , respectively, can be related to the corresponding true object intensities,  $o^b$ , and  $o^n$ , respectively, via a convolution with the point spread function (PSF):

$$i_j^b = o^b \star PSF_j^b, \quad i_j^n = o_j^n \star PSF_j^n, \quad (3.1)$$

where  $\star$  denotes the convolution operator. The index  $j$  ( $j = 0, \dots, 75$ ) is introduced to distinguish between the individual broad-band frames and thus different atmospheric realizations. In the narrow-band channel the index  $j$  indicates the number of different wavelength points and thus the number of different true objects  $o_j^n$ .

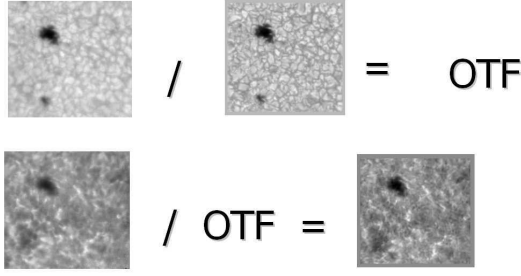


Figure 3.2: The principle of the speckle deconvolution technique. Upper line: from left to right: single broad-band image, speckle reconstruction of a burst of broad-band images. Bottom line: from left to right: single narrow-band image, reconstructed narrow-band image. In reality, all the images are Fourier-transformed. The data used to create this scheme is described in Sect. 3.2.1.

Assuming that the spectral bands of the broad-band and the narrow-band channel are close enough, the corresponding PSF's can be considered as identical for each time step  $j$ , and Eq. 3.1 can be translated into the Fourier domain as follows:

$$I_j^b = O^b \cdot OTF_j, \quad I_j^n = O_j^n \cdot OTF_j. \quad (3.2)$$

where capital letters denote Fourier transforms of the corresponding quantities in Eq. 3.1. The Fourier transform of PSF is called Optical Transfer Function (OTF). Theoretically, these two equations can be solved for  $O_j^n$ , by replacing  $O^b$  with the Fourier spectrum of the broad-band (“mother”) speckle reconstruction,  $\bar{O}^b$ , and calculating

$$\bar{O}_j^n = \frac{I_j^n}{I_j^b} \bar{O}^b. \quad (3.3)$$

This operation is schematically presented in Fig. 3.1.

However, in the presence of noise, which I have not considered so far, this approach fails and leads to an unwanted amplification of those parts of the signal spectrum that are dominated by noise. These regions exhibit a poor signal-to-noise ratio (SNR) and give rise to artifacts in the spatial domain of the restored intensity distribution. Typically, these are the high-frequency components of the spectrum. The result can be improved by multiplying Eq. 3.3 with the complex conjugate of the relevant broad-band Fourier spectrum,  $(I_j^b)^*$ , and perform an averaging process over several narrow-band filtergrams:

$$\bar{O}_j^n = \frac{\langle I_j^n (I_j^b)^* \rangle}{\langle |I_j^b|^2 \rangle + \langle |N_j^b|^2 \rangle} \bar{O}^b, \quad (3.4)$$

where  $\langle |N_j^b|^2 \rangle$  is the average noise level as deduced from the broadband images. I assume a frequency-independent (“white”) noise spectrum. Averaging is done over frequencies that are beyond the telescope cut-off frequency.  $N^b$  is the Fourier spectrum of the noise in the broad-band channel.

### Practical considerations

In practice, it is very important to find a trade-off between wavelength sampling and SNR, i.e. number of images per wavelength position, because the interval needed to take a single 2-D spectrum should stay below the characteristic time for changes on the Sun. This time scale depends on wavelength and spatial resolution and in a case of the data presented in this thesis it is about 30 s.

In the past, there were several approaches to this problem. Keller and von der Lühe [1992] took 100 images at single wavelength in about 30 s. In order to keep the scanning time short, Krieg et al. [1999] took 5 images at each of the 28 wavelength positions chosen to scan the Na  $D_2$  spectral line. Hirzberger and Kneer [2001] scanned Fe I line 557.6 nm at 11 wavelength positions with 10 frames per wavelength step, which results in a cadence of subsequent scans i.e. 2-D spectra of 70 s.

For the data presented in this thesis, I adopted a different approach: I performed a spectral sampling with equidistant steps of 0.84 pm and used five adjacent wavelength positions for the deconvolution. In a case of the data presented here, this averaging procedure has very little effect on reconstructed line profiles.

## 3.2 Photometric quality of speckle deconvolution

### 3.2.1 Observations

All the spectroscopic data presented in this thesis was recorded with the Fabry-Perot interferometer TESOS at the VTT. It was accompanied by the G-band imaging, all spectra analyzed here were taken in the Fe I line at 557.6 nm in the TESOS high resolution mode (circular FOV of 40 arcsec in diameter, spectral resolution  $\lambda/\Delta\lambda=250000$ ). The data set consists of 5 scans, the total time covered is 250 s. The line is sampled with equidistant steps of 0.84 pm at 76 wavelength points. The single exposure time was 15 ms and one scan was completed in 30 s. A prefilter centered at 557.6 nm, an FWHM of 1.1 nm and a maximum transmission of 70 % was used. Simultaneously to the narrow-band images, TESOS takes data in the broad-band channel, the filter used here had the central wavelength of 550 nm and FWHM of 10 nm. The image scale in the both channels is 0.09 arcsec/pixel.

The G-band imaging was performed by a relatively simple optical setup which was placed in front of TESOS. A dichroic beam-splitter plate was used to reflect any light  $<450$  nm onto a fast  $1k \times 1k$  pixel Dalsa camera. A filter centered around 430.3 nm and 1.0 nm wide was placed in front of the detector to isolate the G-band wavelength range. The FOV was  $57 \times 57$  arcsec and the image scale 0.055 arcsec/pixel. The G-band data was taken in bursts which were later used in the speckle reconstruction process and is quasi-simultaneous with the TESOS data. The G-band images were mainly used to locate the positions of photospheric bright points. More about it in Chapters 4 and 5.

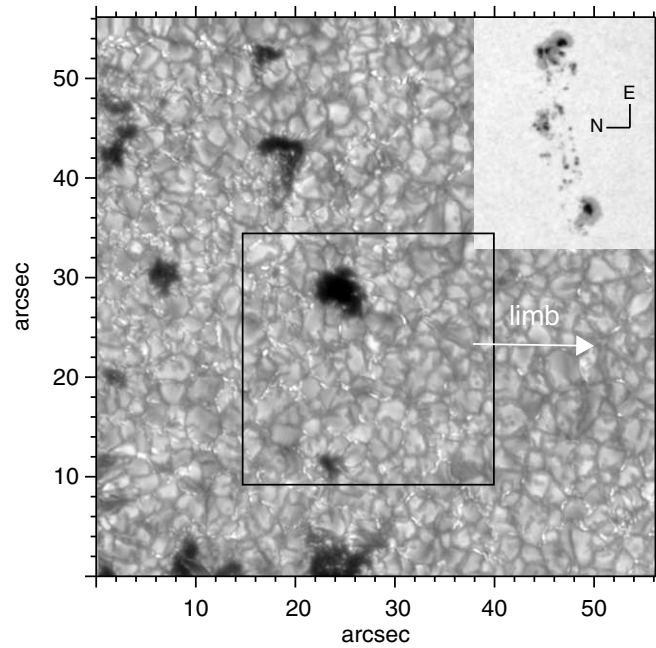


Figure 3.3: Speckle reconstructed G-Band image. The right square indicates the TESOS FOV. The arrow points toward the nearest solar limb. The inset in the upper right corner shows the complete active region AR10180.

Both FOVs covered a part of the active region AR 10180 located at  $\theta = 15.68^\circ$  ( $\mu = 0.96$ ) on the southern solar hemisphere. The FOVs of Dalsa and TESOS are shown in Fig. 3.3.

The observations presented here were made with the support of Kiepenheuer Adaptive Optics System.

### 3.2.2 Data reduction and reconstruction

Before performing the speckle reconstruction and deconvolution, several pre-processing procedures were performed: dark subtraction and gain correction at each individual wavelength step. The flat field images needed for the gain correction were taken by moving the solar image across the focal plane to smear out all solar structure. Slight differences in orientation and pixel image scale between the narrow-band and the broad-band channel of TESOS were determined from a comparison of grid target images. Thus, a rotation of  $-0.816$  deg and offset shifts of  $\Delta x = 0.57$  pixel and  $\Delta y = 0.87$  pixel were applied to the broadband images to match the narrow-band images. Furthermore, I corrected the broadband images for a 2% difference in image scale with respect to the narrowband images. Residual image motion during the scan was compensated by determining the image shifts from one broadband image to the next and shifting the simultaneous narrow-band images by the same amount. The intensity modulation pattern (see Appendix A.2) was removed by Fourier filtering leaving a residual variation on a 1-2% level in the local continuum intensity.

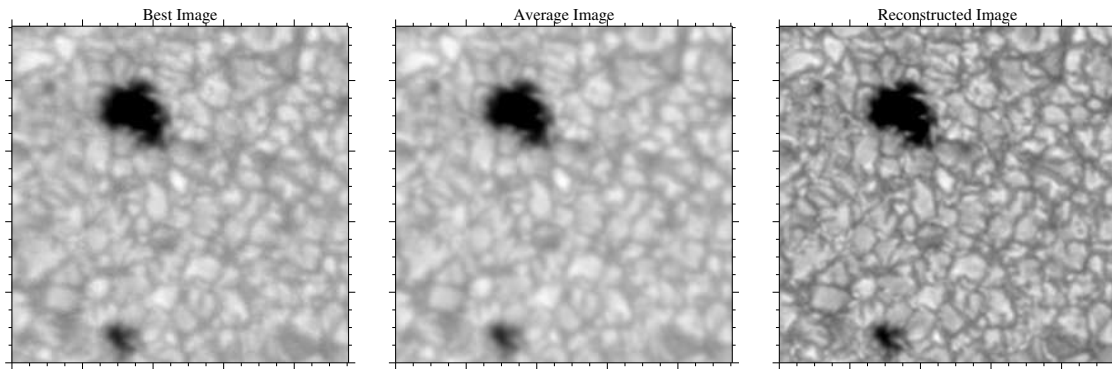


Figure 3.4: Left: Best broad-band image taken from first scan. Middle: Averaged broad-band image (over 76 images). Right: broad-band speckle reconstruction. One minor tick mark corresponds to one arcsec.

### Alignment with the G-Band images

The G-Band images have a different orientation and pixel image scale than the TESOS data. In order to identify locations of G-Band bright points in the TESOS data co-spatiality of the two data sets must be guaranteed. Therefore, in a first step, the G-Band data has to be rotated counterclockwise by  $270^\circ$  and mirrored. In a second step, the pixel scale of the G-Band data ( $0.055 \times 0.055 \text{ arcsec}^2$ ) is changed to match that of the TESOS data ( $0.089 \times 0.089 \text{ arcsec}^2$ ) by performing a linear interpolation. Finally, a residual rotation counterclockwise of about  $2^\circ$  is applied.

### Speckle reconstruction

The broad-band TESOS images and the G-Band images were speckle reconstructed using the Kiepenheuer Institute Speckle Imaging Package (KISIP). Figure 3.3 shows a result of the speckle reconstruction in the broad-band channel data simultaneous to the first scan of the time series: the best broad-band image of the burst, the average over the while burst and the speckle reconstruction. The enhanced contrast of the speckle-reconstructed image can be seen.

The speckle deconvolution of the narrow-band data was performed as described in Sec.3.1.

## 3.3 Results

Fig. 3.3 shows the result of the deconvolution process for the first scan. The un-restored filtergrams (corresponding to different position across the spectral line) are presented in the left column, while the right column contains corresponding speckle-deconvolved images. The filtergrams in the narrow-band continuum are reconstructed almost as efficiently as the broad-band images.

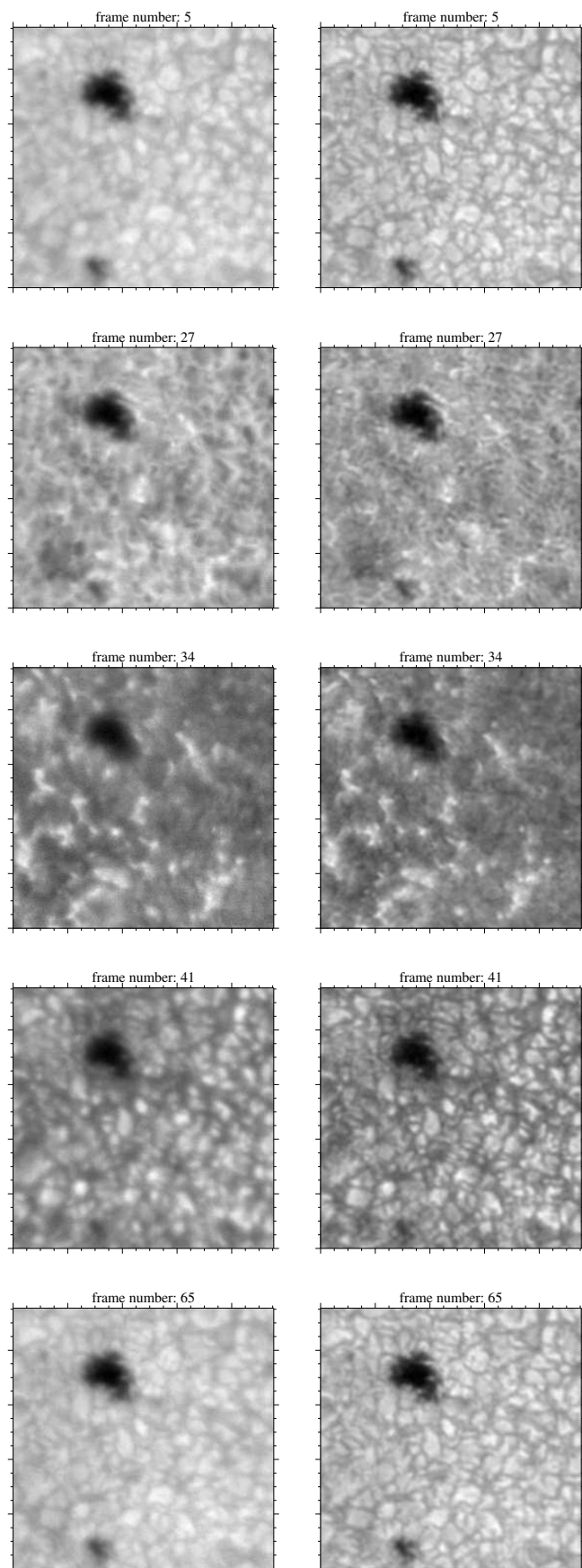


Figure 3.5: Left column: Narrow-band filtergrams before reconstruction. Right column: Narrow-band filtergrams after the speckle deconvolution process. Top to bottom: Blue continuum (frame number 5), blue line wing (27), line core (34), red line wing (41), and red continuum (65). One minor tick mark corresponds to one arcsec.

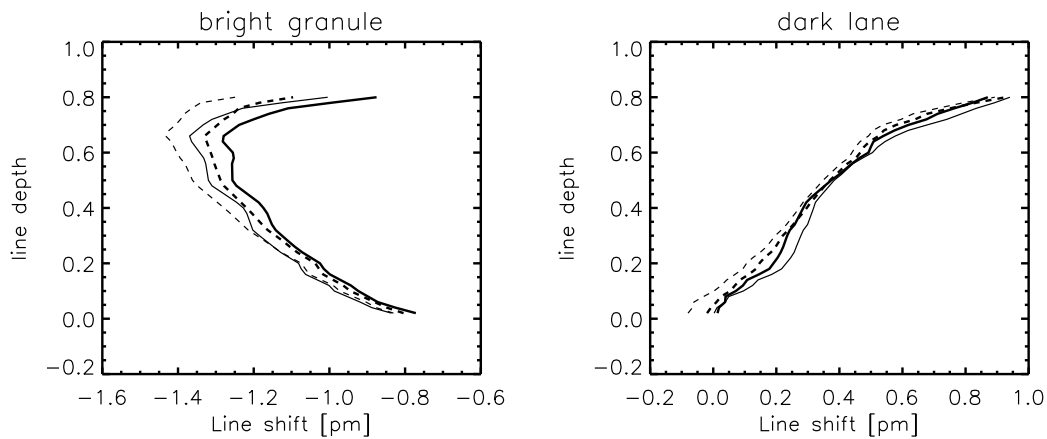


Figure 3.6: Bisectors before (dashed) and after (solid) the deconvolution process. Left: center of the granule. Right: intergranular lane. Thin lines: bisectors averaged over four pixels. Thick lines: bisectors averaged over nine pixels. Line depths of 0.0 and 1.0 correspond to the line center and the continuum, respectively. The meaning and definition of line bisectors are given in Sect. 3.3.3.

### 3.3.1 “Grainy pattern”

A closer look at the speckle-deconvolved filtergrams in Fig. 3.3 reveals the presence of a weak small-scale *grainy pattern*. The pattern is more pronounced in the line wing and line core and less obvious in the continuum. It appears at spatial scales close to the resolution limit, the grains span 2-3 pixels which corresponds to 0.18-0.27 arcsec. Such a pattern has been observed before in narrow-band image reconstructed data [see e.g. Krieg et al., 1999]. The origin of this pattern is still unclear: it is very likely caused by the lack of sufficient signal-to-noise ratio at spatial frequencies close to the diffraction limit, but on the other hand, it shows surprising temporal stability over the whole time sequence.

van Noort et al. [2005] observed a similar effect in the magnetograms reconstructed with the phase-diversity technique and concluded that it is due to noise and can be reduced by taking more frames at each wavelength position.

My main concern was, if the existence of the *grainy pattern* has any influence on the bisectors of single structures. As a test, I analyzed several line profiles and the corresponding bisectors (cf. Sect. 3.3.3) of individual structures. In Fig. 3.6 two typical bisectors (for a bright granule and an intergranular) before (dashed) and after the deconvolution (solid) are displayed. The bisectors are averaged over four (thin lines) and nine pixels (thick lines), respectively. Apparently, there are no significant differences in the bisectors before and after the deconvolution process and moreover, increasing the averaging area does not significantly change the result. This observation allows to conclude that the presence of the *grainy pattern* in general does not change the spectral information.

### 3.3.2 Difference between the blue and red wing of 557.6 nm Fe I line

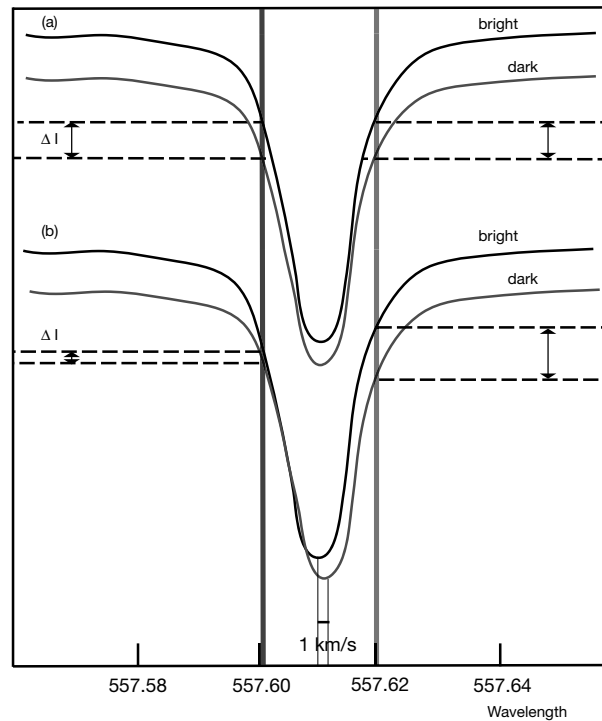


Figure 3.7: Intensity change in the line wings due to Doppler shift. The lower curves show line profiles of bright granules and dark intergranular regions with a Doppler shift of  $1000 \text{ m s}^{-1}$ . Note the intensity contrast enhancement in the red wing and the strong decrease in the blue wing. The upper curves show the same profiles without any line shift for comparison.

The filtergrams taken in the blue wing of the spectral line are quite different from those obtained in the red wing at the same line depression (compare 27 and 41 in Fig. 3.3). The different appearance of the filtergrams is a natural consequence of the correlation between convection and radiation.

Figure 3.7 illustrates this effect schematically: in the red wing, the Doppler shift enhances the intensity contrast of the granulation, because the blue shift of the bright granules leads to an enhanced intensity, whereas the red-shifted dark regions appear even darker. In the blue wing, the effect is exactly opposite. If the line shift is sufficiently high, the intensity contrast may even be reversed here. A similar effect was already observed for other photospheric spectral lines, for example Ba II at 455.4 nm [Sütterlin et al., 2001a].

To show that it is really this mechanism that causes the large difference between the blue and red wing of the analyzed spectral line, I removed the Doppler shift of the line core by shifting the position of the spectral line to a common position at every pixel. The result is illustrated in Fig. 3.8 for the deconvolved filtergrams. There is almost no difference between both wings, except some residual differences due to line asymmetries which I did not account for.

It has also to be mentioned that the  $\tau = 1$  surface is influenced by both thermal and Doppler effects causing a wide range of line shifts, line widths and line asymmetries [e.g. Stein and Nordlund, 1998, Asplund et al., 2000b]. The temperature gradient above the granules is steeper, as a consequence the line profiles are stronger and narrower. The temperature gradient above intergranular lanes tends to be shallower leading to weaker and broader line profile. These effects introduce additional difference between the blue and red shifted line profiles.

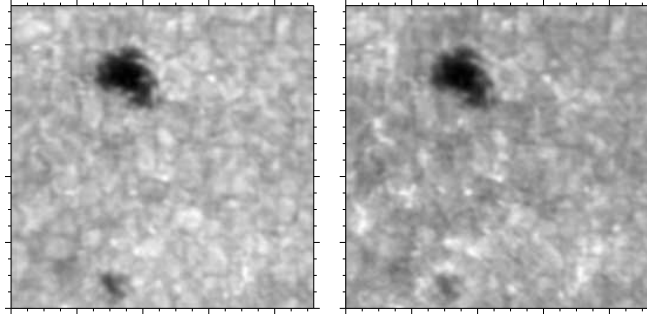


Figure 3.8: Reconstructed filtergrams taken from the blue (left panel) and red wing of the line profile. Prior to the image reconstruction, the spectral line was shifted to a common position at each pixel. One major tick mark corresponds to five arcsec.

### 3.3.3 Influence of the speckle deconvolution on the spectral lines

As already mentioned, speckle deconvolution methods are widely used, but so far, to my knowledge, no analysis on the influence of the reconstruction process on spectroscopic data has yet been published. Therefore I performed a detailed spectral analysis of the line profiles before and after reconstruction and investigated the following properties of the profiles: line position, depth and asymmetry (characterized in form of line bisectors). This was done for the average line profiles of some characteristic solar structures, as well as for individual profiles.

In order to identify the region of interest: granules, intergranular lanes and the central part of the pore I constructed three binary masks (see Fig. 3.9). The masks for bright granules and dark lanes were created by setting the appropriate intensity threshold values to the quiet granulation in the reconstructed broad-band image. The masks were used to calculate the mean line profiles and bisectors of the region of interest.

The pre-processed and reconstructed data cube leaves us with a line profile sampled at 71 wavelength points. In order to allow for a fair and direct comparison between the data before and after the deconvolution process, a box-car average over five images is performed to the un-restored data cube (76 wavelength points). In this way, both data cubes have the same number of wavelength points.

The line asymmetry can be quantified by the bisector, i.e. the line segment connecting the midpoints of the spectral line from the core to the continuum (see Fig. 3.3.3. A line bisector

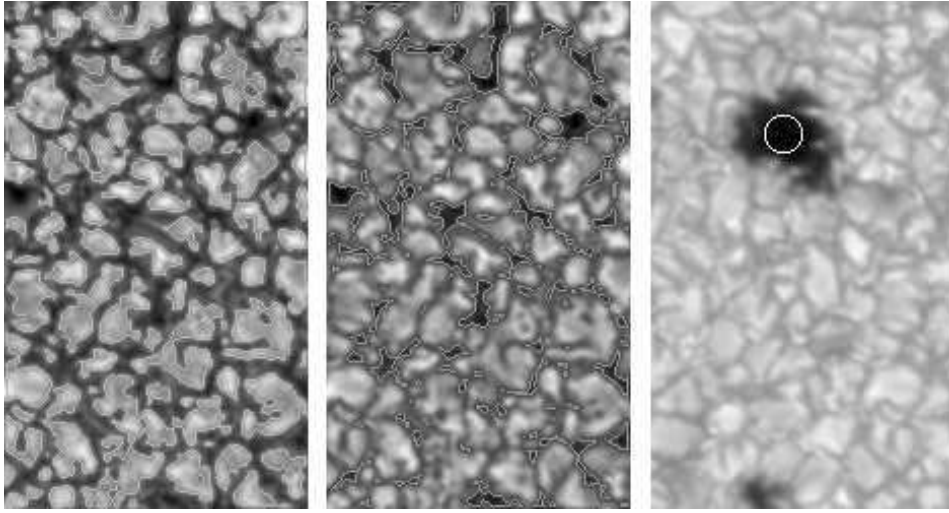


Figure 3.9: Contours of the binary masks used to calculate the mean line profiles and bisectors presented in Fig. 3.11. From left to right: bright granules, dark lanes and the central part of the pore.

analysis is performed for each averaged line profile, 40 bisector positions are calculated at intensity levels between 2% and 80% of the line depression. Line depths of 0.0 and 1.0 correspond to the line center and the continuum, respectively. Bisector levels larger than 80% are not taken into account since the bisector positions in the extreme line wings are very sensitive to noise. Red-shifts are positive and blue-shifts - negative. The line core position of the central part of the pore serves as velocity reference.

The spatially averaged line profiles (upper row) and the corresponding mean bisectors (bottom row) from the five individual scans are displayed in Fig. 3.11. To demonstrate the effect of the reconstruction process, the corresponding data before (dashed) and after the deconvolution process (solid) are plotted. The line profiles are normalized with respect to the local continuum intensity of the averaged granulation.

The reconstructed mean line profile for the brightest granules in the FOV (Fig. 3.11, upper panel, left) shows an enhanced continuum intensity and narrower wings. For the darkest intergranular lanes, the deconvolution leads to a decrease of the continuum intensity and broader wings. This result can be expected: bright structures become brighter and dark structures become darker by the deconvolution process.

A close inspection of the of bisector shapes before and after the deconvolution proves that line asymmetries are preserved (bottom row). Differences in bisector shapes are visible in the (far) wing only, reflecting the broadening and narrowing of the line profiles due to the deconvolution. This can be understood in terms of an increase of the spatial resolution which has been already predicted from the simulations of solar magneto-convection [Asplund et al., 2000a, Stein and Nordlund, 2003].

The spatially averaged line profile of the darkest part of the pore shows in fact the same ten-

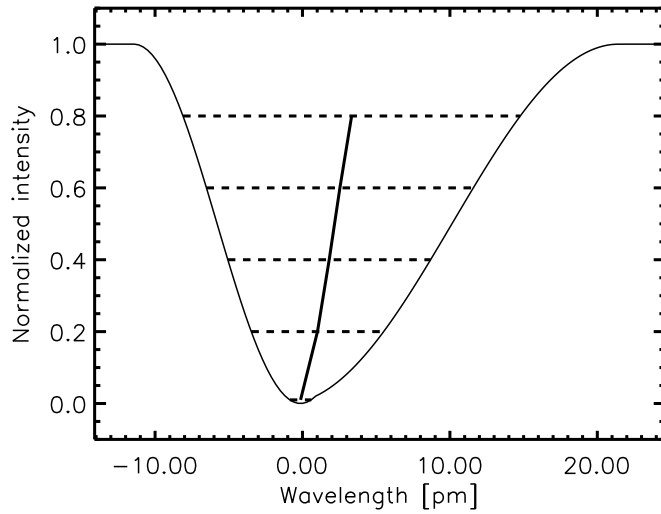


Figure 3.10: Schematic representation of a spectral line bisector (thick lines). Dashed lines represent intensity levels.

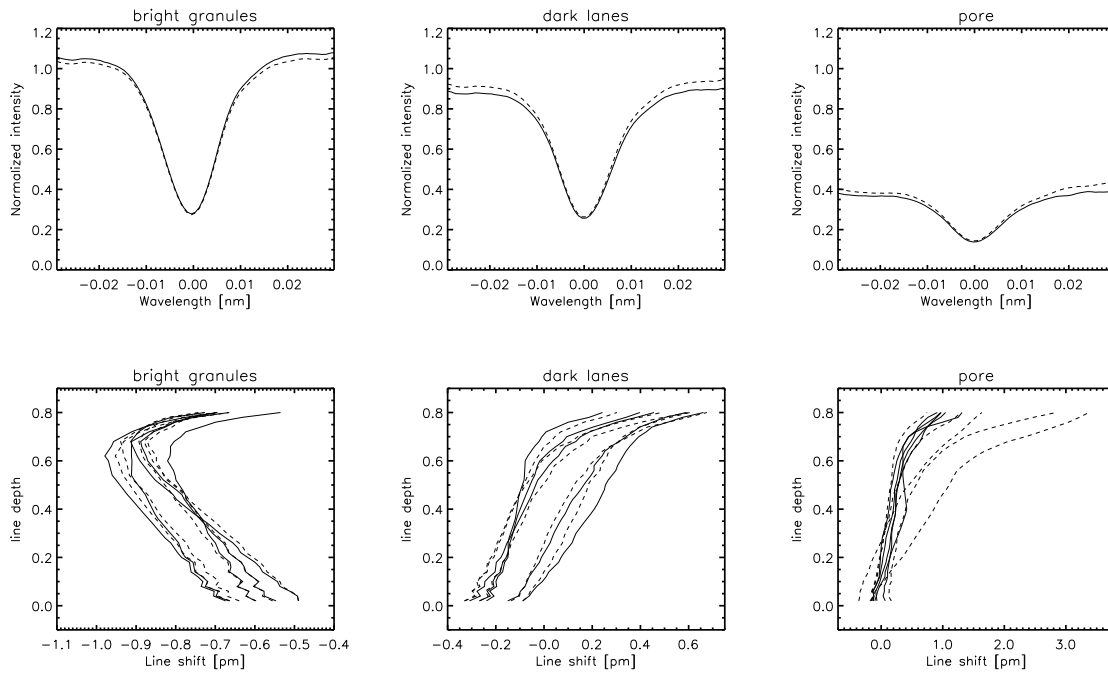


Figure 3.11: Averaged line profiles and bisectors before (dashed) and after (solid) the deconvolution process for selected regions of interest. Top row: spatially and averaged line profiles for the first scan. Bottom row: spatially averaged bisectors for the five scans. Line depths of 0.0 and 1.0 correspond to the line center and the continuum, respectively.

dency as the darkest intergranular lanes before and after the deconvolution: continuum intensities are decreased and the line becomes broader.

However, the mean bisectors for the pore resulting from the second and third scan differ considerably before and after the reconstruction, in particular for bisector levels close to the continuum. Inspecting individual line profiles inside the pore from these two scans reveal the existence of a highly red-shifted line satellite. A possible explanation for this is the presence of a strong downflow inside the pore. However, in the far red wing the line is blended with two molecular lines which might cause or influence the observed asymmetry: MgH at 557.628 nm and C<sub>2</sub> at 557.636 nm. The MgH line only shows up at low temperatures because the molecule has a very low dissociation energy of 1.3 eV. The C<sub>2</sub> line disappears at lower temperatures (high dissociation energy of 6.2 eV) because it comes from an excited state that only gets populated at higher temperatures (priv. comm. Han Uitenbroek). The treatment of this line flag is beyond the scope of this thesis and will be subject of a separate investigation.

The results concerning the photometric quality of the reconstructed spectra and presented above can be summarized as follows:

- Average intensities are preserved and local changes on small spatial scales have the correct sign: bright granules become brighter and dark lanes become darker through the reconstruction.
- Line profiles of bright structures show a decreased line width and those of dark structures have an increased line width.
- Line asymmetries are generally not altered, i. e. the shape of the line bisectors is preserved.

### 3.3.4 Quiet and abnormal granulation

There is an obvious difference between the pattern of the granulation located on the limb side (away from the active region) and that located on the center side (toward the active region) (see e.g. Fig. 3.3, upper row). The latter shows much less contrast and seems to be spatially distorted. This is commonly called “abnormal” granulation [Dunn and Zirker, 1973].

Fig. 3.12 (left) compares the mean line bisectors originating from those two areas (normal: solid, abnormal: dashed). The mean bisector of the abnormal granulation is inclined toward the red, indicating a continuous acceleration toward the surface. The mean bisector of the undisturbed granulation is almost vertical with a slight asymmetry toward the blue showing the expected C-shape [Dravins et al., 1981, Dravins, 1982].

The mean bisectors averaged over the brightest structures in quiet granulation (Fig. 3.12, middle) show the expected blue asymmetry or reversal of the bisector in deep photospheric layers. This blue asymmetry is significantly reduced in the abnormal area throughout the whole height range. The bisector is less inclined and shows a less pronounced reversal. Furthermore, the

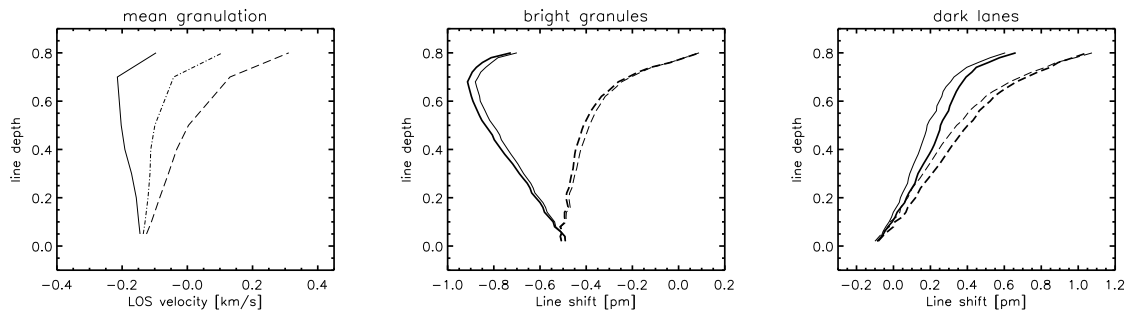


Figure 3.12: Left: Averaged line profiles and bisectors from the un-restored data. Right: Corresponding bisector (dashed-dotted) of the mean granulation (whole FOV). Solid: Quiet Sun granulation. Dashed: Abnormal granulation. Middle and right: Averaged line profiles and bisectors before (thin) and after (thick) the deconvolution process for selected regions of interest. Solid lines: normal granulation. Dashed lines: abnormal granulation. Line depths of 0.0 and 1.0 correspond to the line center and the continuum, respectively.

abnormal intergranular lanes (Fig. 3.12, right) lead on average to more inclined bisectors with a strong red asymmetry compared to the normal intergranular lanes.

Our results are essentially consistent with those from one-dimensional spectroscopic data [e.g. Hanslmeier et al., 1991b]. The advantage of 2-D spectroscopy is the possibility to clearly distinguish between bright granules and intergranular lanes. Our results concerning the bisectors shape in “quiet” and “abnormal” granulation agree with previous findings for active and non-active regions [e.g. Hanslmeier et al., 1991a].



## Chapter 4

# Photospheric bright points

In this thesis, I use the term 'photospheric bright points' (PBPs). These structures - due to the historic reasons and a variety of observational techniques and/or to the region where they occur - are sometimes referred to as filigrees, facular points, network bright points (NBP), magnetic bright points (MBP), continuum bright points, G-band bright points (GBP) and many others (for the more or less complete list see Solanki [1993]). The name refers to the origin of these structures and not to the particular observational technique scale or location on the solar disc, analogically i.e. to 'chromospheric bright points'.

This chapter summarizes the most important observational and theoretical results for photospheric bright points obtained so far.

### 4.1 From filigrees to G-band bright points

In 1968 Stenflo [1968] showed that the flux of each magnetic polarity increased with decreasing slit size when observing solar photosphere. As a conclusion he suggested an existence of several magnetic elements of opposite polarities within one resolution element. If the large slit was used these elements cancelled each other, so the measured field of each polarity was weak, even if the flux in a single magnetic element was significant. On the other hand, this effect was more pronounced when using smaller slit. One year later Livingston and Harvey [1969] provided first observational evidence of the quantization of the photospheric magnetic flux away from sunspots and suggested field strengths of the order of kilogauss. Howard and Stenflo [1972] stated that *the reason that a magnetograph normally records a continuous range of field strengths is (...) that a smaller or larger number of filaments happen to be inside the scanning aperture, and not because of continuous variation of the 'true' field strength.*

All above ideas led to the concept of *two component model* and *magnetic filling factor*. This approach allows to obtain information about unresolved magnetic fields outside of sunspots under an assumption that a resolution element  $A_{res}$  consists of a part with strong (kG) magnetic field  $A_{mag}$  and its field-free surrounding. The magnetic filling factor is then defined as  $\alpha = A_m/A_{res}$ .

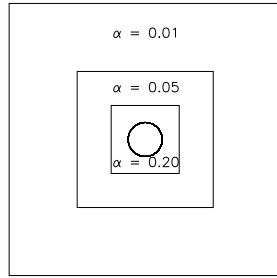


Figure 4.1: Dependence of the filling factor on the size of the resolution element in two-component model. The circle represents a magnetic element and the squares represent resolution elements of different sizes.

Figure 4.1 illustrates the principle of two-component model and dependence of the filling factor on the size of the resolution element.

Both components contribute to the observed intensity  $I$ :

$$I = \alpha I_m + (1 - \alpha) I_{ff},$$

where  $I_m$  is the intensity contribution, expected from a magnetic element that would fill the whole resolution element and  $I_{ff}$  is the intensity contribution expected from a field-free resolution element.

The *line ratio technique* [Howard and Stenflo, 1972, Stenflo, 1973] bases on the *two component model* and enables to determine the field strength of unresolved magnetic field elements. Frazier and Stenflo [1978] used the line ratio technique to demonstrate the field strength in magnetic concentrations is 1-2 kG and their size ranges between 200 and 300 km.

There were attempts to identify these magnetic elements in observations as early as in the 1970s. Dunn and Zirker [1973] noticed strings of bright grains in the intergranular lanes when observing in the red wing of  $H_\alpha$  line. They propose the name *filigree* for this phenomenon and '*crinkle*' for the individual elements because they seem to be zigzagged or crinkled in shape and not just a string of bright dots.

Mehlretter [1974] investigated some examples of photospheric faculae at the center of the solar disc in order to understand their substructure. He observed that *faculae almost invariably consist of either small points which are round (...) or slightly elongated (...), occurring singly or associated in chains, or of ring-like formations or 'crinkles' (...); in some areas - reasonably far from spots - facular structure is almost exclusively made up by 'points' sitting in the intergranular lanes.* The new discovered solar structures were named "facular points" and their sizes were further estimated to be smaller than 350 km [Muller, 1980, Spruit and Zwaan, 1981], in agreement with Frazier and Stenflo [1978] and Mehlretter [1974].

Muller [1983] made observations concerning interaction of facular points with the granular flow in the quiet Sun area. He noticed that they always appear in the dark lanes between the granules and rather at the supergranular boundaries than inside the cells. He also estimated the mean lifetime of bright points as about 1000 s and observed that they often undergo the splitting events. Muller

and Keil [1983] attempted to estimate the real size and brightness of facular points in the “white light” in the quiet photosphere. They obtained the characteristic size of 160 km and the typical brightness of 1.08 relative to the mean surroundings.

To my knowledge, the first observations of bright points in the CH molecular band at 430.5 nm (Fraunhofer G-band) were made in early 1980s. Muller and Roudier [1984] noticed that facular points observed at this wavelength show more contrast than when observing in the “white light”. Using this observational technique Muller and Mena [1987] measured the speed of facular bright points around the decaying sunspot and obtained the mean velocity of 0.65 km/s.

Stenflo and Harvey [1985] used the position of the zero crossing of the Stokes V profile as a measure of the Doppler shift of the line profile inside the magnetic field concentrations. The results show almost no flow inside the magnetic elements, but pointed that there is a downdraft inside the surroundings non-magnetic regions.

Muller et al. [1989] studied the influence of the bright points located in the network (network bright points, NBPs) on the surrounding granulation. They observed a ‘daisy pattern’ known from laboratory convection experiments. Such a pattern is expected when rigid thin obstacle appears among the convective cells. The granules in the presence of the NBPs seem to be smaller than in the undisturbed regions. This is consistent with the results of Dunn and Zirker [1973] for the ‘abnormal’ granulation.

Berger et al. [1995] studied the bright points in the plage and in the network and found, that BPs in the plage are slightly larger and that the majority of them have circular shapes and diameter of 200 km. Their measurements of the bright point contrast in the G-band gave about twice larger values than those in the continuum.

Until the mid 1990s there were no simultaneous high resolution intensity images and magnetograms of PBPs available. The milestone was set by Yi and Engvold [1993] who presented time series of near-simultaneous magnetogram, continuum  $H\alpha$ , and CaII K line images obtained at Swedish Vacuum Telescope (SVST) on La Palma. They showed that PBPs appear always at sites where magnetic concentrations are observed. The main problem in those observations was the low contrast of BPs in the continuum, so only the brightest elements in largest intergranular lanes were taken into consideration, which obviously led to some selection effects. This was significantly improved when the interference filter centered at 430.5 nm, so in the Fraunhofer G-band was added at the SVST. The filter was designed basing on the above-mentioned work of Muller and Roudier [1984]. Using the new filter together with the existing system at SVST [Scharmer, 1989, Title et al., 1989] Berger [1996] verified the conclusions of Yi and Engvold [1993]. He observed that the existence of the magnetic field is indeed necessary, although not sufficient, condition for the occurrence of PBPs, because magnetic elements are often found without associated bright points. They also noticed that filigrees are located in the downflow area.

The analysis of long time series of the plage region obtained with the same observational setup [Berger and Title, 1996] showed that the concept of stable flux tubes of relatively constant shape

is incapable to describe the PBPs (in this study the name G-band Bright Points, GBPs, appears, as far as I know, for the very first time), because of their strongly dynamic interaction with similar structures and granulation, splitting and merging and relatively fast motion along the intergranular lanes (1-5 km/s). They tried to estimate the typical lifetimes of G-band Bright Points, which turned out to be a very difficult task, because of the merging and splitting events. They concluded that *flux that is located within a particular element at a given time will most likely be redistributed to other elements on a timescale of 6 - 8 minutes*. The typical timescale for significant morphological changes was estimated for 100 s. Berger et al. [1998] analyzed a similar dataset, but as they used automated bright point tracking, they achieved better statistical measure of the magnetic element motion. They found a mean magnetic bright point speed of 1.47 km/s and a mean lifetime of 560 s, both results compared well with previous studies. The mean interaction time with the surroundings was estimated for 360 s, which is about the same as the mean granulation lifetime and supports the hypothesis that the local granular flow indeed drives most of the PBPs motions.

Muller et al. [2000] showed that the time of maximum longitudinal field strength does not always coincide with the time of maximum brightness which was in disagreement with existing models of the magnetic concentrations. More about it later.

Berger and Title [2001] analyzed the magnetograms with the maximum spatial resolution of 0.3 arcsec and concluded that *all G-band bright points, properly distinguished from granulation brightenings, are magnetic in nature*. They found that relatively isolated GBPs are not only cospatial, but also comorphous with the associated magnetic concentrations. However, for the bright points occurring in groups the structure seen in the magnetogram seemed to be more diffuse. The average peak flux density of magnetic elements was 135-180 G and the bright G-band structures located at the edges of granules show no magnetic signal. Moreover, they observed that GBPs tend to occur in the surrounding of 'magnetic pathes' demarcated by pores, transient micropores or the abnormal granulation.

Wiehr et al. [2004] used the G-band and continuum observations made at the new 1 m Swedish Solar Telescope to determine the sizes of the photospheric bright points at a high spatial resolution. They found the upper limit of the size distribution close to 300 km and observed a decrease in the number of PBPs having diameter smaller than 130 km. This agrees with theoretical predictions which are described in the next section.

Table 4.1 summarizes the most important observational findings for photospheric bright points.

## 4.2 Understanding photospheric bright points

The magnetic flux tube is one of the fundamental concepts in solar magnetohydrodynamics (MHD). It is used to describe a variety of the solar phenomena: from sunspots to magnetic elements. In the *thin flux tube approximation* [Roberts and Webb, 1978, Ferriz-Mas et al., 1989]

diameter [km]	lifetime [s]	proper motion [km s <sup>-1</sup> ]	LOS velocity	reference
350-1000				Spruit and Zwaan [1981]
150	30-3000 s 1080 (mean)	0.65 (mean)		Muller and Keil [1983] quiet Sun
			no flow	Stenflo and Harvey [1985] plage
350 (mean) 300 (modal)	240-3600 1020 (mean)	0.65 (mean)		Muller and Mena [1987] around a sunspot
		0.35 (mean)	downflows	Yi and Engvold [1993] quiet Sun
250		1.33 (mean) 1.0 (modal) 3.0 (max)		Muller et al. [1994]
120-500		large velocity gradient		von der Lühe [1994] active region
250 (mean) 220 (modal)				Berger et al. [1995] plage and network
250 (mean) 220 (modal)		0.5-5 2.4 (rms)		Berger [1996] disk center plage
		1-5		Berger and Title [1996] around a sunspot
	560 (mean) 4200 (longest)	1.47 (mean) 0.3 (modal)		Berger et al. [1998]
96-118	4200 (longest)	1.47 (mean) 0.3 (modal)		Berger and Title [2001]
			downflows	Langhans et al. [2002] around a pore
100-300				Wiehr et al. [2004] active region

Table 4.1: Overview of the observational results for photospheric bright points. The last column contains references to the results and the location of the observed structures on the Sun.

the cross-sectional scale of the flux tube is small as compared to both, the scale of height of the non-magnetic surroundings and any spatial variation scale along the tube [see e.g. Fan, 2004]. In the zeroth order thin flux tube approximation all physical parameters in the tube (pressure, density, field strength etc.) are assumed to vary only along the tube. Then, flux pressure balance between the flux tube and its unmagnetized surroundings is given by

$$p + \frac{B^2}{8\pi} = p_0, \quad (4.1)$$

where  $p$  is the pressure inside the flux tube,  $B$  is the tube field strength and  $p_0$  is the pressure of non-magnetic surroundings (Fig. 4.2).

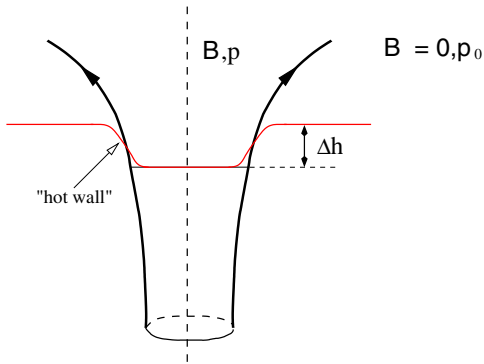


Figure 4.2: Thin flux tube model.

The gas pressure within the tube is reduced with respect to its unmagnetized surroundings by the magnetic pressure  $\frac{B^2}{8\pi}$ . The strong magnetic field prevents convective flow across the field lines and there is only radiative energy exchange between the flux tube and its surroundings present, which quickly establishes thermal equilibrium between the flux tube atmosphere and the ambient medium. Hence, the reduced gas pressure within the tube is achieved by a reduced density, which causes photon escape height being lowered by a Wilson depression  $\Delta h$ . At the circumference of the depression hot exterior material is exposed and radiates into the flux tube. This is known as the *hot wall effect* [Spruit, 1976].

The theory for understanding the formation and evolution of magnetic flux tubes is the *magneto-convection* which describes the interaction between convectively driven flows and a magnetic field. Magnetoconvection processes on the Sun, are associated with [Schüssler, 2001]:

- the generation of magnetic flux by the solar dynamo,
- the structuring of magnetic field flux expulsion,
- magnetohydrodynamic instabilities and magnetoathmospheric waves,
- the transport of mechanical energy.

The mechanism of *flux expulsion* was proposed in the mid-1960s [Parker, 1963, Weiss, 1966]. It is the convectonal flow that expels frozen-in weak fields from convection-cell interiors to the

intergranular lanes and to the boundaries of the supergranular cells. The order of magnitude of the field strength resulting from this process is given by kinetic equipartition,

$$\frac{B}{8\pi} = \frac{\rho}{2}v^2, \quad (4.2)$$

where  $\rho$  is the density and  $v$  the typical granular velocity. Eq. 4.2 expresses the equality of magnetic and kinetic energy density and the resulting field strength  $B = B_{eq}$  is therefore called the *equipartition* field strength. Close to the solar surface it can be estimated to approximately 400 G, which value cannot be significantly exceeded, unless additional effects are taken into account. MHD simulations show [e.g. Galloway and Weiss, 1981, Grossmann-Doerth et al., 1998, Shelyag et al., 2004] that an initially homogeneous vertical magnetic field is advected by the horizontal flow and assembled in the downflow regions of the convection pattern within few minutes. However, magnetic elements harbour kG fields, so that the expulsion mechanism is possibly insufficient to form them. As a consequence of the flux expulsion, the horizontal flow is retarded towards the downflow regions by the growing magnetic fields. This leads to a cooling of the magnetic region, because the radiative losses can not be balanced by the reduced horizontal flow. As the gas pressure decreases, the magnetic field increases and the downflow accelerates, which gives rise to the *superadiabatic effect* [Parker, 1978, Spruit and Zweibel, 1979]: An adiabatic downflow in a thermally isolated magnetic flux tube leads to a cooling of its interior with the respect to the superadiabatically stratified surroundings and it is followed by a partial evacuation of the upper layers. To maintain the pressure equilibrium with the surrounding gas the flux tube contracts and the magnetic pressure increases. This mechanism allows the magnetic field to be locally intensified beyond the equipartition field strength.

When the initial field is stronger, a rebound of the downflow appears followed by an upward traveling shocks [Grossmann-Doerth et al., 1998]. More details concerning the concepts of flux expulsion and intensification can be found in Schüssler [1992].

Steiner et al. [1998] carried out the 2D simulation of magnetic flux sheets embedded in a non stationary, radiative convection. They found a strong dynamic interaction between the magnetic structures and the surroundings, like rapid occasional displacements or inclination of the flux sheet with respect to the vertical direction (see Fig. 4.2. This *swaying motion* can lead to an occasional exposition of a large area of “hot wall” at a favorable angle toward an observer.

During most of the simulation time the flux sheet was formed by strong narrow downflows that are only rarely perturbed by convective motions. These downflows can evolve into *jets*, i.e. they accelerate and become narrower with depth. More details on flux sheet dynamics can be found in a review paper by Steiner [1999].

Bellot Rubio et al. [2001] and Beck et al. [2006] presented spectropolarimetric evidences of a convective collapse and an upward-propagating shocks. Beck et al. [2006] found downflow with velocity of 2 km/s and showed the magnetic field intensification started before a bright point became visible in the G-band.

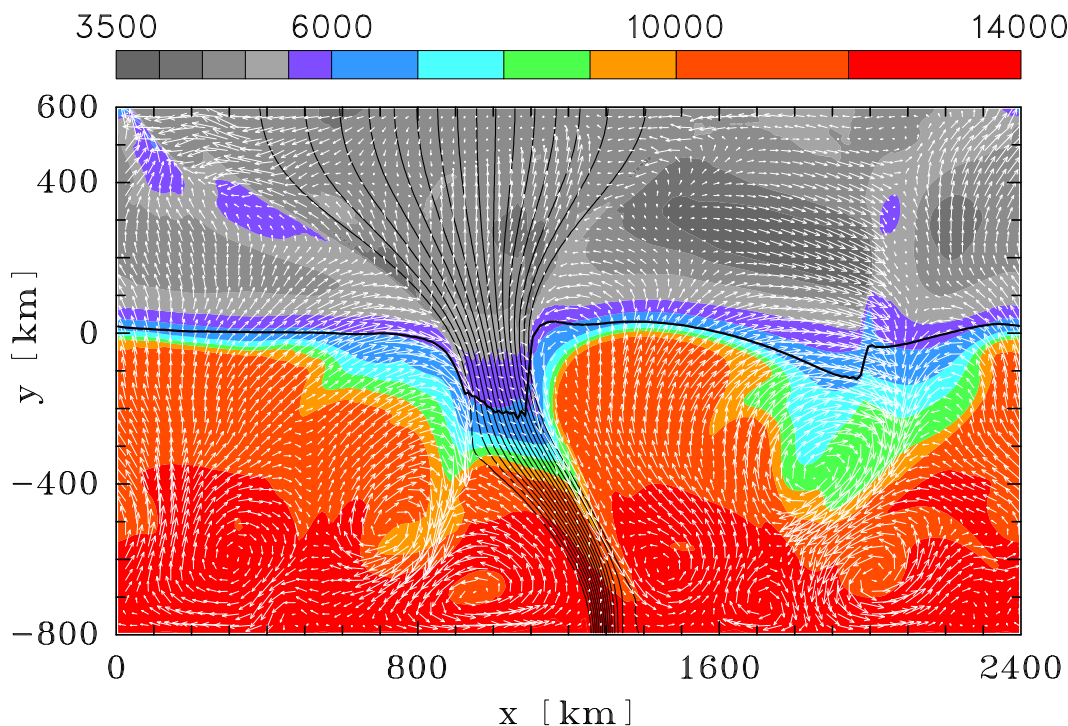


Figure 4.3: Snapshot of a simulation of a magnetic sheet embedded in non stationary convection. Magnetic field lines are shown in black, the velocity field is indicated by white arrows. The temperature is indicated with colors (for a scale in Kelvin see the top bar). The horizontal black line indicates the surface of optical depth unity for vertical lines of sight. Courtesy of O. Steiner.

Similar results were obtained by Shelyag et al. [2004], who carried out 3D simulations of solar magneto-convection including a spectral synthesis in the G-band. The maps of the vertical component of the velocity show that most of the photospheric bright points are associated with downflows, but some show very strong upflows of up to a few km/s.

### 4.3 Why are PBPs bright in the G-band ?

The G-band in the solar spectrum is a molecular bandhead at around 430 nm and it consists of electronic transitions of the molecule CH [Jorgensen et al., 1996]. The name comes from the times when only low resolution spectra were available, when the bandhead appeared like a single spectral line. The name 'G' was assigned to this band by Fraunhofer (1814).

As already mentioned, the photospheric bright points show a high contrast to the photosphere when observed in the G-band. This effect is much smaller in the "white light". There have been several attempts to explain this property of the small magnetic concentration, here I will present only the probably most accepted explanation.

The G-band brightness of magnetic structures depends mainly on the CH line strengths. The

abundance of the molecule CH decreases as the magnetic field strength increases as a consequence of the difference between flux tube atmosphere with respect to the ambient medium.[Shelyag et al., 2004]. This process causes the weakening of the CH lines in the magnetic flux concentration and allows *the continuum to shine through the thinned forest of CH lines across the G-band* [Steiner et al., 2001].

The mechanism behind the G-band brightness of non-magnetic structures is very different: this is caused due to an increase of the local continuum intensity [Langhans et al., 2002]. This is a result of a maximum in the CH number density for the granules caused by the drop of the temperature around the continuum-forming layers [Shelyag et al., 2004].

The observed spectroscopic properties of magnetic and non-magnetic G-band bright structures were investigated by Langhans et al. [2002] who presented the spectra of isolated bright points (see Fig. 4.3) and proposed the classification of those structures based on their spectral signatures in the spectral range from 430.24 to 430.78 nm.

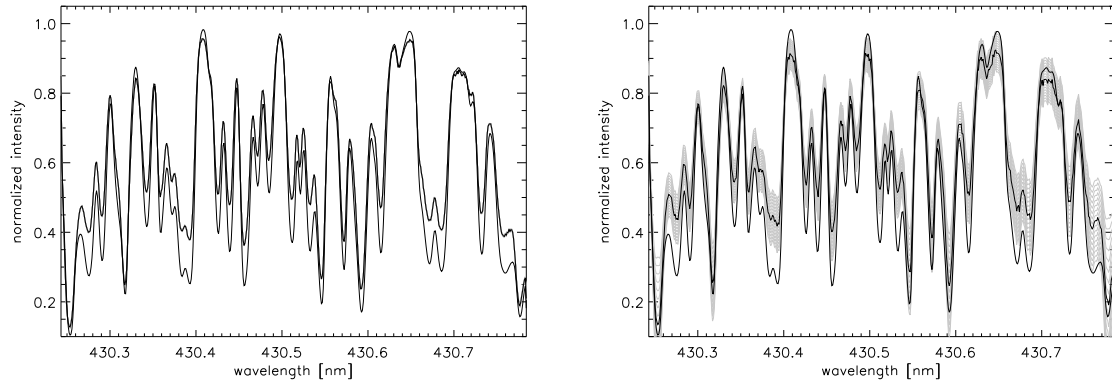


Figure 4.4: Bright point spectra. The thin curve corresponds to an averaged spectrum, obtained in the undisturbed Sun. Left: single bright point spectrum. Right: Averaged spectrum of all observed bright points. The shaded range corresponds to the  $2\sigma$ -level. Courtesy of K. Langhans.

As a classification tool the 'Bright Point Index' (BPI) which is defined as the ratio of the relative line depressions of the Fe II (430.32 nm) and the CH line (430.34nm), minus one, was introduced:

$$BPI = \frac{I_{cont} - I_{lc}^{Fe}}{\langle I_{cont} - I_{lc}^{Fe} \rangle} \cdot \frac{\langle I_{cont} - I_{lc}^{CH} \rangle}{I_{cont} - I_{lc}^{CH}} - 1,$$

where  $I_{cont}$  corresponds to the continuum intensity at 430.33 nm.

The BPI helps to distinguish structures whose brightness is caused by a weakening of the CH line (high BPI) from those with enhanced continuum intensity causing brightness (low BPI). Moreover, structures characterized by a high BPI (= an increased line core intensity of the CH absorption lines) are located in the downflow regions of intergranular lanes and those with low BPI are related to granules and do not show a downflow. This conclusion seem to coincide with

the magnetic/non-magnetic classification introduced by Berger and Title [2001].

## Chapter 5

# Spectroscopy of photospheric bright points

### 5.1 Observations

The observations presented and analyzed in the following sections were taken on November 7th, 2002 at the German Vacuum Tower Telescope on Tenerife, Spain. The data set analyzed here is described in detail in Sec. 3.2.1, the only difference being that the TESOS images are now resized in order to match the image scale of Dalsa.

#### 5.1.1 Velocity maps

A single scan from a tunable 2-D filter instrument provides an observer with a spectral line profile at each pixel of the image. These line profiles can be used to derive the line-of-sight velocity which is one of the most important quantities that can be obtained from a spectroscopic measurement.

As mentioned in Chapter 3, bisectors represent the wavelength shifts of the line at specific intensity levels with respect to a reference wavelength. These wavelength shifts can be interpreted as Doppler shifts:

$$\Delta\lambda_D = \frac{\lambda v}{c}, \quad (5.1)$$

where  $\lambda$  is a reference wavelength,  $c$  is the speed of light and  $v$  is the velocity of the solar plasma generating the line spectral line.

If the source is moving away from the observer the observed wavelength is greater (red-shifted), and if the source is moving toward the observer the observed wavelength is shorter (blue-shifted).

A Doppler shift gives us the line-of-sight component velocity of the plasma. If the source is located at the solar disk center this velocity corresponds to the vertical motion of the plasma. However, if the signal comes from the location away from the disk center the observed line-of-sight velocity contains both the vertical and horizontal velocity component of the moving plasma. The

magnitude of this effect depends on the heliocentric angle  $\theta$ :

$$v_{LOS} = v_{\perp} \cos \theta + v_{\parallel} \sin \theta, \quad (5.2)$$

where  $v_{LOS}$  is the observed line-of-sight velocity, and  $v_{\perp}$  and  $v_{\parallel}$  are the horizontal and vertical velocity components, respectively. If the observed area is located at the disk center the measured LOS velocity correspond to the vertical component of the plasma velocity.

Line-of-sight velocities are derived from the shift of the line profile with respect to a reference position. This could be the laboratory value, but there are several practical reasons which made this solution unpopular:

- the laboratory wavelength is not always known with a sufficient precision
- relative motions between the Sun and an observer, which includes the Earth's rotation and orbital motion and the solar rotation, need to be taken into account
- the velocities have to be corrected for the gravitational red-shift and the convective blue-shift.

In practice, a position of a mean line profile of undisturbed granulation or of a spot/pore is used as a reference. I decided to use a larger pore as a velocity reference, because there is no convective blue-shift in pores or spots. In addition, all the relative motions between the Sun and an observer are automatically taken into account.

The accuracy of the line shift measurement depends on the spectral sampling. Ideally, the sampling should be at least at twice the theoretical spectral resolution of the instrument ("critical sampling"), but the compromise concerning the scan duration has often to be made. The spectral resolution of TESOS at 557.6 nm is 1.74 pm and the data presented in this thesis was sampled with the step of 0.84 pm. The precision of the velocity determination is analyzed in Appendix B.

It has to be mentioned that the seeing changes during a scan can influence the line profile and a resulting line shift measurement. It is due to the changes of the rms contrast of the image, which can result in artificial, *seeing-induced*, shifts of the line position. This effect was described in detail by Schlichenmaier and Schmidt [2000]. Therefore, it is very important to choose the scans recorded under the constant seeing conditions.

As mentioned above, the center of the pore (averaged over all five scans) was used as a velocity reference. I determined the line core position by performing a least-squares second-order polynomial fit to the central part (12 wavelength steps wide) of the line profile. The minimum of the fitted curve was then used as a line core position.

I performed a line bisector analysis at each pixel for the whole FOV for all five scans. 40 bisector positions were calculated at intensity levels between 2 % and 80 % of the line depression. The narrow-band 2-D spectrograms often suffer from a very low SNR ratio, especially in a line core, which can result in very noisy velocity maps. In order to improve that, an average over four

(or more) pixel or over several bisector positions for each single pixel can be used. In this thesis I adopted the latter approach.

Fig. 5.1 shows the line-of-sight velocity maps derived from the first scan and deduced from wavelength shifts in the line wing (bisector positions from 42% and 80% of the line depression, upper row) and the line core (bisector positions from 2% and 40% of the line depression, bottom row), before (left) and after (right) the speckle deconvolution process. Negative velocities (green/blue) point toward the observer and correspond to blue-shifts, while positive ones (yellow/red) correspond to red-shifts.

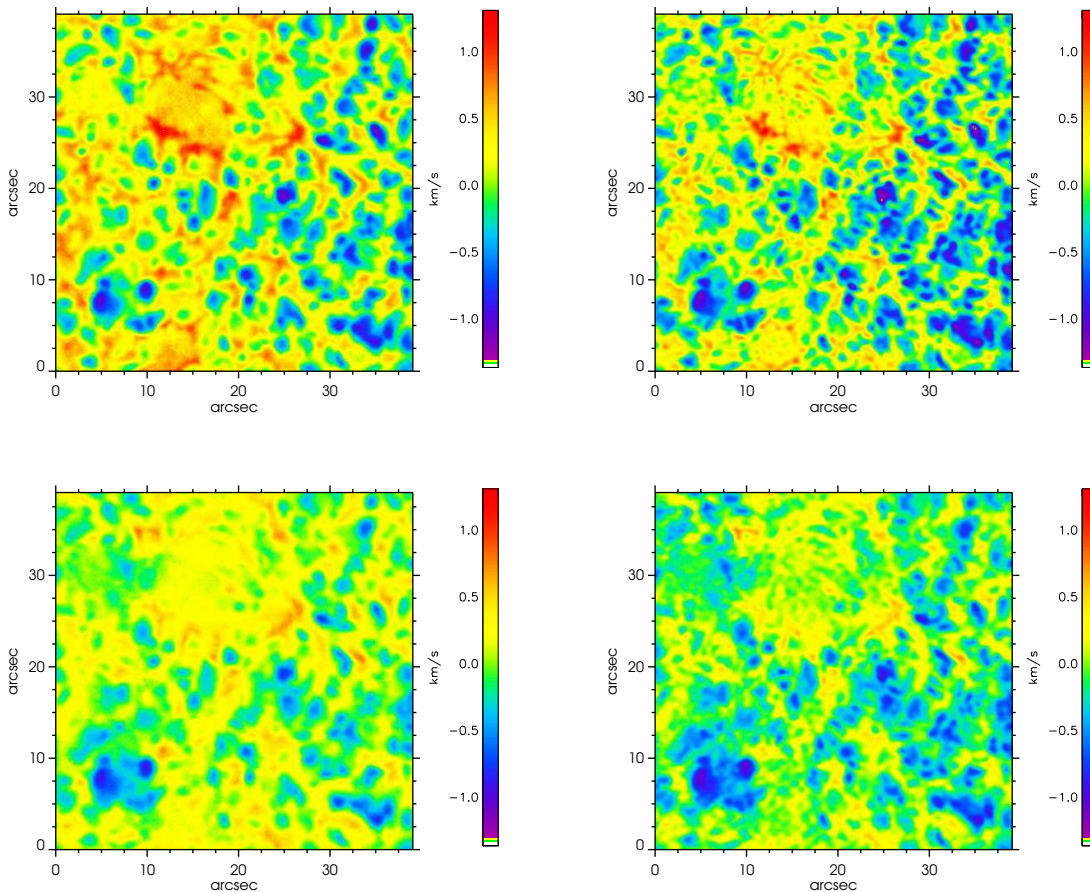


Figure 5.1: Dopplergrams derived from red line wing (top) and the line core (bottom) intensities. Left panel: un-restored data. Right panel: deconvolved data. Yellow/red denotes downflows and green/blue denotes upflows.

It can be clearly seen that the higher contrast and spatial resolution of speckle deconvolved data is transferred to the velocity maps, but the overall velocity structure across the FOV is well preserved.

The Dopplergram derived from the line core has a lower contrast than the velocity map derived from the line wing. In order to understand that the knowledge about the height of formation of spectral lines in the solar atmosphere is needed. The observed quantity - in this case the intensity

at a given wavelength - has contributions from several atmospheric layers. The formation region of the core of the Fe I line at 557.6 nm is located at higher photospheric layers (300-400 km above the level  $\tau_{500nm} = 0$ , see Appendix C and Sec. 5.7), while the wings are formed deeper in the solar photosphere (about 100 km above the level  $\tau_{500nm} = 0$ ). Since the granular flow ceases higher in the solar atmosphere, the velocity maps derived from the line core show less contrast.

The weak *grainy pattern* in the velocity maps calculated from the speckle deconvolved data is most prominent in areas with low signal-to-noise ratio (e.g. inside the pores). A similar effect can be seen in the velocity maps presented for example by Hirzberger and Kneer [2001], calculated from the data restored in a very similar way. More surprisingly, a similar pattern occurs in the Dopplergrams shown by Sütterlin et al. [2001b], obtained from five speckle-reconstructed filtergrams. This suggests that the artefacts in the Doppler maps are not an intrinsic property of the speckle deconvolution, but most probably are an effect of the bandpass noise in certain areas of the image.

Fig. 5.2 shows the line-of-sight velocity maps derived from all five scans and the corresponding G-band images.

## 5.2 Identification of bright points in the G-band images

A very important step of my analysis is to identify the photospheric bright points. This has to be done automatically, because the number of the photospheric bright structures in the given FOV can be as large as few hundreds. The automated detection of the photospheric bright points becomes even more important for long time sequences.

As already mentioned, one of the most favorable spectral regions to detect photospheric bright points is the G-band around 430.5 nm. But a closer look at the data reveals that there are many more small bright structures in the G-band without being photospheric bright points, e.g. bright edges of the granules. Moreover, many G-band bright points show very large contrast locally, but are less bright than the brightest granules. These are the reasons why simple threshold operation is not sufficient to identify the PBPs.

There are several approaches to this problem described in the literature: subtracting the white-light images from the G-band images and then applying the threshold [Nisenson et al., 2003], blob-finding algorithm [Berger et al., 1995], *multiple level tracking* algorithm [Bovelet and Wiehr, 2001] etc.

The method applied by me is a modification of the approach of Berger et al. [1995]. First, the blob-finding algorithm developed by Rosenthal [Tomita, 1990] is applied in order to enhance a contrast of structures of given size and shape. The following quantity is computed at every pixel of the image:

$$B(x, y) = \frac{1}{(2M + 1)^2} \sum_{u=x-M}^{x+M} \sum_{v=y-M}^{y+M} I(u, v) - \frac{1}{(2N + 1)^2} \sum_{u=x-N}^{x+N} \sum_{v=y-N}^{y+N} I(u, v), \quad (5.3)$$

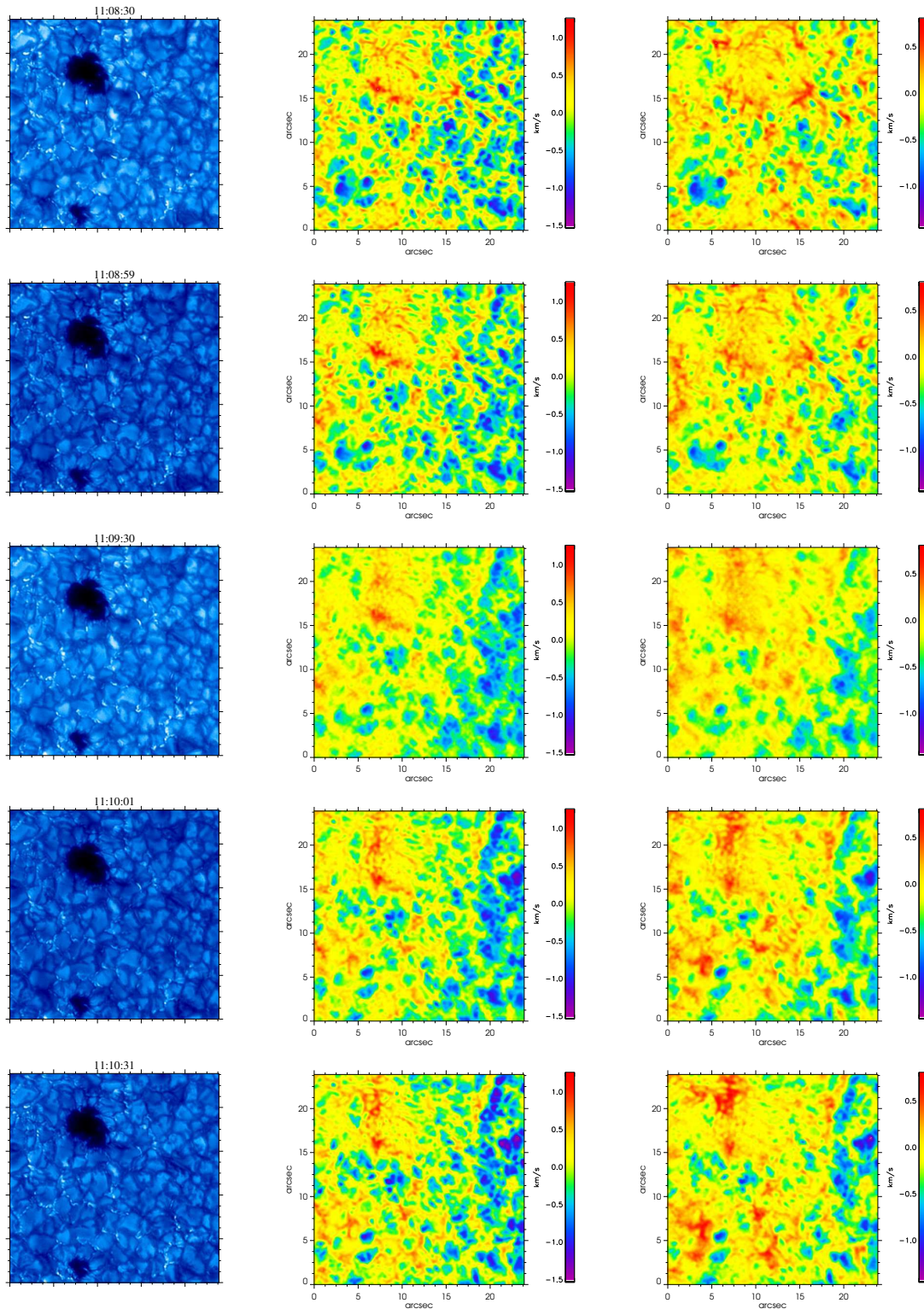


Figure 5.2: G-band intensities and Doppler velocity maps for the five scans. From left to right: G-band intensity, line wing velocity, line core velocity. In the velocity maps yellow/red denotes downflows and green/blue denotes upflows.

where  $M, N$  are integers,  $M < N$  and  $I(x, y)$  is the intensity at the pixel  $(x, y)$ . The operator  $B(x, y)$  returns either positive (bright blobs) or negative values (dark blobs).

In case of the presented data the optimum increase of the contrast for small bright structures was achieved for  $M=2$  and  $N=3$ , which corresponds to  $5 \times 5$  and  $7 \times 7$  pixel, or  $0.28 \times 0.28$  and  $0.39 \times 0.39$  arcsec area, respectively. In the next step, the threshold operation is performed with the threshold value of 15% of the maximum which results in a binary mask. The structures with an area smaller than 7 pixels are then rejected. Further, the 'blobs' are divided into two groups: round and elongated ones. The round ones (as long as they do not exceed a reasonable area) are considered to be single structures, while the elongated ones are then investigated for a presence of an internal gradient. If such a gradient along the structure exists, it is considered to be a 'chain' of individual bright points and divided. As a final step, the surroundings of all potential bright points are investigated in order to distinguish granular brightenings from the bright points located in the intergranular lanes. This procedure leaves us with the binary mask with 1 at the bright points locations and 0 elsewhere.

It is difficult to estimate the detection errors in a case of a photospheric bright point recognition. This is caused by a lack of a very precise definition of a bright point. As already mentioned in Sec. 4.1, the shape of a PBP is round or almost round. I also follow the approach of Langhans et al. [2002] distinguishing between PBPs in the intergranular lanes and bright features confined to granules. When an intergranular lane is very narrow, it is very difficult to distinguish between these two types of G-band bright structures. This is very often the case in abnormal granulation regions.

The final binary mask usually contains some (5-10%) clear false-positive detections which have to be removed manually. For example: in a case of the data presented here, there were some bright structures at the edge of the pore misidentified as bright points, because of their size and high local G-band contrast. The number of false-negative detections is usually smaller and stays below 5%.

I removed large elongated bright structures from the final binary mask, they will be subject of a separated study.

Fig. 5.3 illustrates the process from the G-band image to the final binary mask.

### 5.3 Line-of-sight velocity distribution

The binary masks described in the previous section were used to investigate the distribution of line-of-sight velocities of photospheric bright points. Fig. 5.5 shows the line-of-sight velocities calculated from the line wing plotted versus the line-of-sight velocity calculated from the line core of Fe I line at 557.6 nm. The blue symbols denote velocities of single bright points computed with the center of the pore as a reference. The mean, median and standard deviation of the line core and line wing velocities are listed in Tab. 5.3. One can notice a relatively large scatter of the

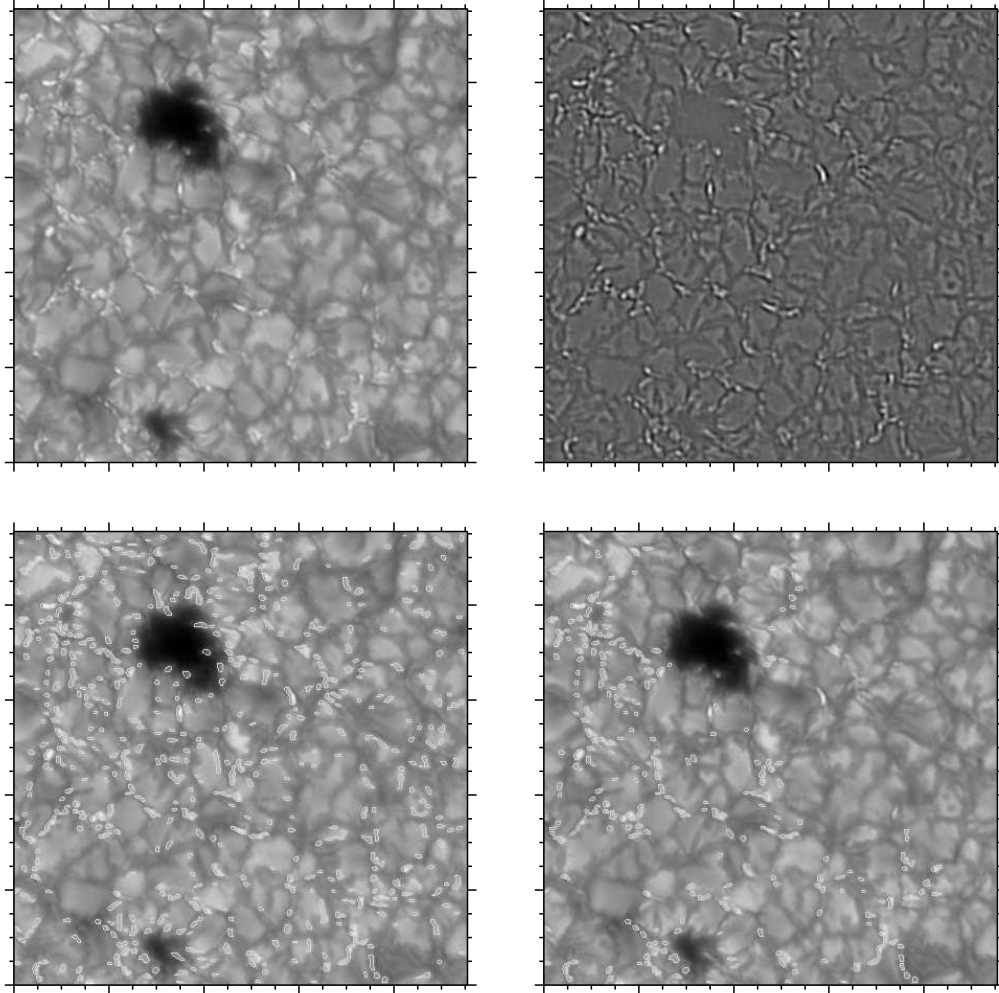


Figure 5.3: Example of photospheric bright points detection process. Upper left: input G-band image. Upper right: blob-enhanced image. Bottom left: combination of the input image and the mask resulting from the threshold operation on the blob-enhanced image and removing small structures. Bottom right: combination of the input image and the final mask, after manual removal of misidentified structures. 233 structures are left after the final visual inspection. One major tick mark corresponds to five arcsec.

No structures	Velocity - line core [km/s]			Velocity - line wing [km/s]		
	Mean	Median	Standard Deviation	Mean	Median	Standard Deviation
233	-0.088	-0.084	0.199	0.127	0.140	0.260
247	-0.065	-0.059	0.175	0.158	0.171	0.227
223	-0.094	-0.087	0.160	0.102	0.117	0.203
243	-0.059	-0.067	0.197	0.116	0.122	0.243
243	-0.058	-0.080	0.185	0.148	0.143	0.228

Table 5.1: Statistics for line-of-sight velocities of photospheric bright points. Rows from top to bottom correspond to the five scans. Velocities were calculated with the center of the pore (mean over all five scans) as a reference.

results, which can be explained by the presence of solar oscillations. The solar photosphere shows periodic motions with periods of about 3-12 min (mostly referred to as "5-min" oscillations), the origin of which has not yet been clearly understood. The typical spatial scales of those oscillations are of order of 10 Mm which corresponds to 10-15 arcsec, the velocity amplitude is typically 0.5 to 1 km/s. Since the characteristic spatial pattern scale of the oscillations is smaller than the investigated area, it can be expected that their contribution to the line-of-sight velocity varies across the field of view.

In order to account for this effect, I used the immediate surroundings of each detected photospheric bright point as a velocity reference. First, I calculated the center of gravity of each structure, then defined an area of  $7 \times 7$  pixels centered at the center of gravity of a given structure. The pixels belonging to the bright structure itself were then subtracted and the remaining pixels were used as a velocity reference. The velocities computed with respect to an immediate surroundings defined above are plotted as blue symbols in Fig. 5.5.

Fig. 5.4 presents the spatial distribution of the photospheric bright points associated with an upflows and downflow. The upflows are denoted with blue and the downflows with red contours.

Table 5.3 presents the statistics for the line-of-sight velocities computed with the immediate surroundings as a reference. One can notice that the line core velocities are very close to zero and similar for all the investigated structures (standard deviation below 50 m/s). This can be understood as a ceasing of the flow in the higher photospheric layers. As far as the line wing velocities are concerned, the mean and median velocity are of order of 200 m/s, which means slight downflow with respect to the immediate surroundings. This is (roughly) in agreement with the results presented in Chapter 4. The largest downflow found in the analyzed dataset is of order of 800 m/s.

The results are presented again in form of histograms in Fig. 5.6 (line core velocities in the right panel and line wing velocities in the left panel). Blue line represents velocities calculated with respect to the pore, and the red line - the velocities calculated with respect to the immediate surroundings.

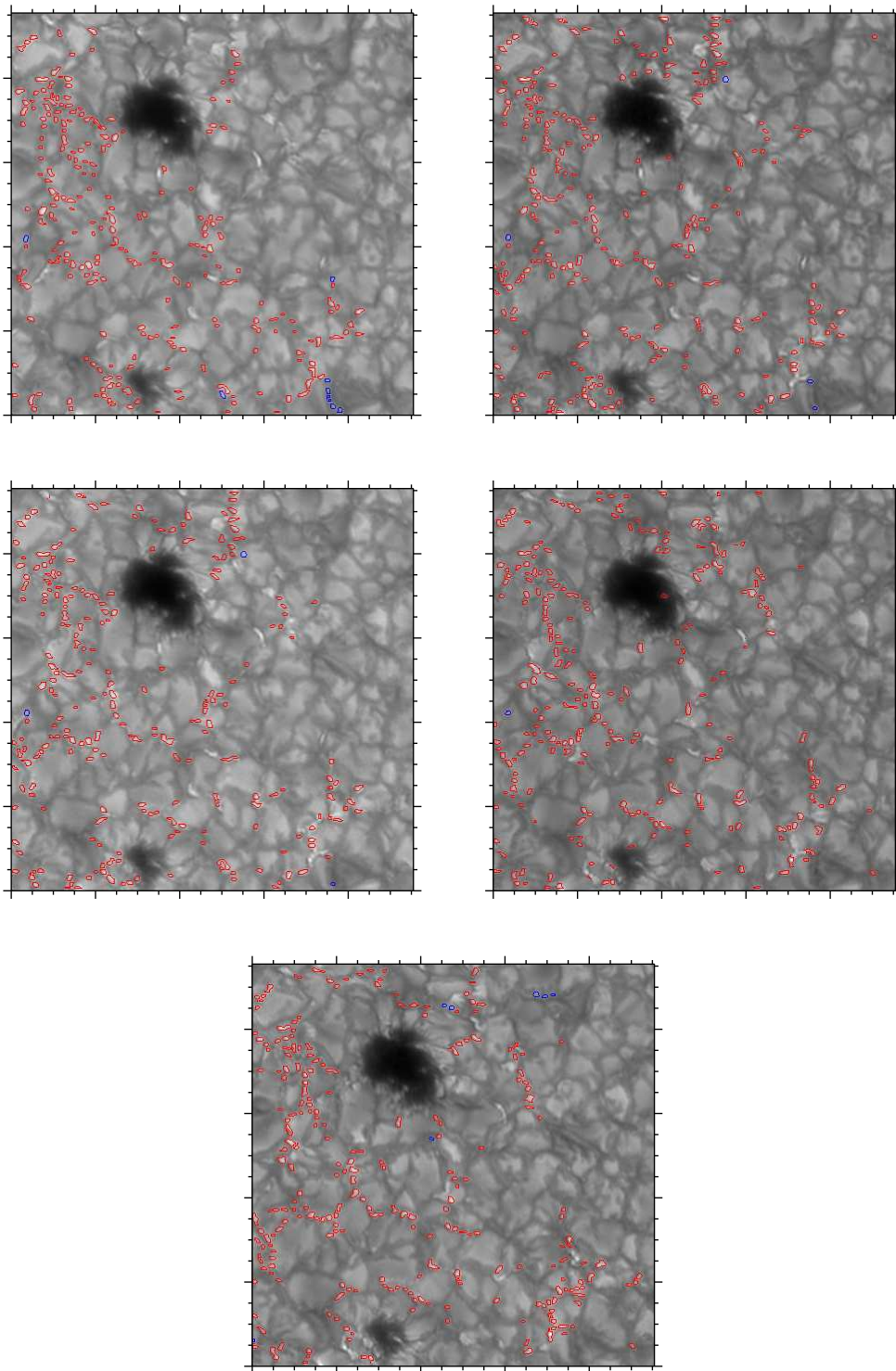


Figure 5.4: The combination of the G-band images, the final “bright points mask” and line-of-sight velocities deduced from the line wing of Fe I line at 557.6 nm for all five scans. Bright points with downflows relative to the immediate surroundings are denoted with red contours, and bright points associated with relative upflows - with blue contours. One major tick mark corresponds to five arcsec.

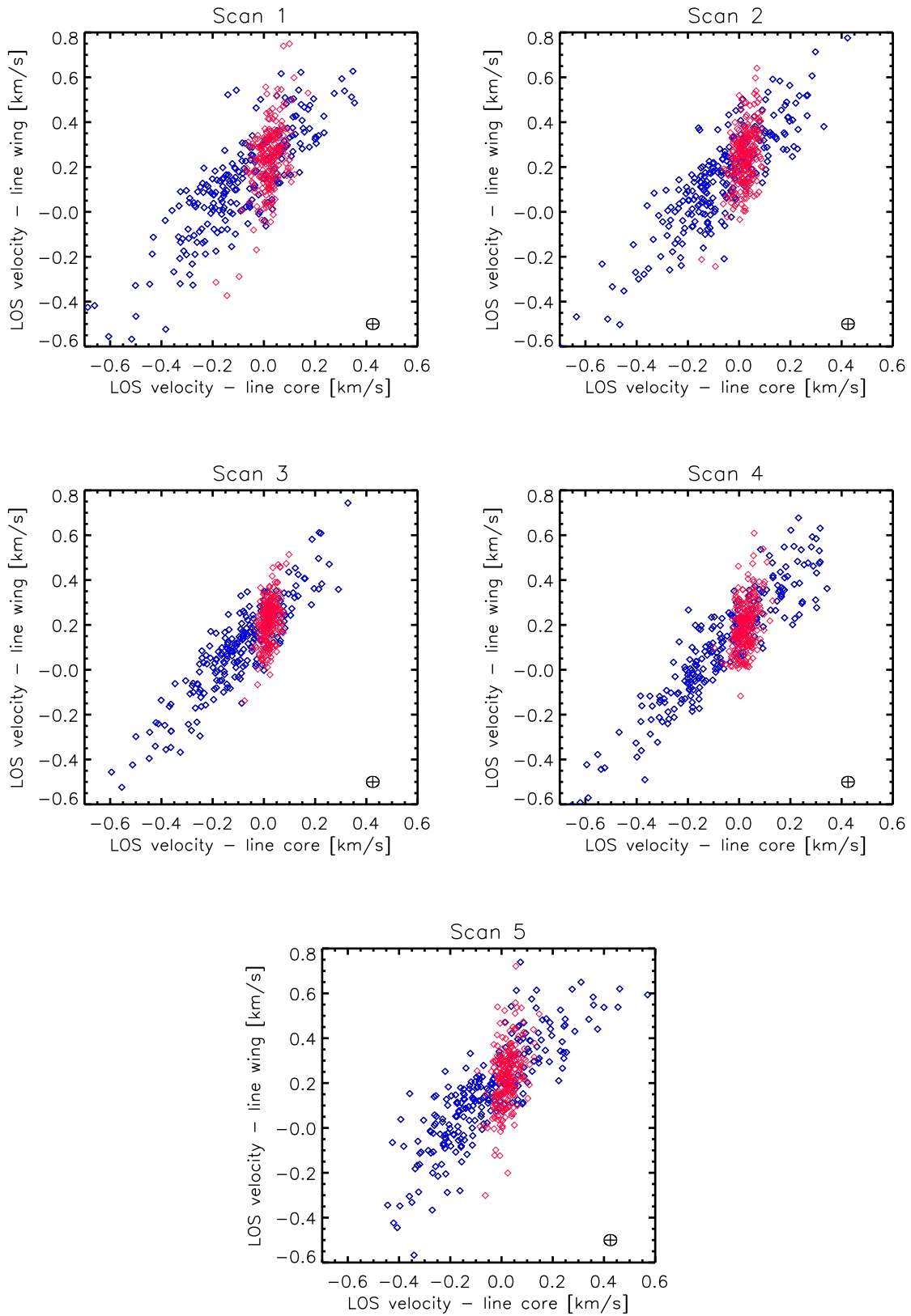


Figure 5.5: Line-of-sight velocities of photospheric bright points from the five scans. Blue symbols: velocities with respect to the center of the pore. Red symbols: velocities with respect to the immediate surroundings ( $7 \times 7$  pixels). The error ellipses indicate the determination precision of the line-of-sight velocity.

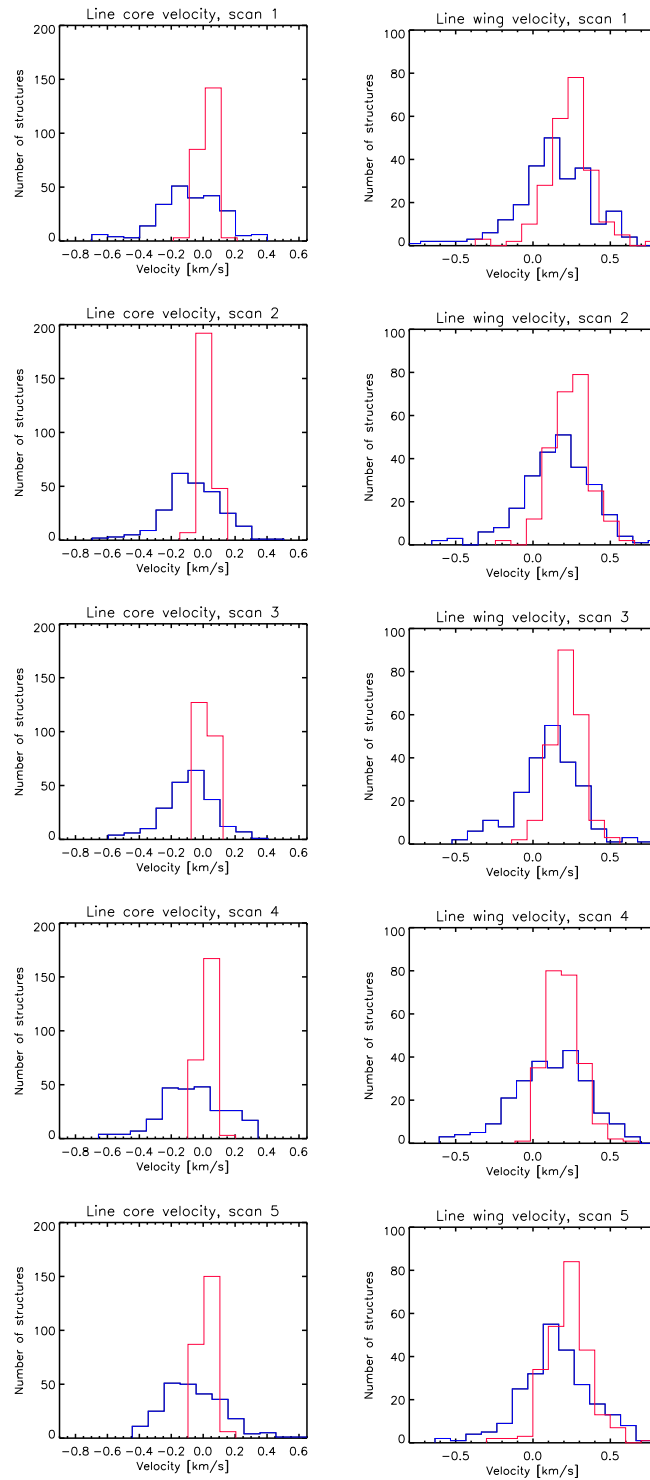


Figure 5.6: Distribution of the line-of-sight velocities of photospheric bright points derived from the line core (left panel) and the line wing (right panel) from the five scans. Blue line: velocities with respect to the center of the pore. Red line: velocities in respect to the immediate surroundings ( $7 \times 7$  pixels).

No structures	Velocity - line core [km/s]			Velocity - line wing [km/s]		
	Mean	Median	Standard Deviation	Mean	Median	Standard Deviation
233	0.021	0.022	0.044	0.236	0.244	0.149
247	0.021	0.022	0.035	0.244	0.248	0.128
223	0.020	0.020	0.026	0.216	0.225	0.100
243	0.023	0.020	0.033	0.198	0.188	0.109
243	0.021	0.019	0.037	0.227	0.231	0.135

Table 5.2: Statistics for line-of-sight velocities of photospheric bright points. Rows from top to bottom correspond to the five scans. Velocities were calculated with their immediate surroundings ( $7 \times 7$  pixels) as a reference.

## 5.4 Are photospheric bright points bright in the line core of Fe I at 557.6 nm ?

As already mentioned, the brightness of the photospheric bright point in the G-band and in the continuum around 550 nm is correlated, although the contrast of PBPs to the mean granulation is higher in the G-band. I investigated the correlation of the brightness of PBPs in the G-band and in the core of the Fe I spectral line at 557.6 nm. As mentioned before, the line core originates higher in the solar photosphere than the continuum and since the granular flow ceases high in the photosphere, no typical granular pattern can be found in the line core image of the investigated spectral line.

Fig. 5.7 shows the “bright point mask” superimposed at the G-band image (left) and the line core image (right). One can notice that the G-band bright points are generally cospatial with the bright areas in the line core image. There are bright area in the left side of the field, where no bright points matching the detection criteria were found, but the granulation in the G-band images at this location seems to be disturbed. On the other hand, there are some G-band bright points locations that are not brighter than the mean in the line core.

Fig. 5.8 demonstrates this effect: in the left panel Fe I line core intensities normalized to the mean are plotted vs normalized G-band intensities at the bright point location. Right panel shows the same quantities, but for the full field of view, one dot corresponds to one pixel. The latter correlation diagram agrees qualitatively with the findings of Berger et al. [1998] who distinguished three components in their correlation diagrams (G-band intensity contrast vs 468.6 nm broad-band intensity contrast): bright points, diffuse component (bright in the G-band) and granulation.

## 5.5 Individual cases

In this section I will analyze the dynamic properties of four individual photospheric bright points. Each of the individual cases is illustrated with a similar figure: in the upper row there are G-band images centered at the analyzed structures, the middle row show cross-sections of the G-band and

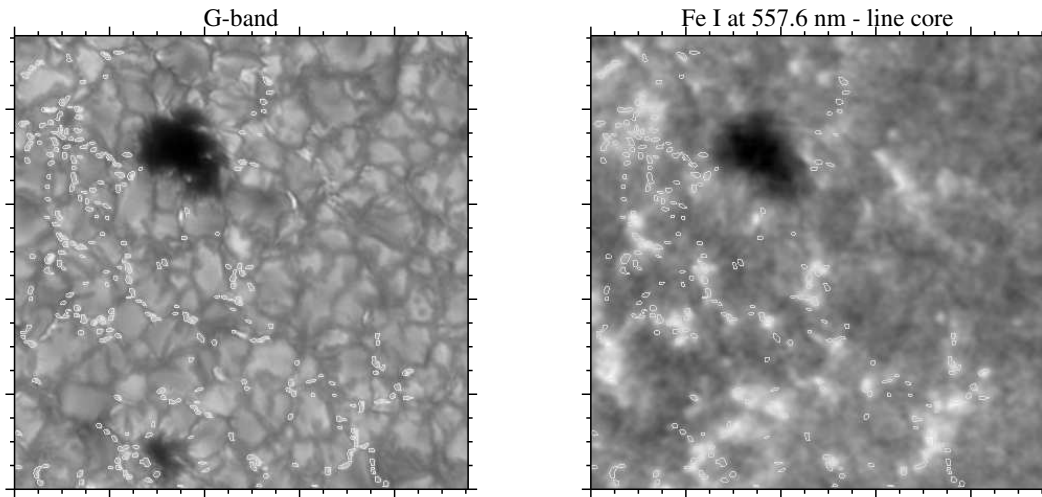


Figure 5.7: Combination of the “bright point mask” and the G-band image (left) and the image at the core of Fe I line at 557.6 nm. One major tick mark corresponds to five arcsec.

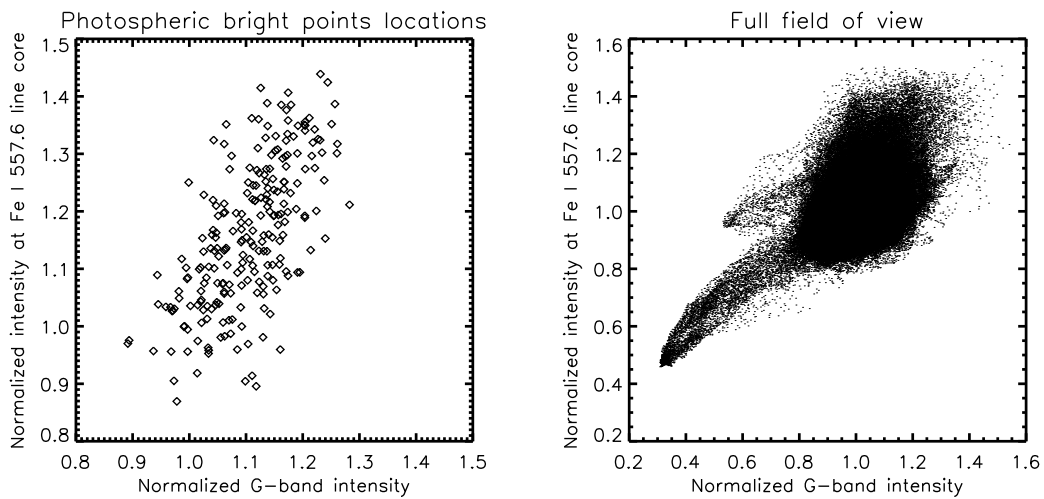


Figure 5.8: Normalized G-band intensities vs normalized intensities in the line core of Fe I line at 557.6 nm. Left: bright points locations. One symbol corresponds to one bright point. Right: full field of view. One symbol corresponds to one pixel. The error of the intensity measurement is about 2%.

the continuum (at 550 nm) intensities and the line-of-sight velocities calculated from the line core and line wing of the Fe I spectral line at 557.6 nm. The velocities were calculated with respect to the center of the pore (mean of all five scans), downflows are positive, upflows are negative.

### 5.5.1 Individual case 1

This is a case of a forming photospheric bright point at the edge of a granule. The G-band contrast of the PBP increases from scan to scan.

The line-of-sight velocities from the line wing from the first two scans show a downflow signature that can be associated with the PBP and vanishes in the third scan. The magnitude of this signature is of order of the precision of the line-of-sight velocity determination (see Appendix B), but since it persists in the two-three scans, it should be taken into account. The line-of-sight velocity from the line core shows a relative downflow for the first and second scan, no relative flow in the third scan and a relative upflow in the fourth and fifth scan. The magnitude of this effect is again rather small, but it could originate from a rebound shock in the higher photospheric layers, described in Chapter 4.

One can notice that the maximum G-band contrast (scan 3) is shifted in time by about 90 s with respect to the moment of the maximum downflow (scan 1).

The bisectors of the photospheric bright point and its immediate surroundings are very similar and resemble those of “abnormal” intergranular lanes (see Chapter 3) and they do not change much in time.

### 5.5.2 Individual case 2

At the first G-band image one can see two rather dim G-band structures in the intergranular lane between two granules. On the consecutive scans the “upper” one vanishes, while the intensity of the other increases continuously. The investigated PBP is associated with a sharp downflow on all the five scans. When looking at the velocity, it is easy to notice the large downflow forming on the left side and finally merging with the downflow associated with the bright point. Interestingly, the slight difference between the line-of-sight velocities between the downflow region and the bright point location persists until the end of the time sequence. Similar to the Case 1 the maximum of the G-band brightness is shifted in time in comparison to the maximum of the relative downflow. The velocities deduced from the line wing and line core show similar temporal behavior.

### 5.5.3 Individual case 3

This is a case of an already existing photospheric bright point with only slight changes in the G-band contrast. This bright point is associated with a downflow, but the line-of-sight velocities do not show any signature that would distinguish this bright point from its intergranular surrounding. During the time sequence, a reduction of the downflow associated with the PBP and

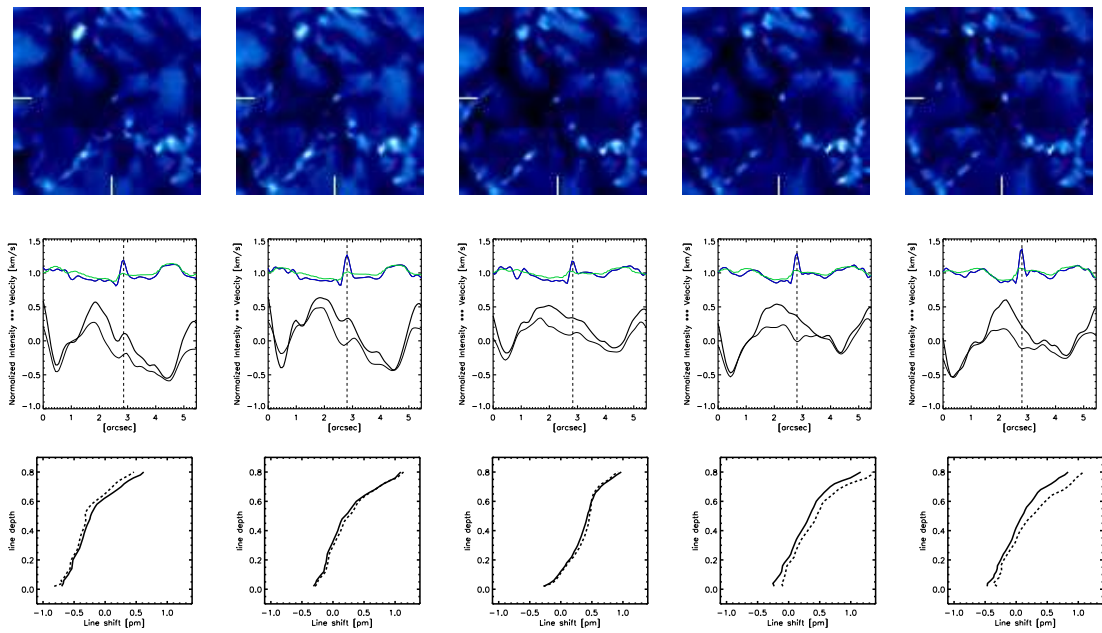


Figure 5.9: Individual case 1. Top row: G-band image, the FOV is  $5.5 \times 5.5$  arcsec and centered at the analyzed structure. Bottom row: Courses of the G-band (blue line) and the continuum (at 550.0 nm, green line) normalized intensities, line core velocity (thin line) and line wing velocity (thick line).

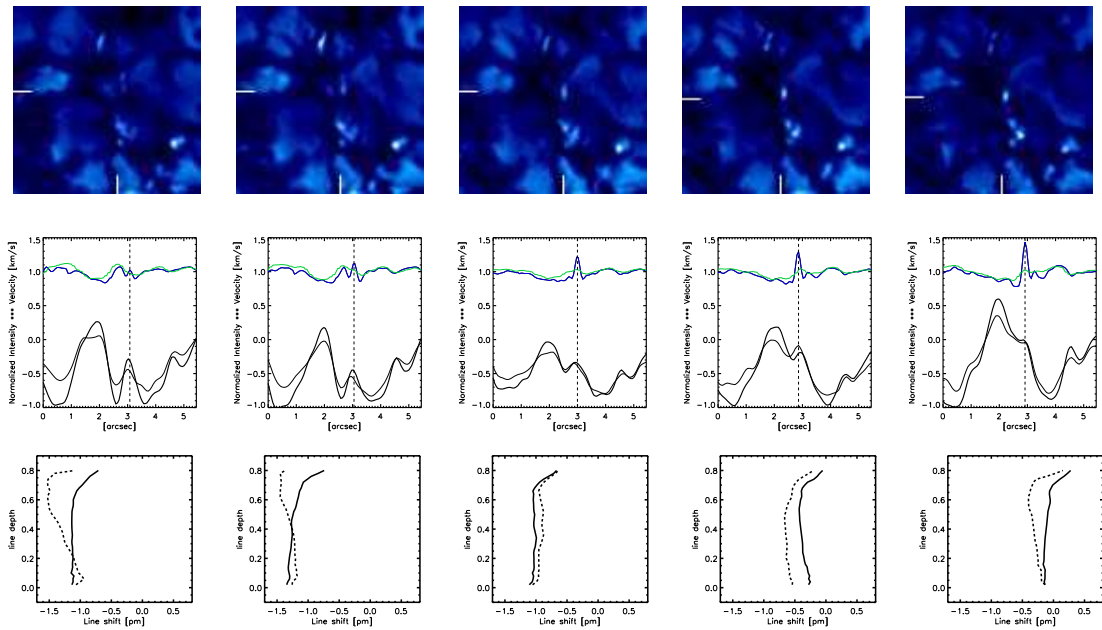


Figure 5.10: Individual case 2. Top row: G-band image, the FOV is  $5.5 \times 5.5$  arcsec and centered at the analyzed structure. Bottom row: Courses of the G-band (blue line) and the continuum (at 550.0 nm, green line) normalized intensities, line core velocity (thin line) and line wing velocity (thick line).

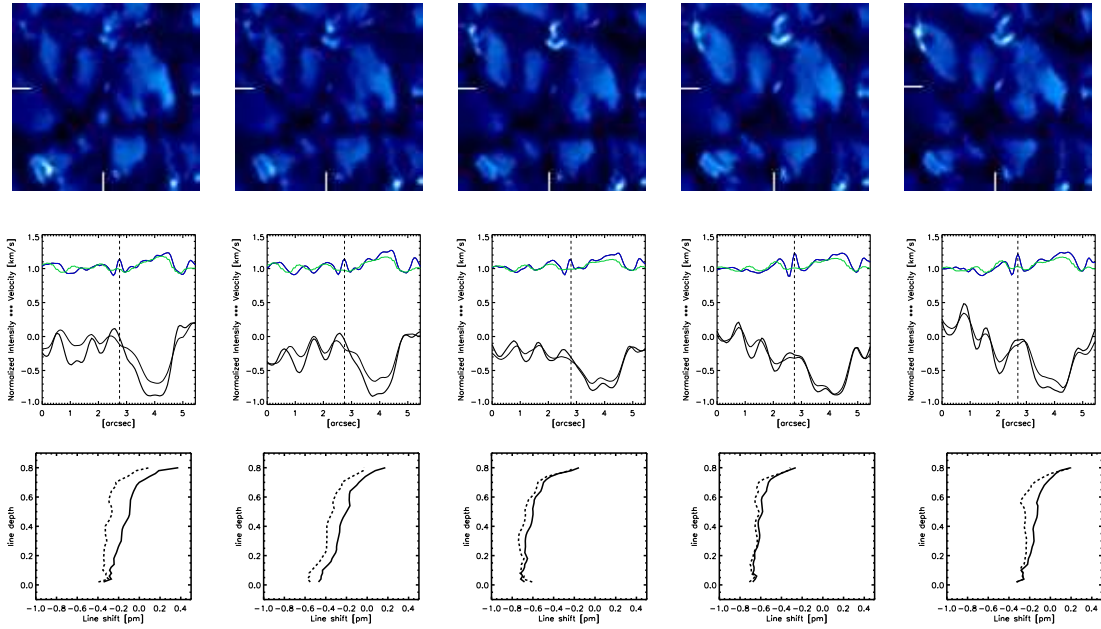


Figure 5.11: Individual case 3. Top row: G-band image, the FOV is  $5.5 \times 5.5$  arcsec and centered at the analyzed structure. Bottom row: Courses of the G-band (blue line) and the continuum (at 550.0 nm, green line) normalized intensities, line core velocity (thin line) and line wing velocity (thick line).

its surroundings can be noticed, but this can be an effect of the granular flow.

The bisector of the bright point and its surroundings are characteristic for “quiet” intergranular lanes and do not show any significant temporal evolution.

#### 5.5.4 Individual case 4

This isolated photospheric bright point is one of a few cases showing a relative upflow, both in the line wing and the line core. It shows a moderate G-band contrast in the first scan, becomes fainter with time and almost vanishes in the fifth scan, so one can assume the case of an “old” PBP.

The upflow is the strongest in the first scan and becomes less significant in the second and third scan, to change into a relative downflow in the fourth scan.

In the first and second scan the bisector of the bright point shows only small variation with the height, in the later scans the relative downflow in the higher layers increases and the relatively large velocity gradient is present. The bisector of the surroundings resembles those of “abnormal” intergranular lanes.

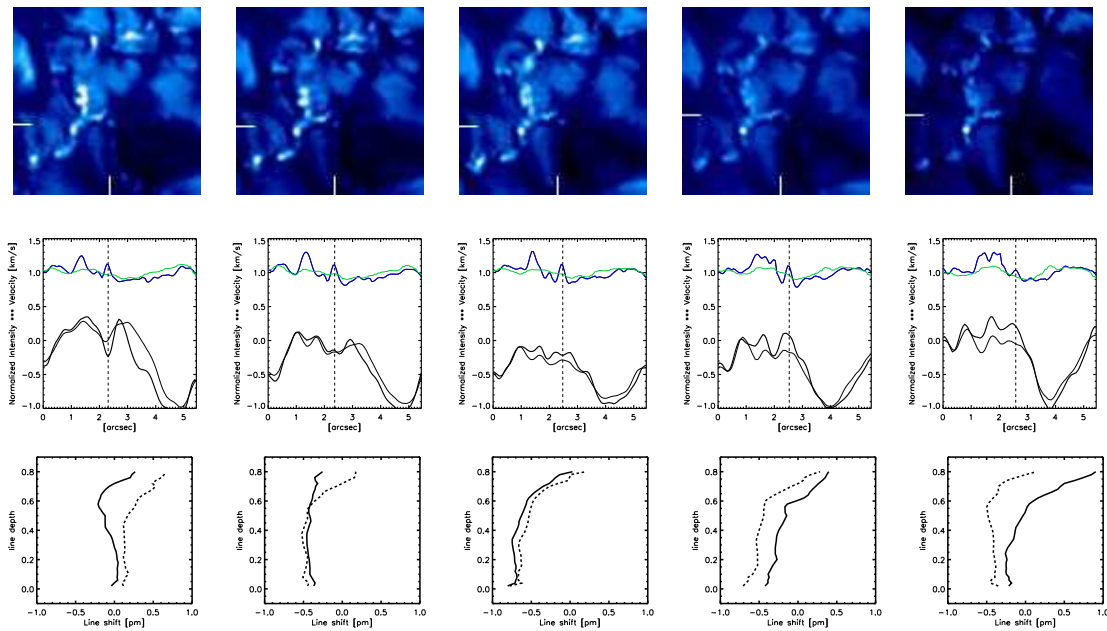


Figure 5.12: Individual case 4. Top row: G-band image, the FOV is  $5.5 \times 5.5$  arcsec and centered at the analyzed structure. Bottom row: Courses of the G-band (blue line) and the continuum (at 550.0 nm, green line) normalized intensities, line core velocity (thin line) and line wing velocity (thick line).

## 5.6 Elongated structures

As previously mentioned, the elongated, large and homogeneous structures were removed from “bright point masks”, because they do not fulfill the common recognition criteria (e.g. shape). I investigated three “loop-like” structures that persisted almost unchanged through all five scans.

First, I calculated the intensity and velocity gradients along the structures’ “spines”, i.e. line segments connecting the most distant points of the structures. The spine was found using the thinning algorithm. The results are shown in Fig. 5.13. The normalized G-band intensity is plotted with a blue line, the intensity at the 550 nm continuum - with a green line. Both the line core (thin line) and the line wing (thick line) intensities are over-plotted. Note, that the sizes of the structures can vary from scan to scan.

All three structures seem to be internally quite homogeneous, as far the intensity and the velocity is concerned. Their temporal evolution is slower when comparing to the PBPs and they are more resistant versus the granular motion. Only the structure presented in the right column of Fig. 5.14 shows some signs of splitting in the last scan. The elongated objects are inconspicuous in velocity (see middle and bottom row of Fig. 5.14)

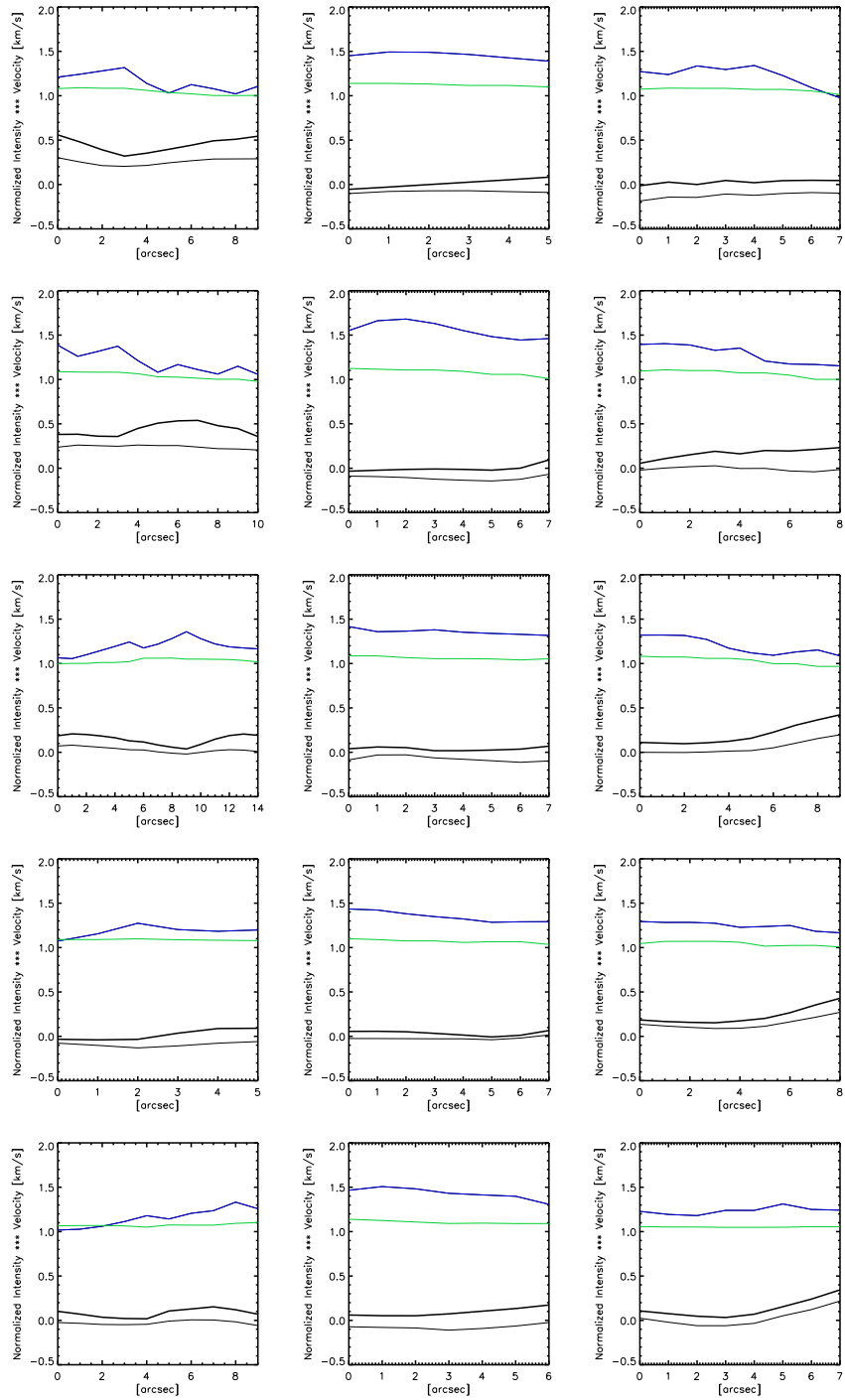


Figure 5.13: From left to right: three examples of elongated G-band bright structures. From top to bottom: intensities and velocities for all five scans. Courses of the G-band (blue line) and the continuum (at 550.0 nm, green line) normalized intensities, line core velocity (thin line) and line wing velocity (thick line)

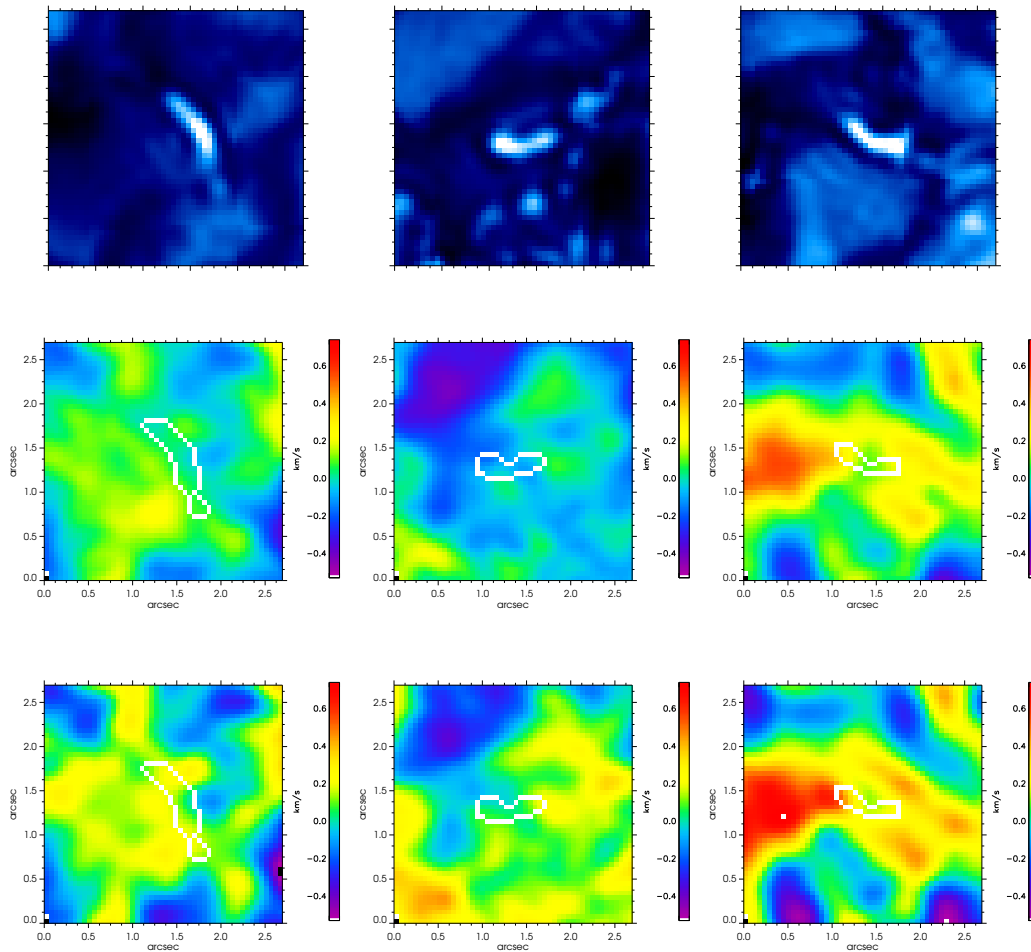


Figure 5.14: From left to right: three examples of elongated G-band bright structures. Top row: G-band image, the FOV is  $5.5 \times 5.5$  arcsec and centered at the analyzed structure. Middle row: Line-of-sight velocity deduced from the line core. Bottom row: line-of-sight velocity from the line wing.

## 5.7 Velocities and height of formation of spectral lines

As already mentioned in Chapter 4, the physical conditions are different within a flux tube and its surrounding which causes the Wilson depression. As a consequence, the observed spectral lines are formed at the different geometrical heights inside and outside a flux tube.

Fig. 5.15 shows the temperature structure inside (solid line) and outside (dashed line) a magnetic element plotted versus the optical depth (left, see C) and the geometrical height (right). The interior of a magnetic element is represented here by network flux tube model atmosphere of Solanki and Brigrjevic [1992]. The geometrical height corresponds to an atmosphere that surrounds the flux tube where  $\tau(z = 0) = 1$ . One can easily see, that the flux tube atmosphere is “shifted downwards” with respect to the non magnetic surrounding, so that the pressure equilibrium is

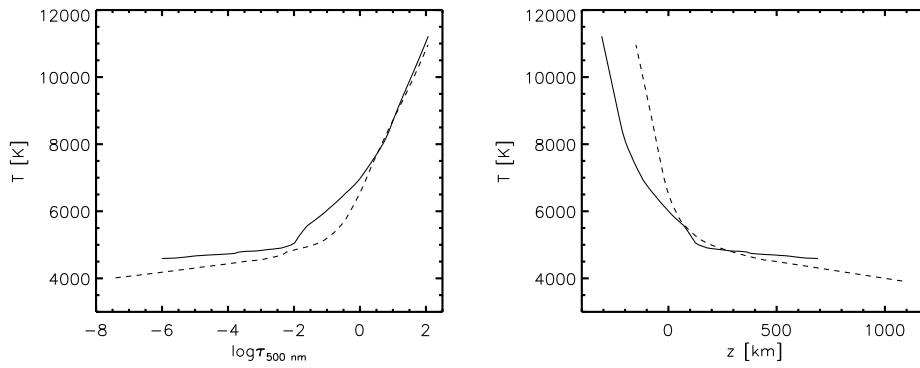


Figure 5.15: Model temperature inside (solid line) and outside (dashed line) a magnetic element versus the optical depth and the geometrical height (right). For the models description see text. Courtesy of O. Steiner.

maintained when taking the magnetic pressure into account. In this case, the “Wilson depression” is of about 100 km.

The non magnetic surrounding is represented by solar atmosphere model F (average supergranule cell interior) of Fontenla et al. [1999].

The determination of the line-forming layers can be carried out with the use of contribution functions, which give the contribution of the different atmospheric layers to an observed quantity. For this analysis the *contribution function to the line depression* (see e.g. Magain [1986] or Gurtovenko et al. [1991]) for the Fe I line at 5576 nm (calculated for the local thermodynamic equilibrium (LTE) conditions) was used.

Upper panel of Fig. 5.16 shows the formation depths of the analyzed Fe I inside (solid line) and outside (dashed line) a magnetic flux tube plotted versus the spectral distance from the line core ( $\lambda = 0$ ). One can see, that in the continuum the difference in the formation depth about 100 km and increases to 200 km in the line core. Lower panel of Fig. 5.16 presents the same data, but plotted versus the *relative line depression* (0 corresponds to the continuum and 1 to the line core).

The effect of the “Wilson depression” demonstrated above has practical consequences for the analysis of the line-of-sight velocities of photospheric bright points and their surrounding. Because of different physical conditions inside and outside of these structures a direct comparison of the velocities may be difficult.

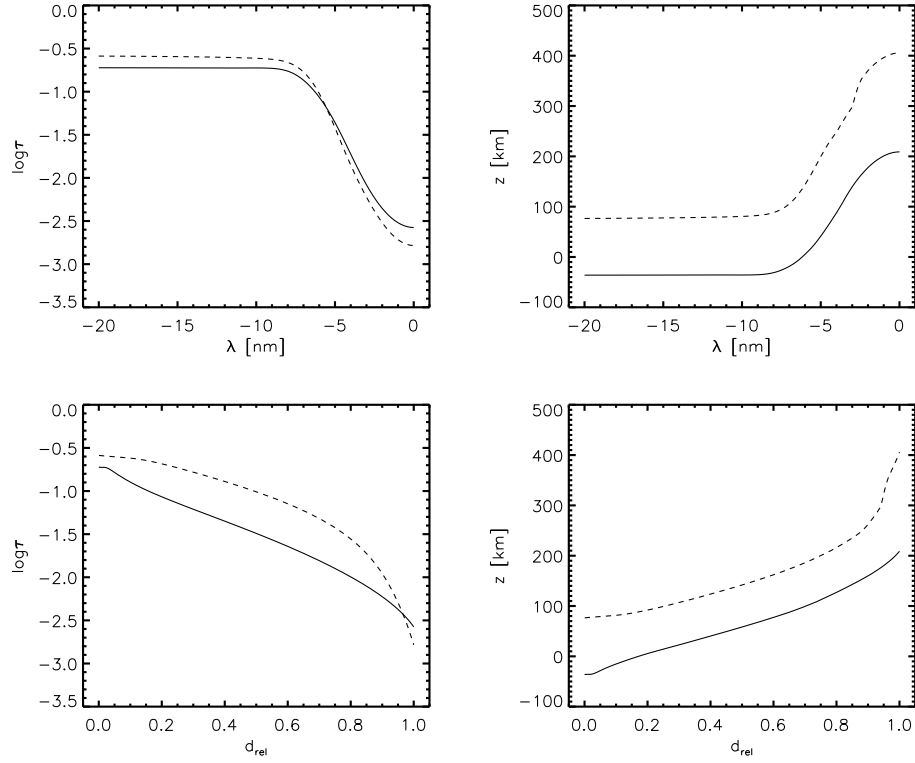


Figure 5.16: Formation height of Fe I spectral line at 557.6 nm inside (solid line) and outside (dashed line) a magnetic flux tube versus the spectral distance from the line core (upper panel  $\lambda = 0$  corresponds to the line core) and the relative line depression (lower panel, 0 corresponds to the continuum and 1 to the line core). Courtesy of O. Steiner.



# Chapter 6

## Conclusions and outlook

In this chapter I summarize the results discussed in the previous chapters. The summary is followed by the conclusions and discussion of possible extensions of this work.

### Summary

**Chapter 2:** KISIP V - a user-friendly version of the implementation of the extended Knox-Thompson speckle reconstruction algorithm developed at KIS - is now available. The package has been tested using simulated and real data. Simulated data permit to compare a speckle reconstruction with input data, estimate photometric errors of the speckle reconstruction process and understand which set of input parameters is required for given atmospheric conditions and a solar scene.

The application of KISIP V to observational data was mostly successful and the range of atmospheric conditions which can be successfully treated by speckle imaging turned out to be very large. Even data with a Fried parameter of order of a few cm could provide a decent reconstruction. We generally use KISIP V with observations taken with adaptive optics. Our experience proves it to be a well working combination. First, speckle imaging is sensitive to slowly varying low order aberrations of the optical system, especially at good seeing conditions and the adaptive optics effectively removes most of this kind of quasi-static aberrations efficiently. Second, adaptive optics compensate low orders of dynamic aberrations, while higher orders are partially or fully uncompensated. Therefore, the Speckle Transfer Function for an uncompensated wave with better seeing can be used as a first order approximation of the Speckle Transfer Function for a partially compensated wavefront.

**Chapter 3:** Speckle deconvolution techniques are already established in the solar physics community. Our implementation of the method proposed by Keller and von der Lühe [1992] was tested on high resolution two-dimensional spectroscopic data from in order to test its influence on the spectral line profiles. The analysis, including the measurement of line position and depth,

as well as the line asymmetry, revealed that the line profiles were changed by the reconstruction in the expected way for increasing spatial resolution. In particular, local changes of intensity on small spatial scales have the correct sign, line profiles of bright structures show a decreased line width and those of dark ones have an increased line width and line asymmetries are preserved. The findings presented in this thesis prove that speckle-reconstructed spectral line profiles can be used for quantitative spectroscopy.

One of the advantages of 2-D spectroscopy is the possibility to clearly distinguish between different photospheric structures. The investigations of the line shifts and asymmetries of quiet and “abnormal” granulation confirm the previous findings from 1-D spectroscopy: there is indeed a significant difference between the line asymmetry in quiet and disturbed granulation.

**Chapter 5:** Two-dimensional spectroscopic data from TESOS and G-band filtergrams were used to investigate line-of-sight velocities of photospheric bright points. First, photospheric bright points, properly distinguished from granular brightenings, are localized on a G-band images. Then line-of-sight velocities derived from the line wing and the line core of Fe I spectral line at 557.6 nm are calculated for every PBP. The scatter in the LOS velocities calculated with a center of the pore as a velocity reference is most probably due to the presence of solar oscillations. This is the reason why the local velocity references are better when comparing the structures from different areas of the field of view. Most photospheric bright points show downflows with respect to their immediate surroundings in the lower photospheric layers which agrees with the previous findings. However, although the high contrast of the photospheric bright points persists in the higher photospheric layers (the line core filtergrams), the flow seems to cease there.

In many cases, the high spatial resolution of spectral data presented here allows to follow the changes in the line-of-sight velocity of the bright points and their immediate surroundings. Four significant single cases of photospheric bright points were presented in order to demonstrate the variety of dynamic properties of those structures.

The elongated G-band bright structures do not fulfill the detection criteria for the PBPs are therefore were investigated separately. They are quite homogeneous as far as line-of-sight velocities are concerned and very stable against the granular flow. A detailed study with more objects is needed to understand if they are unresolved “chains” of photospheric bright points, loop-like structures or effects of swaying motion of magnetic flux tubes (see Chapter 4).

## Conclusions

The solar data used in this thesis was improved in both active (adaptive optics) or passive (speckle reconstruction techniques) way. It was proved that the speckle-deconvolved spectral profiles from TESOS do not show artefacts compromising their usage for a quantitative analysis.

The speckle reconstructed profiles of Fe I spectral line at 557.6 nm were used to investigate the line-of-sight velocities of photospheric bright points. The majority of the photospheric bright

points are associated with downflows, which is in agreement with MHD simulations [Steiner et al., 1998, Grossmann-Doerth et al., 1998, Shelyag et al., 2004], as well as the fact that larger velocities were found in the line wing (lower photospheric layers) than in the line core (higher photospheric layers). Hence, this result is an indication for a convective collapse (see Chapter 4).

There were only very few photospheric bright points in the analyzed data which showed upflows with respect to their immediate surroundings. This effect was predicted by MHD simulation carried by Grossmann-Doerth et al. [1998].

However, the magnitude of the line-of-sight velocities presented in this thesis is smaller than predicted by the above-mentioned MHD simulations (up to few km/s). This can be due to a different spatial resolution of the models and the data presented here.

The analysis of single photospheric bright points shows that the maximum downflow usually does not coincide with the maximum G-band intensity [see Beck et al., 2006]. The maximum downflow is characteristic for the initial phase of a photospheric bright point existence. The dynamic interaction of photospheric bright points with the granular flow known from the analysis of G-band images sequences [see e.g. Berger et al., 1995] can be also observed in Dopplergrams, e.g. as merging of two downflow regions.

The analysis of the line core images revealed that there are bright areas at photospheric bright points locations. This can be an indication that these structures persist with height in the solar atmosphere and a justification of the efforts to understand whether chromospheric and photospheric bright points are manifestations of the same solar structures.

## Outlook

The results presented in this thesis give some new insights into the dynamics of photospheric bright points. During our next observational campaign efforts will be made to perform simultaneous measurements of line-of-sight velocities and magnetic fields of photospheric bright points with TESOS and TIP (Tenerife Infrared Polarimeter) at the VTT. A longer time series would allow to filter the solar oscillations and therefore get more precise velocity estimation.

The spatial scales relevant to magnetic elements still cannot be fully resolved, because they are below the diffraction limit of currently operating solar telescopes. This situation will improve quite soon, when the new 1.5 m solar telescope GREGOR at the Teide Observatory on Tenerife becomes operational. Another perspective is offered by currently developed MCAO systems [see e.g. von der Lühe et al., in press] which will be able to compensate larger fields of view than conventional adaptive optics systems.



# Appendix A

## Spectroscopic observations

### A.1 TESOS - TElecentric SOLar Spectrometer

TESOS operates at the VTT since 1997. It consists of the three Fabry-Perot interferometers, in a telecentric mount.

This optical configuration allows for a very compact design and provides a constant wavelength passband across the whole field of view. The instrument has very good wavelength stability with time. A sequence of four wavelength regions can be recorded sequentially, and the time to switch from one filter to another is only one second. TESOS is equipped with two PIXEL VISION backside-illuminated CCDs which are capable to detect enough photons also from the short-wavelength part of the visible spectra.

The optical scheme of TESOS is presented in Fig. A.1 and the instrument characteristics are listed in Table A.1.

### A.2 Intensity modulation

Some of the line profiles, when observed with TESOS, exhibit an *intensity modulation* which has been described by Tritschler et al. [2002]. The 557.6 nm line shows an intensity variation of about a few percent due to this effect. The period and amplitude of this intensity variation pattern remains constant in space and time for a given spectral region. The magnitude of this effect is wavelength dependent and its amplitude varies from about ten percent to virtually zero.

The reasons for this modulation pattern are still quite unclear. It might be caused by an unwanted influence from one of the plates of the FPIs.

I have concluded that there are two ways to deal with this problem:

1. by comparing the observed line with a theoretical line profile from the quiet Sun model in order to determine the modulation pattern,

Spectral range	430-750 nm
Field of view	50/100 arcsec
Spectral resolution	320.000/160.000
Spatial scale	0.09/0.19 arcsec/pixel
Scan range	1 nm
Step width	> 0.25 pm
Stability	< 0.30 pm/h
Frame rate	3-5 frames/s
Prefilters	FWHM 1.0 nm (four filters in one setup)
Prefilter adjustment range	+0/-0.2 nm
Detectors	2 PV PLUTO 652 × 488, backside illum.
Pixel size	12 $\mu\text{m}$
Digital Resolution	14 bit
FPIS	3 Queensgate ET50-FS

Table A.1: TESOS: Instrument characteristics. Courtesy of W.Schmidt.

2. by removing the frequencies originating from modulation using a Fourier filter with the observed line profile.

The first method is not really useful, since theoretical profiles are always symmetric and the line profiles originating from the solar structures almost always show asymmetries. Therefore, I applied the second method to the data presented in this thesis. The single sinusoid fit seems not to result in a good correction - the modulation pattern is still prominent. Only removing more frequencies seems to guarantee a good result.

Fig. A.2 shows the spectral line profile (Fe I 557.6 nm) with the *intensity modulation* effect (thin line) and the line profile with modulation corrected by removing the most prominent Fourier frequencies (thick line).

The Fourier method is relatively fast and does not rely on the theoretical models, but it requires observations of the nearby continuum. This can be done just once during the observational campaign, since the modulation does not change with the time. Using this method can be rather difficult in case of the spectral lines without nearby continuum.

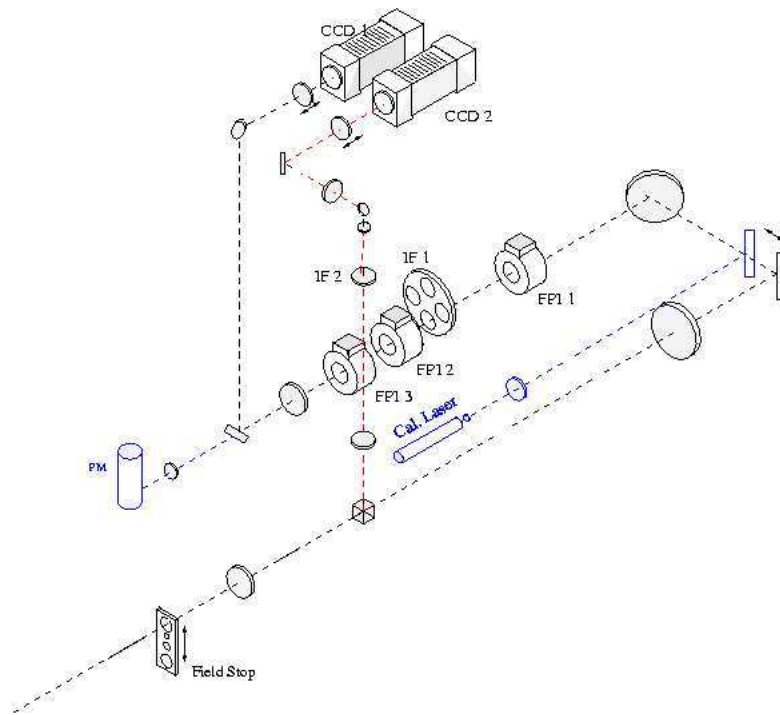


Figure A.1: TESOS optical scheme. Courtesy of T. Kentischer.

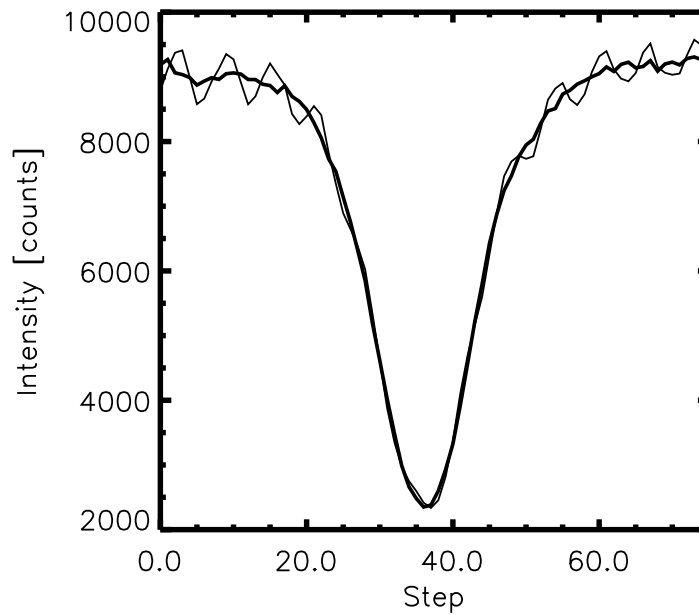


Figure A.2: Intensity modulation effect in the spectral line Fe I 557.6 nm: an uncorrected profile (thin line) and a profile corrected by removing several frequencies (thick line).



# Appendix B

## Precision of velocity measurements

Error estimation is a very important step in each data analysis. In a context of this thesis the precision of the line-of-sight velocity determination deserves a particular attention.

The actual measurement done with TESOS is the intensity, which is followed by the line shift estimation. It can be then translated to the line-of-sight velocity using the Doppler formula. As a consequence, any uncertainty in the intensity measurements results in an error in the velocity estimation. This effect is illustrated in Fig B, where  $dI$  and  $d\lambda$  are the uncertainties in the intensity measurement and the line shift determination, respectively.

There are two major effects influencing the intensity measurement with TESOS: the photon (and detector) noise and the intensity modulation (see A.2).

The peak-to-peak residual intensity modulation amounts to about 1.5% in Fe I spectral line at 557.6 nm and its magnitude is the largest in the continuum and decreases towards the line core. The effect of photon noise is on the other hand larger in the line core than in the continuum: the signal-to-noise ratio in the continuum is about 200 and about twice smaller in the line core. The character of both errors is quite different: while the photon noise can be characterized by a Poisson distribution, the intensity modulation is a systematic error: the modulation is not random,

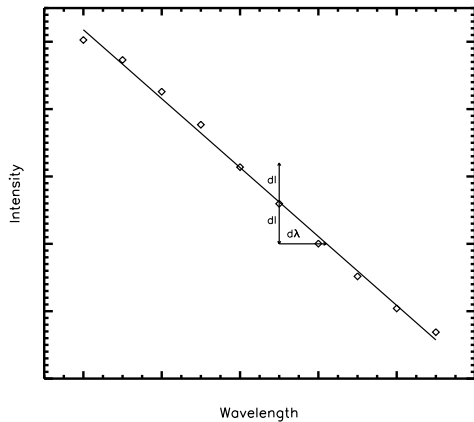


Figure B.1: Illustration of the influence in the intensity measurement error ( $dI$ ) on the precision of the line shift determination ( $d\lambda$ ).

the pattern is constant in time and space.

In order to estimate the precision of the line-of-sight velocity determination, let us consider the line wing at 50% of the line depression, where both effects are not negligible. The velocity uncertainty due to the modulation amounts there to 30 m/s and the error due to noise is about 15 m/s. However, the deconvolution process uses five narrow-band images and the latter is reduced by a square-root of the number of images used. As already mentioned, there are twenty bisectors levels used to calculate line core and line wing velocities, which further reduces the uncertainty to about 3 m/s.

There is still one factor missing in the above analysis: the precision of the line core position determination. Langhans [2003] analyzed the influence of the spectral sampling on the polynomial fit method of the line core determination. If the sampling is critical, the rms error of the line position determination is about 20 m/s.

Taking this into account, the uncertainty of the line wing or line core velocity determination is about 50 m/s.

As already mentioned, the line profiles analyzed here were sampled with the step of 0.84 pm, or, translating a line shift into a velocity, 500 m/s. The actual precision of velocity measurement is thus of an order of magnitude better than the spectral sampling.

## Appendix C

# The optical depth

The optical depth  $\tau$  is a dimensionless quantity measuring the opacity of the medium to radiation passing through it. It depends on the frequency of radiation and it is measured along the optical path  $dl$ . In the astrophysical convention:

$$d\tau_\nu = k_\nu dl$$

and

$$\tau_\nu(l) = \int_0^l k_\nu dl,$$

where  $k_\nu$  is the absorption coefficient and has a dimension of  $\text{m}^{-1}$ ,  $l$  is the geometrical thickness of the layer.

A layer with  $\tau_\nu \gg 1$  is said to be optically thick, while a layer with  $\tau_\nu \ll 1$  is optically thin. A completely transparent medium has an optical depth of zero.

In astrophysics, the surface where  $\tau = 1$  defines the *photosphere* of a star. Photons reaching the photosphere escape more or less freely into space.



# Bibliography

- M. Asplund, H.-G. Ludwig, Å. Nordlund, and R. F. Stein. The effects of numerical resolution on hydrodynamical surface convection simulations and spectral line formation. *A&A*, 359:669–681, July 2000a.
- M. Asplund, Å. Nordlund, R. Trampedach, C. Allende Prieto, and R. F. Stein. Line formation in solar granulation. I. Fe line shapes, shifts and asymmetries. *A&A*, 359:729–742, July 2000b.
- C. Beck, W. Schmidt, L. R. Bellot Rubio, R. Schlichenmaier, and P. Suetterlin. Polarimetric observations of the formation a G-band bright point. In *ASP Conf. Ser.: Proceedings of the 4th Solar Polarization Workshop, Boulder*, page 0, 2006.
- L. R. Bellot Rubio, I. Rodríguez Hidalgo, M. Collados, E. Khomenko, and B. Ruiz Cobo. Observation of Convective Collapse and Upward-moving Shocks in the Quiet Sun. *ApJ*, 560:1010–1019, October 2001.
- C. Bendlin, R. Volkmer, and F. Kneer. A new instrument for high resolution, two-dimensional solar spectroscopy. *A&A*, 257:817–823, April 1992.
- T. Berger. Observation and Analysis of Small-scale Solar Magnetic Structure. *Bulletin of the American Astronomical Society*, 28:869, May 1996.
- T. E. Berger, M. G. Löfdahl, R. S. Shine, and A. M. Title. Measurements of Solar Magnetic Element Motion from High-Resolution Filtergrams. *ApJ*, 495:973, March 1998.
- T. E. Berger, C. J. Schrijver, R. A. Shine, T. D. Tarbell, A. M. Title, and G. Scharmer. New Observations of Subarcsecond Photospheric Bright Points. *ApJ*, 454:531–544, November 1995.
- T. E. Berger and A. M. Title. On the Dynamics of Small-Scale Solar Magnetic Elements. *ApJ*, 463:365, May 1996.
- T. E. Berger and A. M. Title. On the Relation of G-Band Bright Points to the Photospheric Magnetic Field. *ApJ*, 553:449–469, May 2001.

- F. C. Bettonvil, P. Suetterlin, R. H. Hammerschlag, A. P. Jagers, and R. J. Rutten. Multi-wavelength imaging system for the Dutch Open Telescope. In *Innovative Telescopes and Instrumentation for Solar Astrophysics*. Edited by Stephen L. Keil, Sergey V. Avakyan. *Proceedings of the SPIE, Volume 4853*, pages 306–317, February 2003.
- D. Bonaccini, A. Righini, F. Cavallini, and G. Ceppatelli. High resolution solar bidimensional spectroscopy with a universal birefringent filter in tandem with a Fabry-Perot interferometer. *A&A*, 217:368–374, June 1989.
- B. Bovelet and E. Wiehr. A New Algorithm for Pattern Recognition and its Application to Granulation and Limb Faculae. *Solar Phys.*, 201:13–26, October 2001.
- M. P. Cagigal and V. F. Canales. Generalized Fried parameter after adaptive optics partial wave-front compensation. *Optical Society of America Journal A*, 17:903–910, 2000.
- F. Cavallini and et al. IBIS: A Purely Interferometric Instrument for Solar Bidimensional Spectroscopy. In *ESA SP-463: The Solar Cycle and Terrestrial Climate, Solar and Space weather*, page 607, 2000.
- M. Collados, I. Rodriguez Hidalgo, E. Ballesteros, B. Ruiz Cobo, J. Sanchez Almeida, and J. C. del Toro Iniesta. Two-dimensional, high spatial resolution, solar spectroscopy using a Correlation Tracker. II. Maps of spectral quantities. *A&ASS*, 115:367, February 1996.
- C. R. de Boer and F. Kneer. Speckle observations of abnormal solar granulation. *A&A*, 264:L24–L26, 1992.
- D. Dravins. Photospheric spectrum line asymmetries and wavelength shifts. *Annu. Rev. Astron. Astrophys.*, 20:61–89, 1982.
- D. Dravins, L. Lindegren, and A. Nordlund. Solar granulation - Influence of convection on spectral line asymmetries and wavelength shifts. *A&A*, 96:345–364, March 1981.
- R. B. Dunn and J. B. Zirker. The Solar Filigree. *Solar Phys.*, 33:281, 1973.
- Y. Fan. Magnetic Fields in the Solar Convection Zone. *Living Reviews in Solar Physics*, 1:1–62, July 2004.
- A. Ferriz-Mas, M. Schuessler, and V. Anton. Dynamics of magnetic flux concentrations - The second-order thin flux tube approximation. *A&A*, 210:425–432, February 1989.
- J. Fontenla, O. R. White, P. A. Fox, E. H. Avrett, and R. L. Kurucz. Calculation of Solar Irradiances. I. Synthesis of the Solar Spectrum. *ApJ*, 518:480–499, June 1999.
- E. N. Frazier and J. O. Stenflo. Magnetic, velocity and brightness structure of solar faculae. *A&A*, 70:789–799, December 1978.

- D. J. Galloway and N. O. Weiss. Convection and magnetic fields in stars. *ApJ*, 243:945–953, February 1981.
- U. Grossmann-Doerth, M. Schuessler, and O. Steiner. Convective intensification of solar surface magnetic fields: results of numerical experiments. *A&A*, 337:928–939, September 1998.
- E. A. Gurtovenko, V. A. Sheminova, and A. P. Sarychev. What is the difference between 'emission' and 'depression' contribution functions? *Solar Phys.*, 136:239–250, December 1991.
- A. Hanslmeier, W. Mattig, and A. Nesis. High spatial resolution solar photospheric line observations in Ca(+) active regions. *A&A*, 244:521–532, April 1991a.
- A. Hanslmeier, W. Mattig, and A. Nesis. Selected examples of bisector and line parameter variation over a granular-intergranular region. *A&A*, 251:669–674, November 1991b.
- J. W. Hardy, editor. *Adaptive optics for astronomical telescopes*, 1998.
- J. Hirzberger and F. Kneer. 2D-spectroscopy of the Evershed flow in sunspots. *A&A*, 378:1078–1086, November 2001.
- R. Howard and J. O. Stenflo. On the Filamentary Nature of Solar Magnetic Fields. *Solar Phys.*, 22:402, 1972.
- A. Johanneson, T. Bida, B. Lites, and G. B. Scharmer. Very high spatial resolution two-dimensional solar spectroscopy with video CCDs. *A&A*, 258:572–582, May 1992.
- U. G. Jorgensen, M. Larsson, A. Iwamae, and B. Yu. Line intensities for CH and their application to stellar atmospheres. *A&A*, 315:204–211, November 1996.
- C. U. Keller, J. O. Stenflo, S. K. Solanki, T. D. Tarbell, and A. M. Title. Solar magnetic field strength determinations from high spatial resolution filtergrams. *A&A*, 236:250–255, September 1990.
- C. U. Keller and O. von der Lühe. Solar speckle polarimetry. *A&A*, 261:321–328, 1992.
- T. J. Kentischer, W. Schmidt, M. Sigwarth, and M. V. Uexkuell. TESOS, a double Fabry-Perot instrument for solar spectroscopy. *A&A*, 340:569–578, December 1998.
- K. T. Knox and B. J. Thompson. Recovery of images from atmospherically degraded short-exposure photographs. *ApJL*, 193:L45–L48, 1974.
- A. N. Kolmogorov. Die lokale Struktur der Turbulenz in einer inkompressiblen zähen Flüssigkeit bei sehr groen REYNOLDSschen Zahlen. *Dokl. Akad. Nauk. SSSR*, 32:299–303, 1941.
- D. Korff. Analysis of a Method for Obtaining Near Diffraction Limited Information in the Presence of Atmospheric Turbulence. *Optical Society of America Journal*, 63:971–980, 1973.

- J. Krieg, M. Wunnenberg, F. Kneer, M. Koschinsky, and C. Ritter. Height variation of the solar granulation. *A&A*, 343:983–989, 1999.
- A. Labeyrie. Attainment of Diffraction Limited Resolution in Large Telescopes by Fourier Analysing Speckle Patterns in Star Images. *A&A*, 6:85, 1970.
- K. Langhans. *PhD thesis*. 2003.
- K. Langhans, W. Schmidt, and A. Tritschler. 2D-spectroscopic observations of G-band bright structures in the solar photosphere. *A&A*, 394:1069–1076, November 2002.
- W. Livingston and J. Harvey. Observational Evidence for Quantization in Photospheric Magnetic Flux. *Solar Phys.*, 10:294, 1969.
- P. Magain. Contribution functions and the depths of formation of spectral lines. *A&A*, 163:135–139, July 1986.
- J. P. Mehlretter. Observations of photospheric faculae at the center of the solar disk. *Solar Phys.*, 38:43–57, September 1974.
- K. Mikurda, O. von der Lühe, and F. Wöger. Solar Imaging with an Extended Knox-Thompson Technique. *Astronomische Nachrichten Supplement*, 324:112, 2003.
- K. Mikurda and O. von der Lühe. *Solar Physics*, accepted, 2006.
- R. Muller. Morphological and Dynamic Properties of Magnetic Bright Points in the Quiet Photosphere. In *Japan-France Seminar on Solar Physics*, page 142, 1980.
- R. Muller. The dynamical behavior of facular points in the quiet photosphere. *Solar Phys.*, 85:113–121, May 1983.
- R. Muller, A. Dollfus, M. Montagne, J. Moity, and J. Vigneau. Spatial and temporal relations between magnetic elements and bright points in the photospheric network. *A&A*, 359:373–380, July 2000.
- R. Muller, J. C. Hulot, and T. Roudier. Perturbation of the granular pattern by the presence of magnetic flux tubes. *Solar Phys.*, 119:229–243, 1989.
- R. Muller and S. L. Keil. The characteristic size and brightness of facular points in the quiet photosphere. *Solar Phys.*, 87:243–250, September 1983.
- R. Muller and B. Mena. Motions around a decaying sunspot. *Solar Phys.*, 112:295–303, 1987.
- R. Muller and T. Roudier. Variability of the quiet photospheric network. *Solar Phys.*, 94:33–47, August 1984.

- R. Muller, T. Roudier, J. Vigneau, and H. Auffret. The proper motion of network bright points and the heating of the solar corona. *A&A*, 283:232–240, March 1994.
- P. Nisenson, A. A. van Ballegooijen, A. G. de Wijn, and P. Sütterlin. Motions of Isolated G-Band Bright Points in the Solar Photosphere. *ApJ*, 587:458–463, April 2003.
- E. N. Parker. A Kinematical Theory of Turbulent Hydromagnetic Fields. *ApJ*, 138:226–238, July 1963.
- E. N. Parker. Hydraulic concentration of magnetic fields in the solar photosphere. VI - Adiabatic cooling and concentration in downdrafts. *ApJ*, 221:368–377, April 1978.
- E. Pehlemann and O. von der Lühe. Technical aspects of the speckle masking phase reconstruction algorithm. *A&A*, 216:337–346, 1989.
- T. R. Rimmele. Recent advances in solar adaptive optics. In *Advancements in Adaptive Optics. Edited by Domenico B. Calia, Brent L. Ellerbroek, and Roberto Ragazzoni. Proceedings of the SPIE, Volume 5490, pp. 34-46 (2004).*, pages 34–46, October 2004.
- B. Roberts and A. R. Webb. Vertical motions in an intense magnetic flux tube. *Solar Phys.*, 56: 5–35, January 1978.
- M. C. Roggemann and B. Welsh. *Imaging through turbulence*. Imaging through turbulence, Publisher: Boca Raton, FL: CRC Press, 1996. Series: Laser and optical science and technology. ISBN: 0849337879, 1995.
- P. Sütterlin, R. J. Rutten, and V. I. Skomorovsky. Ba II 4554 Å speckle imaging as solar Doppler diagnostic. *A&A*, 378:251–256, October 2001a.
- P. Sütterlin, R. J. Rutten, and V. I. Skomorovsky. Ba II 4554 Å speckle imaging as solar Doppler diagnostic. *A&A*, 378:251–256, October 2001b.
- M. Schüssler. Small-Scale Photospheric Magnetic Fields. In *NATO ASIC Proc. 373: The Sun: A Laboratory for Astrophysics*, page 191, 1992.
- M. Schüssler. Numerical Simulation of Solar Magneto-Convection. In *ASP Conf. Ser. 236: Advanced Solar Polarimetry – Theory, Observation, and Instrumentation*, pages 343–354, January 2001.
- G. B. Scharmer. High Resolution Granulation Observations from La Palma: Techniques and First Results. In *NATO ASIC Proc. 263: Solar and Stellar Granulation*, page 161, 1989.
- P. H. Scherrer, R. S. Bogart, R. I. Bush, J. T. Hoeksema, A. G. Kosovichev, J. Schou, W. Rosenberg, L. Springer, T. D. Tarbell, A. Title, C. J. Wolfson, I. Zayer, and MDI Engineering Team. The Solar Oscillations Investigation - Michelson Doppler Imager. *Solar Phys.*, 162:129–188, 1995.

- R. Schlichenmaier and W. Schmidt. Flow geometry in a sunspot penumbra. *A&A*, 358:1122–1132, June 2000.
- S. Shelyag, M. Schüssler, S. K. Solanki, S. V. Berdyugina, and A. Vögler. G-band spectral synthesis and diagnostics of simulated solar magneto-convection. *A&A*, 427:335–343, November 2004.
- S. K. Solanki. Smallscale Solar Magnetic Fields - an Overview. *Space Science Reviews*, 63:86–97, 1993.
- S. K. Solanki and V. Brigljevic. Continuum brightness of solar magnetic elements. *A&A*, 262:L29–L32, September 1992.
- D. Soltau, T. Berkefeld, O. von der Lühe, F. Wöger, and T. Schelenz. Adaptive optics and multi-conjugate adaptive optics with the vtt. *AN*, 323:236–240, 2002.
- H. C. Spruit. Pressure equilibrium and energy balance of small photospheric fluxtubes. *Solar Phys.*, 50:269–295, December 1976.
- H. C. Spruit and C. Zwaan. The size dependence of contrasts and numbers of small magnetic flux tubes in an active region. *Solar Phys.*, 70:207–228, April 1981.
- H. C. Spruit and E. G. Zweibel. Convective instability of thin flux tubes. *Solar Phys.*, 62:15–22, May 1979.
- R. F. Stein and A. Nordlund. Simulations of Solar Granulation. I. General Properties. *ApJ*, 499:914, May 1998.
- R. F. Stein and Å. Nordlund. Radiative Transfer in 3D Numerical Simulations. In *ASP Conf. Ser. 288: Stellar Atmosphere Modeling*, page 519, January 2003.
- O. Steiner. Flux Tube Dynamics. In *Astronomical Society of the Pacific Conference Series*, pages 38–54, September 1999.
- O. Steiner, U. Grossmann-Doerth, M. Knoelker, and M. Schuessler. Dynamical Interaction of Solar Magnetic Elements and Granular Convection: Results of a Numerical Simulation. *ApJ*, 495:468, March 1998.
- O. Steiner, P. H. Hauschildt, and J. Bruls. Radiative properties of magnetic elements. I. Why are vec G-band bright points bright? *A&A*, 372:L13–L16, June 2001.
- J. O. Stenflo. On the influence of the slit size on measurements with a solar magnetograph. *Arkiv for Astronomi*, 4:173–198, 1968.
- J. O. Stenflo. Magnetic-Field Structure of the Photospheric Network. *Solar Phys.*, 32:41, 1973.

- J. O. Stenflo and J. W. Harvey. Dependence of the properties of magnetic fluxtubes on area factor or amount of flux. *Solar Phys.*, 95:99–118, January 1985.
- G. I. Taylor. The spectrum of turbulence. *Royal Society of London Proceedings Series A*, 164: 476–490, 1938.
- A. Title and W. Rosenberg. Variations of Birefringent Filters for Solar and Stellar Applications. In *Solar instrumentation: What's next?*, page 326, March 1981.
- A. M. Title, T. D. Tarbell, K. P. Topka, S. H. Ferguson, R. A. Shine, and SOUP Team. Statistical properties of solar granulation derived from the SOUP instrument on Spacelab 2. *ApJ*, 336: 475–494, January 1989.
- F. Tomita. *Computer Analysis of Visual Textures*. Kluwer, 1990.
- K. P. Topka, T. D. Tarbell, and A. M. Title. Properties of the Smallest Solar Magnetic Elements. II. Observations versus Hot Wall Models of Faculae. *ApJ*, 484:479, July 1997.
- A. Tritschler, W. Schmidt, K. Langhans, and T.J. Kentischer. High-resolution solar spectroscopy with TESOS - Upgrade from a double to a triple system. *Solar Phys.*, 211:17–29, 2002.
- M. van Noort, L. van der Rouppe, and Löfdahl. *Solar Physics*, in press, 2005.
- O. von der Lühe. Estimating Fried's parameter from a time series of an arbitrary resolved object imaged through atmospheric turbulence. *Optical Society of America Journal A*, 1:510–519, May 1984.
- O. von der Lühe. Signal Transfer Function of the Knox-Thompson Speckle Imaging Technique. *Optical Society of America Journal A*, 5:721–729, 1988.
- O. von der Lühe. *PhD Thesis*. 1985.
- O. von der Lühe. Speckle imaging of solar small scale structure. I - Methods. *A&A*, 268:374–390, 1993.
- O. von der Lühe. Speckle imaging of solar small scale structure. 2: Study of small scale structure in active regions. *A&A*, 281:889–910, January 1994.
- O. von der Lühe, T. Berkefeld, and D. Soltau. Multi-Conjugate Solar Adaptive Optics at the Vacuum Tower Telescope on Tenerife. *C. R. Physique*, 6:351–360, in press.
- O. von der Lühe, D. Soltau, T. Berkefeld, and T. Schelenz. KAOS: Adaptive optics system for the Vacuum Tower Telescope at Teide Observatory. In S. L. Keil and S. V. Avakyan, editors, *Innovative Telescopes and Instrumentation for Solar Astrophysics. Proceedings of the SPIE*, volume 4853, pages 187–193, 2003.

- G. P. Weigelt. Modified astronomical speckle interferometry 'speckle masking'. *Optics Communications*, 21:55–59, 1977.
- N. O. Weiss. The Expulsion of Magnetic Flux by Eddies. *Royal Society of London Proceedings Series A*, 293:310–328, 1966.
- E. Wiehr, B. Bovelet, and J. Hirzberger. Brightness and size of small-scale solar magnetic flux concentrations. *A&A*, 422:L63–L66, July 2004.
- Z. Yi and O. Engvold. Filigree, magnetic fields, and flows in the photosphere. *Solar Phys.*, 144: 1–14, March 1993.

### Abbreviations used in the text

AO	Adaptive Optics
CCD	Charged Coupled Device
DOT	Dutch Open Telescope
FOV	Field of View
FWHM	Full Width at Half Maximum
FPI	Fabry-Perot Interferometer
KIS	Kiepenheuer-Institut Für Sonnenphysik
KISIP	Kiepenheuer-Institut Speckle Imaging Package
LOS	Line-of-Sight
LTE	Local Thermodynamic Equilibrium
MFI	Michelson Interferometer
MHD	Magnetohydrodynamics
MLSO	Mauna Loa Solar Observatory.
NSO	National Solar Observatory
OTF	Optical Transfer Function
PBP	Photospheric Bright Point
PSF	Point Spread Function
SNR	Signal-to-Noise Ratio
STF	Speckle Transfer Function
TIP	Tenerife Infrared Polarimeter
SVST	Swedish Vacuum Solar Telescope
TESOS	TElecentric SOLar Spectrometer
VTT	Vacuum Tower Telescope



## Acknowledgments

During the years I spent at the Kiepenheuer-Institut my advisors were Prof. Dr. Oskar von der Lüche and Dr. Wolfgang Schmidt. Oskar von der Lüche taught me everything I know about the image reconstruction techniques and Wolfgang Schmidt was an excellent tutor as far as two-dimensional solar spectroscopy was concerned.

My colleagues: Kai Langhans, Alexandra Tritschler and Christian Beck were my companions during the observational campaigns at the VTT. I am grateful to them for all their enlightening comments which made me get the best out of my work.

Oskar Steiner helped me to understand the flux tube models and the simulations of solar magnetoconvection. He and Kai Langhans provided me also with their figures to use in this thesis.

I am very grateful to Thomas Berkefeld, Dirk Soltau and the KAOS Team for all their efforts to make the adaptive optics system running at the VTT.

Thomas Kentischer was not annoyed with my emergency phone calls from Tenerife, even if I called on Sunday morning. He taught me a lot about TESOS.

I express my thanks to all assistants who accompanied me during my observational campaigns. Your help really meant much to me.

Christoph Keller was my host during my stay at the National Solar Observatory in Tucson, AZ, in summer 2002. Our discussions have always motivated me to ask new questions.

Special thanks for Peter Caligari and Reiner Hammer for an efficient management of the computer system at the KIS and the VTT. You really saved my life several times !

I am very grateful to organizations who supported my work financially, especially to the Deutsche Forschungs Gemeinschaft (DFG), which approved and supported our project (grant no. SCHM 1168/3), but also to the European Commission which sponsored my participation in the XV Canary Islands Winter School of Astrophysics on Tenerife, in November 2003.

I thank Gerd for believing in me.